The Hashemite Kingdom of Jordan

Yarmouk University

Jordan Journal of
PHYSICS
An International Peer-Reviewed Research Journal

Instructions to Authors

Instructions to authors concerning manuscript organization and format apply to hardcopy submission by mail, and also to electronic online submission via the Journal homepage website (http://jjp.yu.edu.jo).

Manuscript Submission

1- **Hardcopy**: The original and three copies of the manuscript, together with a covering letter from the corresponding author, should be submitted to the Editor-in-Chief:

Professor Ibrahim O. Abu Al-Jarayesh
Editor-in-Chief, Jordan Journal of Physics
Deanship of Scientific Research and Graduate Studies
Yarmouk University, Irbid, Jordan.
Tel: 00962-2-7211111, Ext. 3735
Fax: 00962-2-7211121
E-mail: jjp@yu.edu.jo

2- **Online**: Follow the instructions at the journal homepage website.

Original *Research Articles*, *Communications* and *Technical Notes* are subject to critical review by minimum of two competent referees. Authors are encouraged to suggest names of competent reviewers. *Feature Articles* in active Physics research fields, in which the author's own contribution and its relationship to other work in the field constitute the main body of the article, appear as a result of an invitation from the Editorial Board, and will be so designated. The author of a *Feature Article* will be asked to provide a clear, concise and critical status report of the field as an introduction to the article. *Review Articles* on active and rapidly changing Physics research fields will also be published. Authors of *Review Articles* are encouraged to submit two-page proposals to the Editor-in-Chief for approval. Manuscripts submitted in *Arabic* should be accompanied by an Abstract and Keywords in English.

Organization of the Manuscript

Manuscripts should be typed double spaced on one side of A4 sheets (21.6 x 27.9 cm) with 3.71 cm margins, using Microsoft Word 2000 or a later version thereof. The author should adhere to the following order of presentation: Article Title, Author(s), Full Address and E-mail, Abstract, PACS and Keywords, Main Text, Acknowledgment. Only the first letters of words in the Title, Headings and Subheadings are capitalized. Headings should be in **bold** while subheadings in *italic* fonts.

Title Page: Includes the title of the article, authors' first names, middle initials and surnames and affiliations. The affiliation should comprise the department, institution (university or company), city, zip code and state and should be typed as a footnote to the author's name. The name and complete mailing address, telephone and fax numbers, and e-mail address of the author responsible for correspondence (designated with an asterisk) should also be included for official use. The title should be carefully, concisely and clearly constructed to highlight the emphasis and content of the manuscript, which is very important for information retrieval.

Abstract: A one paragraph abstract not exceeding 200 words is required, which should be arranged to highlight the purpose, methods used, results and major findings**.**

Keywords: A list of 4-6 keywords, which expresses the precise content of the manuscript for indexing purposes, should follow the abstract.

PACS: Authors should supply one or more relevant PACS-2006 classification codes, (available at http://www.aip.org/pacs/pacs06/pacs06-toc.html)

Introduction: Should present the purpose of the submitted work and its relationship to earlier work in the field, but it should not be an extensive review of the literature (e.g., should not exceed 1 ½ typed pages).

Experimental Methods: Should be sufficiently informative to allow competent reproduction of the experimental procedures presented; yet concise enough not to be repetitive of earlier published procedures.

Results: should present the results clearly and concisely.

Discussion: Should be concise and focus on the interpretation of the results.

Conclusion: Should be a brief account of the major findings of the study not exceeding one typed page.

Acknowledgments: Including those for grant and financial support if any, should be typed in one paragraph directly preceding the References.

References: References should be typed double spaced and numbered sequentially in the order in which they are cited in the text. References should be cited in the text by the appropriate Arabic numerals, enclosed in square brackets. Titles of journals are abbreviated according to list of scientific periodicals. The style and punctuation should conform to the following examples:

1. Journal Article:
   a) Heisenberg, W., Z. Phys. 49 (1928) 619.
   b) Bednorz, J. G. and Müller, K. A., Z. Phys. B64 (1986) 189
   c) Bardeen, J., Cooper, L.N. and Schrieffer, J. R., Phys. Rev. 106 (1957) 162.
   d) Asad, J. H., Hijjawi, R. S., Sakaji, A. and Khalifeh, J. M., Int. J. Theor. Phys. 44(4) (2005), 3977.

2. Books with Authors, but no Editors:
   a) Kittel, C., "Introduction to Solid State Physics", 8th Ed. (John Wiley and Sons, New York, 2005), chapter 16.
   b) Chikazumi, S., C. D. Graham, JR, "Physics of Ferromagnetism", 2nd Ed. (Oxford University Press, Oxford, 1997).

3. Books with Authors and Editors:
   a) Allen, P. B. "Dynamical Properties of Solids", Ed. (1), G. K. Horton and A. A. Maradudin (North-Holland, Amsterdam, 1980), p137.
   b) Chantrell, R. W. and O'Grady, K., "Magnetic Properities of Fine Particles" Eds. J. L. Dormann and D. Fiorani (North-Holland, Amsterdam, 1992), p103.

4. Technical Report:
Purcell, J. "The Superconducting Magnet System for the 12-Foot Bubble Chamber", report ANL/HEP6813, Argonne Natt. Lab., Argonne, III, (1968).

5. Patent:
Bigham, C. B., Schneider, H. R., US patent 3 925 676 (1975).

6. Thesis:
Mahmood, S. H., Ph.D. Thesis, Michigan State University, (1986), USA (Unpublished).

7. Conference or Symposium Proceedings:
Blandin, A. and Lederer, P. Proc. Intern. Conf. on Magnetism, Nottingham (1964), P.71.

8. Internet Source:
Should include authors' names (if any), title, internet website, URL, and date of access.

9. Prepublication online articles (already accepted for publication):
Should include authors' names (if any), title of digital database, database website, URL, and date of access.

For other types of referenced works, provide sufficient information to enable readers to access them.

Tables: Tables should be numbered with Arabic numerals and referred to by number in the Text (e.g., Table 1). Each table should be typed on a separate page with the legend above the table, while explanatory footnotes, which are indicated by superscript lowercase letters, should be typed below the table.

Illustrations: Figures, drawings, diagrams, charts and photographs are to be numbered in a consecutive series of Arabic numerals in the order in which they are cited in the text. Computer-generated illustrations and good-quality digital photographic prints are accepted. They should be black and white originals (not photocopies) provided on separate pages and identified with their corresponding numbers. Actual size graphics should be provided, which need no further manipulation, with lettering (Arial or Helvetica) not smaller than 8 points, lines no thinner than 0.5 point, and each of uniform density. All colors should be removed from graphics except for those graphics to be considered for publication in color. If graphics are to be submitted digitally, they should conform to the following minimum resolution requirements: 1200 dpi for black and white line art, 600 dpi for grayscale art, and 300 dpi for color art. All graphic files must be saved as TIFF images, and all illustrations must be submitted in the actual size at which they should appear in the journal. Note that good quality hardcopy original illustrations are required for both online and mail submissions of manuscripts.

Text Footnotes: The use of text footnotes is to be avoided. When their use is absolutely necessary, they should be typed at the bottom of the page to which they refer, and should be cited in the text by a superscript asterisk or multiples thereof. Place a line above the footnote, so that it is set off from the text.

Supplementary Material: Authors are encouraged to provide all supplementary materials that may facilitate the review process, including any detailed mathematical derivations that may not appear in whole in the manuscript.

Revised Manuscript and Computer Disks

Following the acceptance of a manuscript for publication and the incorporation of all required revisions, authors should submit an original and one more copy of the final disk containing the complete manuscript typed double spaced in Microsoft Word for Windows 2000 or a later version thereof. All graphic files must be saved as PDF, JPG, or TIFF images.

Allen, P.B., "……………", in: Horton, G.K., and Muradudin, A. A., (eds.), "Dynamical…….", (North……..), pp….

Reprints

Twenty (20) reprints free of charge are provided to the corresponding author. For orders of more reprints, a reprint order form and prices will be sent with the article proofs, which should be returned directly to the Editor for processing.

Copyright

Submission is an admission by the authors that the manuscript has neither been previously published nor is being considered for publication elsewhere. A statement transferring copyright from the authors to Yarmouk University is required before the manuscript can be accepted for publication. The necessary form for such transfer is supplied by the Editor-in-Chief. Reproduction of any part of the contents of a published work is forbidden without a written permission by the Editor-in-Chief.

Disclaimer

Opinions expressed in this Journal are those of the authors and neither necessarily reflects the opinions of the Editorial Board or the University, nor the policy of the Higher Scientific Research Committee or the Ministry of Higher Education and Scientific Research. The publisher shoulders no responsibility or liability whatsoever for the use or misuse of the information published by JJP.

Indexing

JJP is currently applying for indexing and abstracting to all related International Services.

Table of Contents:

Jordan Journal of Physics

REVIEW ARTICLE

Computational Condensed Matter Physics: Progress and Prospects

Abdallah Qteish

Department of Physics, Yarmouk University, 21163 Irbid, Jordan.

Abstract: Computational condensed matter physics is nowadays a highly developed field of research, in terms of basic theory, algorithms and applications. Providing a comprehensive account of this subject is hence far beyond the scope of any review article. Therefore, I will introduce this subject through a set of examples taken from my recent research work, which touch upon some important developments in this field. These developments are the exact exchange formalism within Kohn-Sham density functional theory, combined exact exchange and many-body quasiparticle approach (for highly accurate band structure calculations), and maximally localized Wannier functions. The theoretical background of the above approaches in addition to the density functional perturbation theory (used to calculate the phonon spectra and other related physical properties of solids) will be briefly described, and representative results are shown to demonstrate the accuracy and predictive power of these theoretical approaches.

Keywords: Density functional theory; Density functional perturbation theory; Quasiparticle GW calculations; Exact-exchange; Electronic structure; Phonon spectra; Thermal properties; Wannier functions; Bond ionicity.
PACS: 71.15.Mb, 71.10.-w, 63.20.kd, 65.40.-b

I. Introduction

Direct application of standard quantum mechanics to condensed matter systems is a highly complicated many-body problem, which is simply impossible to solve both analytically or numerically. Thus, it is not surprising that in almost all practical quantum mechanical approaches the many-body problem is transformed to a single-body one. The magic of the Kohn-Sham (KS) formalism [1] of density functional theory (DFT) [2] arises from its proof that this transformation can be *exactly* performed. Thus, the problem of finding the system total energy, charge density and other ground state physical properties can be obtained by solving self-consistently a set of single-particle Schrödinger like equations (known as KS equations). The corresponding effective potential which is *functional* of the charge density, ρ, is called KS potential. In this formalism, all the quantum short-ranged effects are rolled up in the exchange-correlation (XC) energy term, $E_{XC}[\rho]$, which is the only part of the total energy that needs to be approximated. Moreover, the theory itself suggests some practical and well understood approximations for $E_{XC}[\rho]$. The most widely used are the local density approximation (LDA) and generalized gradient approximation (GGA). These approximations are found to give very good results for various properties of a wide range of materials, and this approach is currently being used to tackle fundamental problems in physics, chemistry, geophysics, material science and biology. See Ref. 3 for an excellent review of the basic theory and applications of this theoretical approach. A brief description of the KS-DFT formalism and E_{XC} is given in Sec. II.

Corresponding Author: Abdallah Qteish. **Email**: aqteish@yu.edu.jo

In spite of their enormous successes, the KS-DFT calculations have also several limitations. Here, we focus on two major sources of errors in the KS-DFT calculations based on LDA or GGA: (i) the presence of spurious self-interaction (SI) arising form the use of approximate exchange energy functionals [4], and (ii) the absence of a derivative discontinuity in the exchange-correlation potential with respect to changes in the particle number in both LDA and GGA functionals [5], which has a profound effect on the calculated band gaps of semiconductors and insulators. See Ref. [6] for a recent review of these limitations and their consequences, especially for transition metal and rare earth compounds. When applied to calculate the electronic structure of solids, two main problems are observed: (1) The band gap of semiconductors and insulators are highly underestimated (known as band gap problem), which is due to the above two deficiencies, and (2) the binding energies of the highly localized states are significantly lower than the corresponding experiment values, which is usually attributed to the spurious SI [7,8].

A recent important development is the exact exchange formalism within KS-DFT approach [9-11]. This is a major step forward, since the exchange energy is explicitly calculated, removing thus the spurious SI and leaving only the correlation energy to be approximated. It should be noted that the resulting *local* exact exchange potential is orbital dependent, which makes its computation very expensive in terms of both memory and CPU time, compared to LDA calculations. It has been recognized that this exact exchange potential is equivalent [12] to the optimized effective potential (OEP, Refs. 13 and 14): the best local potential that approximates the *non-local* Hartree-Fock potential, which has long been used in atomic and molecular calculations. Thus, this approach when used together with LDA correlation, hereafter denoted as OEPx(cLDA), is found to yield significant opening of the band gap of a wide range of semiconductors and insulators, leading to improved effective masses and optical properties [11]. However, the OEPx(cLDA) method does not completely solve the band gap problem, and we have shown [15] that

the removal of the SI, in this approach, does not improve the KS-DFT description of the binding energies of the highly localized states, contrary to the above common belief. The LDA, GGA and OEPx exchange-correlation functionals will be introduced in Sec. III.

For accurate band structure calculations, one thus needs to go beyond the KS-DFT formalism. The most widely used approach is the quasiparticle energy calculations [16,17] in Hedin's GW approximation [18] for the many-body self-energy operator. The application of the GW approximation to calculate the electronic structure of solids is pioneered by Hybertsen and Louie [19] and Godby, Schlüter and Sham [20]. The formal relationship between the quasiparticle energies and the experimental valence and conduction band energies, obtained respectively using photoemission spectroscopy and inverse photoemission spectroscopy, is clearly described in Ref. [17]. Originally, the Green's function G_0 and the screened potential W_0 required in the GW approximation (henceforth denoted G_0W_0) are calculated from a set of LDA single particle-energies and wave functions (LDA-G_0W_0). The LDA-G_0W_0 approach is found to accurately predict band gaps of *sp*-bonded semiconductors (with a typical error bar of 0.1 eV). However, complications arise when the LDA-G_0W_0 approach is used to calculate the electronic structure of semiconductors with negative LDA band gaps [21, 22] or when occupied shallow semicore *d* bands are treated as valence in the pseudopotential GW framework [23-25].

The above complications in the LDA-G_0W_0 calculations can be removed [17] by calculating G_0 and W_0 from OEPx(cLDA) single particle data [OEPx(cLDA)-G_0W_0]. This is another important development because of two reasons: (i) The quasiparticle corrections to the KS-DFT eigenvalues are commonly calculated by using first order perturbation theory. The opening of the band gaps within the OEPx(cLDA) makes these corrections smaller than those of LDA-G_0W_0, leading to a better validity and accuracy of these GW calculations. (ii) The OEPx(cLDA) method gives a much better description of the core states than LDA. This is especially important for the states whose wavefunctions

overlap strongly with those of the considered valence states, which allows the treatment of these highly localized states as part of the frozen core, contrary to the pseudopotential LDA-G_0W_0 approach [23-25]. Moreover, this also makes the generated OEPx(cLDA) pseudopotentials superior to those of LDA. We have found that the OEPx(cLDA)-G_0W_0 approach reproduces very well the band gaps of a wide range of semiconductors, including group-III nitrides [15,17,26-28], II-V compounds [17,29] and transition metal nitrides [30,31]. The OEPx(cLDA)-G_0W_0 approach will be introduced in Sec. IV.

Many physical properties of solids are directly related to successive derivatives of the system total energy with respect to external perturbations. These properties can be most efficiently calculated using density functional perturbation theory (DFPT); an interesting merging of perturbation theory and DFT [32-36]. This approach is based on a variational principle that provides accurate expressions for the energy derivatives and gives even access to non-linear responses. The perturbations considered in this review are the atomic displacements [35], homogeneous electric field [35] and homogeneous strain [37, 38]. Appropriate combinations of these perturbations give access to physical properties of primary interest: the dynamical matrices, elastic constants, Born effective charge and dielectric permittivity tensors. We have recently used this approach to investigate the elastic, dielectric, phonon spectra and thermal properties of some semiconductors [39-41]. The thermal properties of solids are usually studied by employing the quasiharmonic approximation [42,43]. However, very recently, the anharmonic effects have received renewed interest [44,45]. The calculations of these properties using DFPT will be described in Sec. V.

It is worth noting that the *ab inito* calculations of the phonon spectra have been started by Kunc and Martin [46], see also Ref. [47], using the so-called frozen-phonon approach. In this approach, the atoms are displaced according to a certain lattice vibrational mode, and the resulting lower symmetry structure is treated as a new crystal structure. Then, the phonon frequency of this mode is deduced from the difference in the total energy of the two structures (distorted and undistorted). A second technique is the interplanar force constant method [48]. In this approach, the force constants between the plans of atom normal to a high symmetry direction are determined by using the supercell method. A long enough unit cell is constructed along the considered high symmetry direction. The interplanar force constants are then extracted from the Hellmann-Feynman forces exerting on the atoms as a result of an appropriate displacement of central atom in an otherwise ground state structure (zero forces). This approach can be used to calculate the phonon modes along the high symmetry directions, and it is very useful in investigating the phonon dispersion relations of superlattices and heterostructures [49-51]. A third direct approach is the interatomic force constants (IFCs) method [52]. Here, the IFCs are calculated from the Hellmann-Feynman forces resulting from appropriate atomic displacements in a big enough supercell. This approach allows for the calculations of the phonon frequencies at a general k-point in the first Brillouin zone which, in turn, can be used to investigate the thermal properties of solids. On the other hand, the phonon frequencies and the free energy (including anharmonic effects) can be obtained using *ab initio* molecular dynamics, see for example Ref. [45]. However, the main disadvantage of the IFCs and molecular dynamic calculations lies in the relatively small size of the supercell considered. In the DFPT approach, on the other hand, the calculations are performed using the primitive unit cell.

Finally, the electronic states in a periodic potential can be described by either the widely used extended Bloch orbitals or in terms of localized Wannier functions (WFs). The non-uniqueness property of the WFs has dramatically limited their applications. An important recent development is the elegant method of Marzari and Vanderbilt [53] to construct unique maximally localized WFs (MLWFs). Hence, the WF representation has recently received considerable interest. In addition to their relevance in several areas of physics, WFs have found new interesting applications due to their connections with the Berry-phase theory of bulk polarization [54-56] and their potential use as basis in modern

electronic structure calculations to dramatically increase their efficiency [57,58]. We mention here the very recent highly efficient implementation of the GW calculations [58], in terms of MLWFs, which extends their applications to large systems (unit cells with hundreds of atoms). Other applications of the MLWFs include electrical and thermal transport [59,60], strongly correlated systems [61-63], photonic lattices [64], van der Waals interaction [65] and tight-binding calculations [66]. We have introduced [67] a novel first-principle bond ionicity scale based on the centers of the MLWFs. Concepts such as valency, electronegativity and bond ionicity are still very useful in understanding the differences in the properties of different systems and in seeking trends of these properties. Both the MLWFs and the new ionicity scale will be briefly described in Sec. VI.

II. The Kohn-Sham Formalism of Density Functional Theory and Exchange- Correlation Energy

Most of the modern electronic structure calculations are based on density functional theory (DFT), introduced by Hohenberg and Kohn [2]. The DFT states that the electronic charge density, ρ, is a basic quantity as the many-body wavefunctions. This is achieved by proving two theorems: (i) There is a one-to-one correspondence between ρ and the external potential, V_{ext}, up to an additive constant. The V_{ext} determines, in turn, the many-body wavefunctions from which all the physical properties of any electronic system can be extracted. Hence, the physical properties of any electronic system can be expressed as functionals of ρ. Of particular importance is the total energy, $E_{tot}[\rho]$. (ii) A variational principle: the ground state total energy is the global minimum of $E_{tot}[\rho]$, and the ρ that minimizes this functional is the ground state ρ. The main difficulty here is that an explicit expression for $E_{tot}[\rho]$ is unknown.

In a subsequent seminal paper, Kohn and Sham (KS) [1] have introduced the following highly intelligent separation of $E_{tot}[\rho]$:

$$E_{tot}[\rho] = T_o + E_{ext} + E_H + E_{XC}, \qquad (1)$$

where T_o is the kinetic energy of the system of *non*-interacting electrons; E_{ext} is the interaction energy between the electrons and the external potential; E_H is the classical electron – electron (e-e) interaction energy given as

$$E_H = \frac{1}{2} \iint \frac{p(r)p(r')}{|r-r'|} dr\, dr', \qquad (2)$$

and E_{XC} is the sum of the exchange (E_X) and correlation (E_C) energies. It is worth noting that the first three terms can be exactly calculated, leaving only the unknown or difficult to calculate term (E_{XC}) to be approximated. Moreover, the use of T_o instead of kinetic energy of the system of interacting electrons, T, allows for an *exact* transformation from the many-body to single-body problems [1]. Thus, the ground state E_{tot} and ρ can be determined by solving self-consistently a set of single particle Schrödinger like equations (note that atomic units are used)

$$\left[-\frac{\nabla^2}{2} + V_{ext}(r) + V_H(r) + V_{XC}(r) \right] \phi_i(r)$$
$$= \varepsilon_i \phi_i(r). \qquad (3)$$

Here, V_{ext}, V_H and V_{XC} are, respectively, the external potential, Hartree and XC potentials defined as

$$V_J(r) = \frac{\delta E_J}{\delta \rho(r)} \qquad (4)$$

[with J stands for *ext*, H or *XC*].

The electron charge density distribution, ρ, is defined in terms of single-particle orbitals, ϕ_i, as

$$\rho(r) = \sum_i f_i |\phi_i(r)|^2, \qquad (5)$$

where f_i denotes the occupation number of the ith state. Eqs. (1) to (5) have to be solved self-consistently after an approximation for $E_{XC}[\rho]$ is adopted. Several practical methods are currently in use for such a purpose [3]. In our calculations, we employ a norm-conserving pseudopotential plane-wave method [68].

The $E_{XC}[\rho]$ part of the e-e interaction energy deserves a brief description. Let us connect first with the single-particle approach introduced by Hartree in 1930, in which V_{XC}

and E_{XC} are completely neglected from the above equations, and the many-body wavefunction of an N particle system is given as

$$\Psi(\boldsymbol{r}_1, \boldsymbol{r}_2, \boldsymbol{r}_3, ..., \boldsymbol{r}_N) = \psi_1(\boldsymbol{r}_1, \sigma_1)\psi_2(\boldsymbol{r}_2, \sigma_2)...\psi_N(\boldsymbol{r}_N, \sigma_N). \qquad (6)$$

Here, ψ_i is the product of the single particle spatial wavefunctions $\{\phi_i(\boldsymbol{r})\}$ and spin wavefunctions $\{\alpha_i(\sigma)\}$. This form of Ψ does not satisfy Pauli's exclusion principle, which requires anti-symmetric wavefunction. In the Hartree-Fock (HF) [69] approach, this principle is satisfied by writing Ψ as a Slater determinant

$$\Psi = \frac{1}{(N!)^{1/2}}$$

$$\times \begin{vmatrix} \psi_1(\boldsymbol{r}_1, \sigma_1) & \psi_1(\boldsymbol{r}_2, \sigma_2) & \psi_1(\boldsymbol{r}_3, \sigma_3) & \cdots \\ \psi_2(\boldsymbol{r}_1, (\sigma_1) & \psi_2(\boldsymbol{r}_2, \sigma_2) & \psi_2(\boldsymbol{r}_3, \sigma_3) & \cdots \\ \cdot & \cdot & \cdot & \cdots \\ \cdot & \cdot & \cdot & \cdots \end{vmatrix}.$$

$$(7)$$

This choice for Ψ leads to an additional orbital dependent exchange energy term

$$E_X = -\frac{1}{2}\sum_{i,j,\sigma}\int d\boldsymbol{r}\, d\boldsymbol{r}'\left(\phi_i^{\sigma *}(\boldsymbol{r})\phi_j^{\sigma *}(\boldsymbol{r}') \right.$$

$$\left. \times \frac{1}{|\boldsymbol{r}-\boldsymbol{r}'|}\phi_j^{\sigma}(\boldsymbol{r})\phi_i^{\sigma}(\boldsymbol{r}')\right). \qquad (8)$$

The corresponding exchange potential is non-local and orbital dependent, and the differential-integral equations to solve in the HF approach take the form

$$\int d^3\boldsymbol{x}'\left(-\frac{1}{2}\nabla^2\delta(\boldsymbol{x}-\boldsymbol{x}') + V_{ext}(\boldsymbol{x})\delta(\boldsymbol{x}-\boldsymbol{x}')\right.$$

$$\left. + V_H(\boldsymbol{x})\delta(\boldsymbol{x}-\boldsymbol{x}') + V_X^{HF}(\boldsymbol{x},\boldsymbol{x}')\right)\phi_i(\boldsymbol{x}')$$

$$= \sum_{i\neq j}\varepsilon_{ij}\phi_j(\boldsymbol{x}),$$

$$(9)$$

with $\boldsymbol{x}$ here comprises the spatial coordinates $\boldsymbol{r}$ and spin σ. The HF exchange potential, $V_X^{HF}(\boldsymbol{x},\boldsymbol{x}')$, leads to the spatial separation between two electrons with equal spin. The exchange energy, E_X, is the reduction in the total energy resulting from the reduction of the Coulomb potential due to the above

spatial separation. Note that only semiconductors will be considered in this review, and all state summations, therefore, include the spin variable implicitly.

The correlation energy, E_C, is defined as the difference between the energy of the many-particle system and that calculated using the HF approach. It can be thought of as the further reduction in the total energy due the spatial separation of electrons with different spin. E_C is the most difficult term, and it is still an ongoing challenge in many-body theory.

III. Exchange - Correlation Functionals: LDA, GGA and Exact - Exchange

The DFT framework described in the previous section provides a practical tool for calculating the ground state properties of many-electron systems. This is largely due to the existence of accurate and well understood approximations for E_{XC}. The simplest and most widely used approximation is the LDA, proposed by Kohn and Sham [1]:

$$E_{XC}^{LDA}[\rho] = \int d\boldsymbol{r}\,\rho(\boldsymbol{r})\varepsilon_{XC}^{\text{hom}}(\rho(\boldsymbol{r})), \qquad (10)$$

where, $\varepsilon_{XC}^{\text{hom}}$ is the XC energy per particle of a homogeneous electron gas of density $\rho(\boldsymbol{r})$, which is known with a very high accuracy. Although it is supposed to be valid for slowly varying $\rho(\boldsymbol{r})$, LDA is proved to be remarkably successful for various properties of a wide range of systems. The reasons behind the success of LDA are thoroughly investigated [70]. However, it has several drawbacks. For solids, the general understanding is that LDA slightly underestimates the lattice parameter and overestimates the cohesive energy and bulk modulus. However, as noted in the introduction, the most serious shortcoming is the so-called band-gap problem.

The other widely used approximation is the generalized gradient approximation (GGA), where information about the local variation of $\rho(\boldsymbol{r})$ is taken into account:

$$E_{XC}^{GGA}[\rho] = \int d\boldsymbol{r}\,\rho(\boldsymbol{r})\varepsilon(\rho(\boldsymbol{r}), |\nabla\rho(\boldsymbol{r})|) . \quad (11)$$

Several GGA functionals have been devised, which try to satisfy as much as possible the properties and scaling rules of the exact E_{XC}

[71]. The main success of the GGA is a definite improvement in the cohesive energy of solids and molecules. Its performance for other properties, such as lattice parameter and bulk modulus of solids, is not impressive: the GGA results may even be worse than the LDA ones. As for the electronic structure, the differences between those calculated using LDA and GGA are marginal.

In principle, DFT is self-interaction free: for each electron the self-exchange energy [i.e, $i = j$ in Eq. (8)] cancels completely its self-Hartree one [Eq. (2), with $\rho_i(r)$ is used instead of $\rho(r)$]. Such a cancellation becomes incomplete when an approximation for E_X is adopted (while treating E_H exactly), leading to a spurious SI that is positive in nature [4]. The SI increases with the increase of the degree of localization of the electronic states. For example, the LDA eigenvalue of the 1s state of the H atom is about one half of the true value of 1 Ryd. Several methods have been introduced to remove or reduce the SI: (i) The self-interaction corrected LDA (SIC-LDA) of Perdew and Zunger [4] and its subsequent variants [7, 8, 72-74]. This is simply done by subtracting the interaction of each electron with its own charge density from the LDA (or the local spin-density (LSD) approximation) total energy. (ii) The LDA+U method [75], where the adjustable state dependent Hubbard U parameter is added locally to reduce the energies of the highly localized states. (iii) The use of hybrid functionals [76], which approximates the exchange potential as a linear combination of the corresponding non-local HF and local GGA potentials. (iv) The exact-exchange scheme within the KS-DFT method [9-11], which is practically SI free.

In the exact-exchange formalism within KS-DFT, E_X is calculated explicitly according to Eq. (8). The major difficulty here lies in the orbital dependence of E_X: note that V_X is defined as the first order variation of E_X with respect to $\rho(r)$, Eq. (4). This difficulty can be solved by using the chain rule:

$$V_X^{OEP}(\mathbf{r}) = \frac{\delta E_X}{\delta\rho(\mathbf{r})} =$$

$$\sum_i \iint \left[\frac{\delta E_X[\rho]}{\delta\varphi_i(r')} \frac{\delta\varphi_i(r')}{\delta V^{KS}(r'')} + c.c. \right] \frac{\delta V^{KS}(r'')}{\delta\rho(\mathbf{r})}. \quad (12)$$

As noted in Sec. I, this local exchange potential is equivalent to the optimized effective potential (OEP): the best local approximation to the HF non-local exchange potential [77]. The first derivative of Eq. (12) can be directly obtained from Eq. (8); the second derivative can be calculated using first order perturbation theory, while the third derivative is nothing but the inverse of the independent particle susceptibility,

$$\chi_o(\mathbf{r},\mathbf{r'}) = \delta\rho(\mathbf{r})\big/\delta V^{KS}(\mathbf{r'}). \quad (13)$$

See Ref. 11 for other technical details. We note here that the calculation of V_X^{OEP} is quite involved and expensive in terms of both CPU time and memory, compared to LDA. More
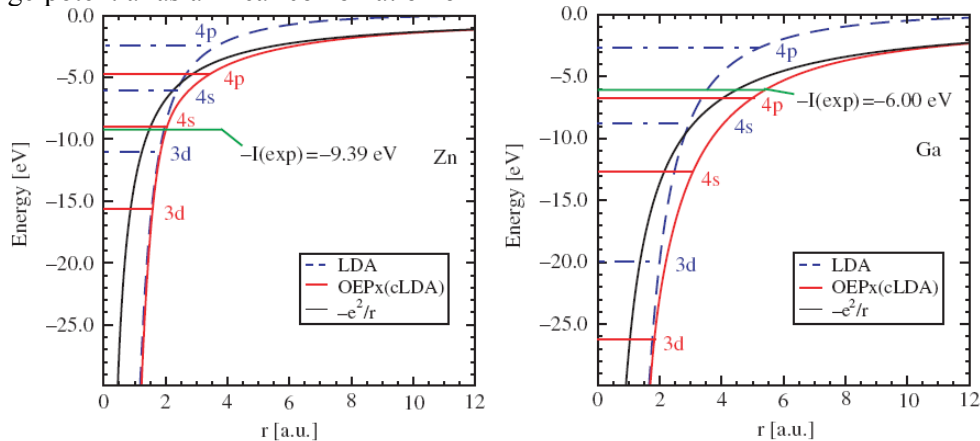
FIG.1. Effective Kohn–Sham potential for the neutral Zn (left panel) and Ga (right panel) atom: the OEPx(cLDA) potential (red line) reproduces the correct asymptotic decay$-e^2/r$ (black line), whereas the LDA (blue, dashed line) decays exponentially and thus underbinds the electrons. The atomic levels (shown as horizontal lines) are lowered in the OEPx(cLDA) approach compared to the LDA, resulting in good agreement with the experimentally measured ionization potential (green horizontal line). (Taken from Ref. 17).

136

efficient methods for calculating V_X^{OEP} have been recently introduced [78, 58].

The advantages of using the OEPx approach can be easily inferred from Fig. 1. First, the removal of the SI by this approach gives the correct asymptotic $-e^2/r$ behavior at large r. It is worth noting that, in this limit, the Coulomb potential of neutral atoms goes to zero, and the XC hole (which satisfies the sum rule: the XC hole density integrates to minus one electron) potential leads to the above asymptotic behavior. On the other hand, the LDA and GGA potentials go very rapidly to zero. Second, the removal of the SI by the OEOx(cLDA) approach improves dramatically the calculated valence eigenvalues. The difference between the LDA (blue lines) and OEOx(cLDA) (red lines) eigenvalues is due to the SI. The OEOx(cLDA) value of the highest valence state energy is very close to the negative of the experimental ionization energy, as expected. Third, The deeper OEOx(cLDA) potential increases the spatial localization of the valence states, compared to those of LDA, leading to a smaller overlap between them in the formation of solids. This leads, in turn, to larger band gaps and smaller band widths relative to those of LDA. This is shown in Fig. 2 for the band gaps of several semiconductors.
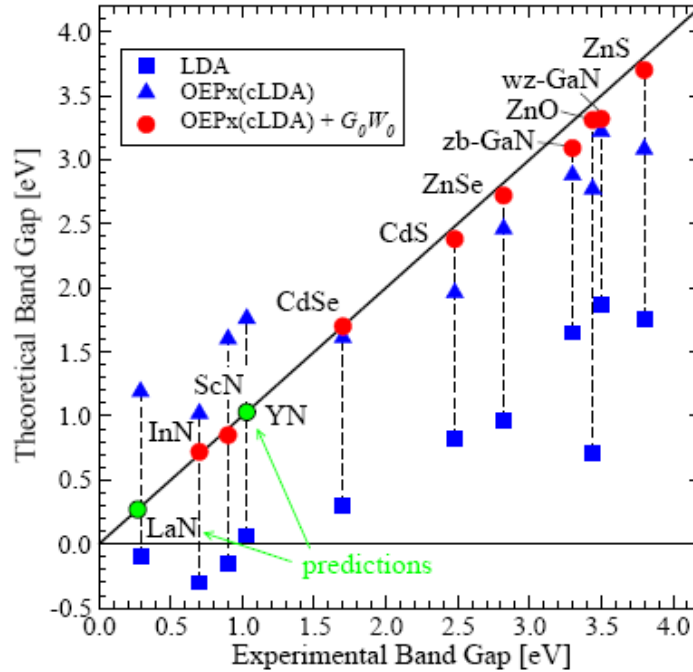
FIG. 2. Calculated *versus* experimental band gaps for selected II-VI compounds, group-III-nitrides and transition metal nitrides. The OEPx(cLDA)-G_0W_0 method consistently improves over LDA and OEPx(cLDA). For lack of experimental information on the band gap of YN and LaN, our predicted gaps have been placed on the diagonal. (Taken from Ref. 31).

IV. Quasiparticle GW Approach Based on Exact-Exchange KS-DFT Calculations

Via the field operator formalism, the many-body Hamiltonian can be transformed into a single-particle Hamiltonian [79]: $\hat{H}(\mathbf{r},\mathbf{r'};\varepsilon) = \hat{h}_o(\mathbf{r}) + \Sigma(\mathbf{r},\mathbf{r'};\varepsilon)$. All electron-electron interaction terms are rolled up in the non-local, energy-dependent self-energy operator (Σ) and the remaining contributions are given by $\hat{h}_o(\mathbf{r}) = \frac{1}{2}\nabla^2 + V_{ext}(\mathbf{r})$. The single particle Green's function

$$G(\mathbf{r},\mathbf{r'};\varepsilon) =$$

$$\lim_{\eta \to 0^+} \sum_s \frac{\psi_s(\mathbf{r}),\psi_s^*(\mathbf{r'})}{\varepsilon - (\varepsilon_s + i\eta\,\mathrm{sgn}(E_f - \varepsilon_s))} \qquad (14)$$

(where η is an infinitesimal positive energy) satisfies then the Dyson equation

$$G^{-1}(r,r';\varepsilon) = \left[\varepsilon - \hat{h}_0(r)\right]\delta((r-r') - \Sigma(r,r';\varepsilon). \tag{15}$$

By inserting Eq. (14) into (15), one immediately finds that ε_s and $\psi_s(\mathbf{r})$ are solutions to

$$\hat{h}_0(r)\psi_s(r) + \int dr'\Sigma(r,r';\varepsilon_s)\psi_s(r') \\ = \varepsilon_s\psi_s(r). \tag{16}$$

The poles of the Green's function therefore correspond to the real electron addition and removal energies ε_s and form a branch-cut infinitesimally above (below) the real energy axis for occupied (unoccupied) states.

To establish a link to photoemission of delocalized valence states, it is helpful to introduce Landau's concept of quasi-particles [80]. This new entity can be considered as a combination of an electron or a hole with its surrounding polarization cloud or, in other words, as the collective response of the interacting many-body system upon photoexcitation. Switching to the quasiparticle picture is consistent with analytically continuing the self-energy to the complex energy domain. Each of the quasi-particle poles (now at complex energy) represents the effect of many of the infinitesimally closely spaced poles just above (below) the real axis.

To solve the Dyson equation [Eq. (15)] for real systems, one typically applies Hedin's GW approximation [18] for the self-energy. Assuming that the quasi-particles interact only weakly via the screened Coulomb interaction W, the self-energy in the GW approach is then given as

$$\Sigma_{XC}^{GW}(r,r';\varepsilon) = \\ \frac{i}{2\pi}\int_{-\infty}^{\infty} d\varepsilon' e^{i\varepsilon'\delta}G(r,r';\varepsilon+\varepsilon')W(r,r';\varepsilon'), \tag{17}$$

where δ is an infinitesimal positive time. In practice, one starts from a system of non-interacting particles with energies ε_i and wavefunctions $\varphi_i(\mathbf{r})$. The non-interacting Green's function is defined analogous to Eq. (14) as

$$G_0(r,r';\varepsilon) = \\ \lim_{\eta\to 0^+}\sum_i \frac{\phi_i(r),\phi_i^*(r')}{\varepsilon - (\varepsilon_i + i\eta\,\mathrm{sgn}(E_f - \varepsilon_i))}. \tag{18}$$

The quantum state indices i and s are short for the composite of band index n and wave vector $\mathbf{k}$. In the random-phase approximation, the dielectric function,

$$\varepsilon(r,r';\varepsilon) = \\ \delta(r-r') - \int dr'' V(r-r'')\chi_0(r,r';\varepsilon) \tag{19}$$

is connected to the independent-particle polarizability,

$$\chi_0(r,r';\varepsilon) = \\ -\frac{i}{2\pi}\int_{-\infty}^{+\infty} d\varepsilon'' G_0(r,r'';\varepsilon'-\varepsilon)G_0(r,r'';\varepsilon')\chi_0 - r''$$

$$\tag{20}$$

and the bare Coulomb interaction,

$$V(r-r') = \frac{1}{|r-r'|}, \tag{21}$$

is screened by the inverse dielectric function

$$W_0(r,r';\varepsilon) = \int dr'' \varepsilon^{-1}(r,r'';\varepsilon)V(r''-r). \tag{22}$$

Separating the Hartree potential from the GW self-energy, and inserting Σ_{XC}^{GW} and the quasi-particle Green's function [Eq. (14)] into Eq. (15), the Dyson equation becomes

$$\left[\hat{h}_0(r) + V_H(r)\right]\psi_s(r) \\ + \int dr'\Sigma_{XC}^{GW}(r,r';\varepsilon_s)\psi_s(r') = \varepsilon_s\psi_s(r) \tag{23}$$

This equation, also referred to as quasi-particle equation, can be solved for the quasi-particle energies and wavefunctions.

Most commonly, the quasiparticle energies $\{\varepsilon_s^{qp}\}$ are determined using first order perturbation theory

$$\varepsilon_{nk}^{qp} = \varepsilon_{nk}^{DFT} \\ + <\phi_{nk}|\Sigma_{XC}^{G_0W_0}(\varepsilon_{nk}^{DFT}) - V_{XC} - \Delta\mu|\phi_{nk}>. \tag{24}$$

Here, G_0 and W_0 used to calculate $\Sigma_{XC}^{G_0W_0}$ are computed from a set of KS-DFT single-particle-energies and wave functions $\{\varepsilon_i^{DFT}, \phi_i^{DFT}\}$, and the constant $\Delta\mu$ is

introduced to align the Fermi energies before and after applying the GW self-energy corrections. Since G_0 and W_0 are not usually updated in a self-consistent manner, the so-calculated quasiparticle energies depend on the XC approximation used to calculate the input data. In the LDA-G_0W_0 approach, G_0 and W_0 are calculated from LDA data, while OEPx(cLDA) data are used in the OEPx(cLDA)-G_0W_0 method. As previously noted, the LDA-G_0W_0 results were found to accurately predict band gaps of *sp*-bonded semiconductors (with a typical error bar of 0.1 eV) [81]. However, complications arise when the LDA-G_0W_0 approach is used to calculate the electronic structure of semiconductors with *negative* LDA band gaps [21, 22] or when occupied shallow semicore *d* bands are treated as valence in the pseudopotential LDA-G_0W_0 framework [23-25]. We have found that OEPx(cLDA)-G_0W_0 method provides a reliable tool for band structure calculations of a wide range of semiconductors, including group-III nitrides [15, 17, 26-28], II-VI compounds [17, 29] and transition metal nitrides [30, 31], as shown in Fig. 2 and Table I.

Table I shows that the quasiparticle band gaps calculated using the OEPx(cLDA)-G_0W_0 approach are much superior than those of LDA-G_0W_0. This can be understood as

TABLE I. DFT and quasiparticle band gaps in eV for ZnO, ZnS, CdS and GaN in the zinc-blende structure compared to the experimental values. The calculations are performed using a pseudopotential plane-wave approach, with the semicore *d* electrons treated as valence. LDA calculations highly underestimate the band gap. The situation is improved by the quasiparticle LDA-G_0W_0 calculation, but the band gaps are still much smaller than the experimental values (see text). The OEPx(cLDA) approach leads to a significant opening of the band gap (relative to those of LDA), and OEPx(cLDA)-G_0W_0 results are in excellent agreement with experiment. (Taken from Ref. 29).

Method	ZnO	ZnS	CdS	GaN
LDA	0.51	1.76	0.81	1.65
LDA-G_0W_0	1.36	2.59	1.60	2.54
OEPx(cLDA)	2.34	2.94	1.84	2.76
OEPx(cLDA)-G_0W_0	3.11	3.70	2.39	3.09
Experiment	3.44	3.80	2.48	3.30

follows. It has been argued that wavefunctions of the semicore *d* electrons in the considered systems overlap strongly with those of the *s* and *p* electrons of the same shell. To obtain accurate quasiparticle band gaps within the pseudopotential LDA-G_0W_0 approach, the *entire* semicore shell should be included as part of the valence states [23-25], which makes these calculations highly expensive. Including instead only the semicore *d* electrons as valence results in large errors in the calculated band gaps, as is evident from Table I. On the other hand, these semicore *s* and *p* states are well described by the OEPx(cLDA) scheme, and hence they can be kept as part of the frozen core in the pseudopotential OEPx(cLDA)-G_0W_0 calculations. The other main advantage of the OEPx(cLDA)-G_0W_0 approach is the significant opening of the band gap arising from the removal of the self-interaction, compared to those of LDA, see above. This means that $V_{XC}^{OEPx(cLDA)}$ is closer to the self-energy operator Σ_{XC}^{GW} than V_{XC}^{LDA}, which leads to a better validity of the first order perturbation theory [Eq. (24)] used to calculate the quasiparticle energies.

As an example, we focus here on the band gap (E_g) of wurtzite (wz) InN. Experimentally, the widely accepted band gap (of 1.9 eV) has been recently questioned [82-84], and a value of about 0.7 eV has been measured in new high quality samples (low carrier concentration resulting from n-type doping). Moreover, the conduction electrons effective mass (m^*) of wz-InN is also found to depend strongly on the carrier concentration in the sample [27].

We show in Fig. 3 the calculated band structure of wz-InN in the vicinity of the band gap. The LDA calculations give incorrectly a negative band gap at the Γ point, which makes problematic the application of the LDA)-G_0W_0 method to this system [21,22]. On the other hand, the OEPx(cLDA) approach leads to sizable opening of the band gap, making wz-InN correctly a direct band gap semiconductor. The opening of the band gap in the latter approach is a direct consequence of the removal of the self-interaction: the energy of the relatively more localized upper valence states is lowered more than that of the lower conduction band
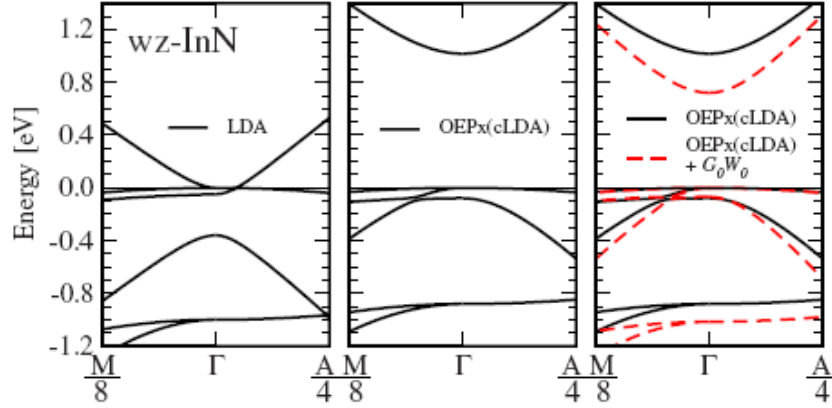
FIG. 3. LDA Kohn-Sham calculations incorrectly predict wurtzite InN to be a metal with the wrong band ordering at the Γ point. In OEPx(cLDA), the band gap opens and InN correctly becomes a semiconductor, thus providing a more suitable starting point for subsequent quasiparticle energy calculations in the G_0W_0 approximation. (Taken from Ref. 27).
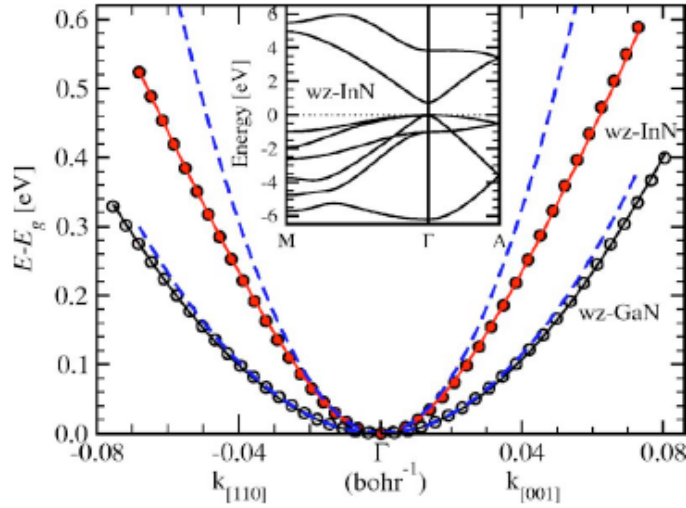
FIG. 4. Conduction band of wurtzite InN and GaN aligned at the bottom of the conduction band: the circles are the OEPx(cLDA)-G_0W_0 results, the solid lines the $\mathbf{k \cdot p}$ fit using Eq. (25), and the dashed lines the effective mass band (i.e, parabolic shape). The inset shows the band structure of wurtzite InN. (Taken from Ref. 27).

states. Finally, the quasiparticle correction to the OEPx(cLDA) band gap (using the OEPx(cLDA)-G_0W_0 scheme) leads to a band gap that is in excellent agreement with the recent experimental results [82-86].

To explain the sizable dependence of the band gap and conduction electrons effective mass of wz-InN on the carrier concentration (n-type), we use an analytic expression for the conduction band around the Γ point

$$E_c(k) = \frac{\hbar^2 k^2}{2m_o} + \frac{1}{2}\left(E_g^+ + \sqrt{(E_g^-)^2 + 4E_p \frac{\hbar^2 k^2}{2m_o}} \right) \quad (25)$$

derived from a four band $\mathbf{k \cdot p}$ model, neglecting spin-orbit splitting. Here, m_o is the free electron mass and $E_g^\pm = E_g \pm \Delta_1$, where Δ_1 is the crystal field splitting parameter of the upper three valence band states at the Γ point. The parameter E_p is related to the optical matrix elements between conduction and valence bands. Since it is the only unknown in Eq. (25), it has been determined by fitting to the OEPx(cLDA)-G_0W_0 conduction band. The calculated and fitted conduction bands around the Γ point are shown in Fig. 4, for wz-InN and wz-GaN. Using the OEPx(cLDA)-G_0W_0 values for Δ_1 and E_g, we find that the quasiparticle

140

conduction band of InN is well described by E_p of 9.0 eV (red solid line in Fig. 4).

Let us start first with the conduction electrons effective mass, m^*. In the spherical band approximation, the momentum effective mass

$$\frac{m^*(k_F)}{m_0} = \left(\frac{m_0}{\hbar^2 k_F} \frac{dE_c(k)}{dk} \bigg|_{k=k_F} \right)^{-1} \qquad (26)$$

can be translated into a carrier concentration dependent effective mass using the free electron relation $k_F = (3\pi^2 \rho)^{1/3}$, where ρ is the density of electrons in the conduction band. Fig. 5 shows the effective mass of wz-InN as a function of the free carrier concentration. The *ab initio* prediction (red line) extracted from our OEPx(cLDA)-G_0W_0 band structure by means of Eqs. (25) and (26) reproduces the experimental results very well and closely matches the curve obtained by Wu *et al.* with an experimentally deduced value of E_p =10 eV [Refs. 85 and 86 (black line)].

The n-type doping has also a direct consequence on the direct optical transitions $[E_g(\rho) = E_c(\rho) - E_v(\rho)]$ of wz-InN, which are shifted towards higher energies due to conduction band filling as the free electron concentration increases — the so-called Burnstein-Moss effect. Contributions from the electron-ion and electron-electron repulsions at high electron concentrations are accounted for following Wu *et al.* [85, 86]. The Burnstein-Moss shift calculated in this way fits very well a wide range of experimentally reported measurements, as shown in Fig. 6, and agrees well with the curve deduced by Wu *et al.* from their experimentally determined values of E_g and E_p. Neglecting the non-parabolicity of the conduction band (blue dashed line) worsens the agreement with the experimental results.

The excellent agreement between the OEPx(cLDA)-G_0W_0 results and experiment for the band gap of a wide range of semiconductors (Fig. 2) and in the delicate case of wz-InN (Figs. 5 and 6) reflects the high accuracy and predictive power of this method. This approach is nowadays one of the most advanced methods for band structure calculations.
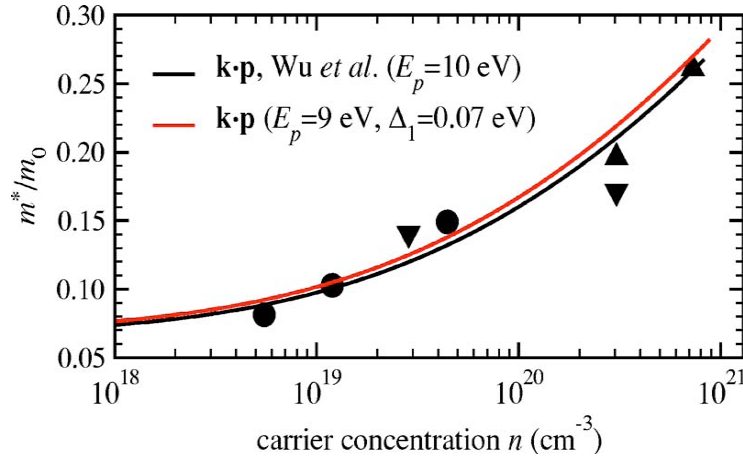

FIG. 5. The wz-InN effective mass as a function of carrier concentration, deduced from the OEPx(cLDA)-G_0W_0 calculations by means of Eqs. (25) and (26) [red line], agrees well with experimental measurements (symbols) and the **k·p** fit of Wu *et al.* (black line) based on the experimental data ([85, 86]). (Taken from Ref. 27).
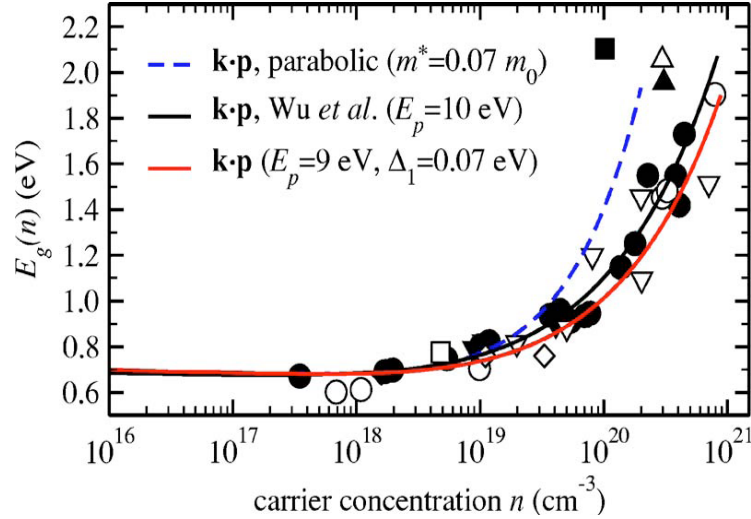
FIG. 6. Burnstein-Moss effect deduced from the OEPx(cLDA)-G_0W_0 band structure (red line) for wz-InN reproduces the experimental trend (symbols) very well and is also close to the **k·p** curve of Wu *et al.* (black line) [85, 86]. Assuming parabolic bands (dashed line) overestimates the Burnstein-Moss shift. (Taken from Ref. 27).

V. Elastic, Dielectric, Vibrational and Thermal Properties of Semiconductors from DFPT Calculations

Many properties of solids are defined as a response to an external perturbation. Here, we will focus on the perturbations that can be handled by the ABINIT computer package [87]: the atomic displacements (u_m) that preserve the crystal periodicity, homogeneous electric fields (E_α, where α denotes a Cartesian direction) and homogeneous strains (η_j, where $j = \{1...6\}$ in Voigt notation). The corresponding responses that are conjugate to these perturbations are (i) forces F_m, (ii) polarizations P_α and (iii) stresses σ_j, respectively. From a simultaneous application of a pair of these perturbations, one gets response functions of primary interest: $K_{mn} = dF_m / du_n$ (interatomic force-constant matrix), $\varepsilon_{\alpha\beta} = P_\alpha / E_\beta$ (dielectric susceptibility), $C_{jk} = d\sigma_j / d\eta_k$ (elastic constants), $Z^*_{m\alpha} = dP_\alpha / du_m$ (Born effective charge), $\Lambda_{mj} = dF_m / d\eta_j$ (internal strain) and $e_{\alpha j} = dP_\alpha / d\eta_j$ (piezoelectric response). These response tensors are nothing but second order derivatives of the total energy with respect to appropriate mixed perturbations. These energy derivatives can be efficiently calculated, within DFPT, by a variational technique similar to the one usually adopted to solve the KS equations. The force-constant

matrices can then be used to find the phonon modes over the entire Brillouin zone, which are the basic ingredient needed to calculate the thermal properties of solids.

V.A. Density functional perturbation theory

In the usual formulation of DFPT, the dependence of the electronic part of the total energy (E_{el}) on a parameter λ is developed as a power series in λ [35]:

$$X(\lambda) = X^{(0)} + \lambda X^{(1)} + \lambda^2 X^{(2)} + ... \qquad (27)$$

This power series expansion applies to other exact perturbed physics quantities: $\{\varphi\}$, $\{\varepsilon\}$, ρ, V_{ext}, T_0, H, … etc. Now, the second order derivative of E_{el} (or $E_{el}^{(2)}$) is stationary relative to variations in the first order derivative of $\{\varphi\}$, thanks to the 2n+1 theorem [88], and is given as

$$
\begin{aligned}
E_{el}^2\{\varphi^{(0)};\varphi^{(1)}\} = \sum_i^{occ} \Big[& <\varphi_i^{(1)}|(H^{(0)} - \varepsilon_i^{(0)})|\varphi_i^{(1)}> \\
& + (<\varphi_i^{(1)}|(T_0^{(1)} + V_{ext}^{(1)})|\varphi_i^{(0)}> + \\
& \quad <\varphi_i^{(0)}|(T_0^{(1)} + V_{ext}^{(1)})|\varphi_i^{(1)}>) \\
& + <\varphi_i^{(0)}|(T_0^{(2)} + V_{ext}^{(2)})|\varphi_i^{(0)}> \qquad (28) \\
& + \frac{1}{2}\iint \frac{\delta^2 E_{H,XC}}{\delta\rho(r)\delta\rho(r')}\rho^{(1)}(r)\rho^{(1)}(r')dr\,dr' \\
& + \int \frac{\partial}{\partial\lambda}\frac{dE_{H,XC}}{\delta\rho(r)}\Big|_{\rho^{(0)}} \rho^{(1)}(r)dr \\
& + \frac{1}{2}\frac{\partial^2 E_{H,XC}}{\partial\lambda^2}\Big|_{\rho^{(0)}}
\end{aligned}
$$

where $E_{H,XC}$ is the sum of the Hartree and XC energies, and $\rho^{(1)}$ is given by

$$\rho^{(1)}(\boldsymbol{r}) = \sum_i^{occ} \left[\varphi_i^{*(1)}(\boldsymbol{r})\varphi_i^{(0)}(\boldsymbol{r}) + \varphi_i^{*(0)}(\boldsymbol{r})\varphi_i^{(1)}(\boldsymbol{r}) \right].$$

(29)

Since $\{\varphi^{(0)}\}$ are already known from self-consistent calculations of the unperturbed system, $E_{el}^{(2)}$ is functional of only $\{\varphi^{(1)}\}$. The variation of $\{\varphi^{(1)}\}$ to minimize $E_{el}^{(2)}$ should be done subject to the constraint

$$< \varphi_i^{(1)} \mid \varphi_j^{(0)} >= 0$$

(30)

for all the occupied states i and j. Under such constraint, $\{\varphi^{(1)}\}$ satisfy the self-consistent Sternheimer equation [89], which is the Euler-Lagrange equation for this functional,

$$P_c \left(H^{(0)} - \varepsilon_i^{(0)} \right) P_c \mid \varphi_i^{(1)} >=$$
$$- P_c H^{(1)} \mid \varphi_i^{(0)} >$$

(31)

where P_c is the projector onto unoccupied states (conduction bands states) and

$$H^{(1)} = T^{(1)} + V_{ext}^{(1)} + V_{H,XC}^{(1)}, \text{ with}$$

$$V_{H,XC}^{(1)} = V_{H,XC0}^{(1)} + \int \frac{\delta^2 E_{H,XC}}{\delta\rho(\boldsymbol{r})\delta\rho(\boldsymbol{r}')}\rho^{(1)}(\boldsymbol{r}')d\boldsymbol{r}',$$

and

$$V_{H,XC0}^{(1)} = \frac{\partial}{\partial\lambda} \frac{\delta E_{H,XC}}{\delta\rho(r)}\bigg|_{\rho^{(0)}}.$$

(32)

Now, Eqs. (28) to (32) can be solved self-consistently, for example using the conjugate gradient technique, as nowadays usually done for solving the KS equations for $E_{el}^{(0)}$ and $\rho^{(0)}$ [Eqs. (1) to (5)].

The computation of response tensors described above involves mixed second derivatives of E_{el} with respect to two different perturbations, except the diagonal elements of the elastic tensor. In this case, Eq. (27) can be generalized as

$$E_{el}(\lambda_1, \lambda_2) = E_{el}^{(0)} + \lambda_1 E_{el}^{(\lambda_1)} +$$
$$\lambda_2 E_{el}^{(\lambda_2)} + \lambda_1\lambda_2 E_{el}^{(\lambda_1\lambda_2)} + \dots\dots$$

(33)

While stationary expressions for such mixed derivatives of E_{el} can be derived, they are usually calculated using the simpler nonstationary expression

$$E_{el}^{\lambda_1\lambda_2} =$$
$$\sum_i^{occ} \Big[< \varphi_i^{(\lambda_2)} \mid (T_0^{(\lambda_1)} + V_{ext}^{(\lambda_1)} + E_{H,XC}^{(\lambda_1)}) \mid \varphi_i^{(0)} >$$
$$+ (< \varphi_i^{(0)} \mid (T_0^{(\lambda_1\lambda_2)} + V_{ext}^{(\lambda_1\lambda_2)}) \mid \varphi_i^{(0)} >$$
$$+ \frac{1}{2}\frac{\partial^2 E_{H,XC}}{\partial\lambda_1\lambda_2}\bigg|_{\rho^{(0)}},$$

(34)

which requires the first-order wave functions for only one of the perturbations and just the non-self-consistent Hamiltonian terms for the other.

In the following subsection, we will describe briefly only the case of periodicity-preserving atomic displacement perturbations, which are used to calculate the interatomic force constant matrices. For homogeneous electric field and strain perturbations, interested readers may consult the original papers [35] and [37], respectively.

V.B. Periodicity-Preserving Atomic Displacements Perturbations

We start by noting that the unperturbed V_{ext} of a crystalline solid is periodic: $V_{ext}^{(0)}(\boldsymbol{r} + \boldsymbol{R}_a, \boldsymbol{r}' + \boldsymbol{R}_a) = V_{ext}^{(0)}(\boldsymbol{r}, \boldsymbol{r}')$, where $\boldsymbol{R}_a$ is a real space translation vector. To preserve this periodicity even for the perturbed potential, we consider a $\boldsymbol{q}$-dependent perturbing potential operator of the form [35]

$$V_{ext,\boldsymbol{q}}^{(!)}(\boldsymbol{r} + \boldsymbol{R}_a, \boldsymbol{r}' + \boldsymbol{R}_a) = e^{i\boldsymbol{q}.\boldsymbol{R}_a}V_{ext}^{(1)}(\boldsymbol{r}, \boldsymbol{r}').\ (35)$$

It should be noted that such a perturbing potential is non-Hermitian and should be always used in conjunction with its Hermitian conjugate counterpart, written as $V_{ext,-\boldsymbol{q}}^{(!)}$ (since its wave vector is $-\boldsymbol{q}$), as well as a complex expansion parameter λ, such that

$$V_{ext}(\lambda) = V_{ext}^{(0)} + (\lambda V_{ext,\boldsymbol{q}}^{(1)} + \lambda^* V_{ext,-\boldsymbol{q}}^{(1)})$$
$$+ (\lambda^2 V_{ext,\boldsymbol{q},\boldsymbol{q}}^{(2)} + \lambda\lambda^* V_{ext,\boldsymbol{q},-\boldsymbol{q}}^{(2)}$$
$$+ \lambda^*\lambda V_{ext,-\boldsymbol{q},\boldsymbol{q}}^{(2)} + \lambda^{*2} V_{ext,-\boldsymbol{q},-\boldsymbol{q}}^{(2)}) + \dots\dots$$

(36)

and a similar form applies for $E_{el}(\lambda)$:

$$E_{el}(\lambda) = E_{ext}^{(0)} + (\lambda E_{el,q}^{(1)} + \lambda^* E_{el,-q}^{(1)})$$
$$+ (\lambda^2 E_{el,q,q}^{(2)} + \lambda\lambda^* E_{el,q,-q}^{(2)} \qquad (37)$$
$$+ \lambda^*\lambda E_{el,-q,q}^{(2)} + \lambda^{*2} E_{el,-q,-q}^{(2)}) + \ .....$$

Now, when q is not a vector of the reciprocal lattice, the requirement of invariance under translation of the whole system leads to [35]

$$E_{el,q}^{(1)} = E_{el,-q}^{(1)} = 0 \quad , \qquad (38)$$

and when $2q$ is not a vector of the reciprocal lattice, one gets

$$E_{el,q,q}^{(2)} = E_{el,-q,-q}^{(2)} = 0 \quad . \qquad (39)$$

Thanks to these equations, it can be shown that $E_{el,q,-q}^{(2)}$ is a real quantity, variational with respect to $\{\varphi^{(1)}\}$. Thus, $E_{el,q,-q}^{(2)}$ is calculated by applying the minimization technique of the preceding section, see Ref. 35 for further details.

V.C. Dynamical Matrix and Phonon Frequencies

To construct the dynamical matrix, one considers unit displacements of atoms in sublattice κ, along the α axis, multiplied by the infinitesimal λ (eventually, a complex quantity) and by a phase varying with the cell to which the atoms belong; the α component of their vector position is changed from $\tau_{\kappa,\alpha} + R_{\kappa,\alpha}$ to $\tau_{\kappa,\alpha} + R_{\kappa,\alpha} + \lambda e^{iq.R_a}$, with q wave vectors restricted inside the Brillouin zone. Atoms in the other sublattices are not displaced. These collective displacements are consistent with the one considered above [Eq. (35)], and hence preserve the periodicity of the unperturbed potential. For such displacements, expressions for the first and second order changes in V_{ext} are given in Ref. 35 and then used to evaluate the second order changes of E_{el} for such perturbations, $E_{el,-q,q}^{\tau_{\kappa\alpha}^* \tau_{\kappa'\beta}}$, as described above. Finally, the second order changes of ion-ion energy are added to $E_{el,-q,q}^{\tau_{\kappa\alpha}^* \tau_{\kappa'\beta}}$ to find the corresponding changes of the total energy, $E_{tot,-q,q}^{\tau_{\kappa\alpha}^* \tau_{\kappa'\beta}}$, which are the main ingredient of the dynamic matrix as we will show below.

On the other hand, the total energy of a periodic crystal with small lattice distortions from the equilibrium positions can be expressed as

$$E_{tot}(\{\Delta\tau\}) = E_{tot}^{(0)} +$$
$$\sum_{a\kappa\alpha} \sum_{b\kappa'\beta} \frac{1}{2}\left(\frac{\partial^2 E_{tot}}{\partial\tau_{\kappa\alpha}^a \partial\tau_{\kappa'\beta}^b}\right)\Delta\tau_{\kappa\alpha}^a \Delta\tau_{\kappa'\beta}^b + ..., \qquad (40)$$

where $\Delta\tau_{\kappa\alpha}^a$ is the displacement along direction α of the atom κ in the cell labeled a (with vector R_a), from its equilibrium position τ_κ^a.

The matrix of the interatomic force constants (IFCs) is defined as

$$K_{\kappa\alpha,\kappa'\beta}(a,b) = \left(\frac{\partial^2 E_{tot}}{\partial\tau_{\kappa\alpha}^a \partial\tau_{\kappa'\beta}^b}\right) \qquad (41)$$

and its Fourier transform is

$$\tilde{K}_{\kappa\alpha,\kappa'\beta}(q) = \frac{1}{N}\sum_{ab} K_{\kappa\alpha,\kappa'\beta}(a,b)e^{-iq.(R_a - R_b)}$$
$$= \sum_b K_{\kappa\alpha,\kappa'\beta}(,b)e^{iq.R_b} \qquad (42)$$

where N is the number of cells of the crystal. It should be noted that $\tilde{K}_{\kappa\alpha,\kappa'\beta}(q)$ is connected to the second-order derivative of the total energy with respect to collective atomic displacements

$$\tilde{K}_{\kappa\alpha,\kappa'\beta}(q) = 2E_{tot,-q,q}^{\kappa\alpha,\kappa'\beta} \qquad (43)$$

and it is the main ingredient of the dynamical matrix

$$\tilde{D}_{\kappa\alpha,\kappa'\beta}(q) = \tilde{K}_{\kappa\alpha,\kappa'\beta}(q)/(M_\kappa M_{\kappa'})^{1/2} \qquad (44)$$

where M_κ is the mass of the κth atom.

The vibration frequencies $[e_\kappa(q|j)]$ and polarization vectors of the phonon modes with wave vector q are determined by solving the eigenvalue matrix equation

$$\sum_{\kappa'\beta} \tilde{D}_{\kappa\alpha\kappa'\beta}(q)e_{\kappa'\beta}(q|j) = \omega_{q,j}^2 e_{\kappa\alpha}(q|j). \qquad (45)$$

For polar compounds, the macroscopic electric field, caused by the long-range character of the Coulomb forces, contributes to the longitudinal optical phonons in the long wavelength ($q{\to}0$) limit. This effect is

included by calculating the nonanalytical part $(\widetilde{K}^{na})$ of the force constants, given by [35]

$$\tilde{K}^{na}_{\kappa\alpha\kappa'\beta} = \frac{4\pi e^2}{\Omega_0} \frac{\sum_{\beta'}(Z^*_{\kappa,\beta',\alpha}q_{\beta'})\sum_{\alpha'}(Z^*_{\kappa,\alpha',\beta}q_{\alpha'})}{\sum_{\alpha'\beta'}q_{\alpha'}\varepsilon_{\infty\alpha',\beta'}q_{\beta'}} \quad (46)$$

where, Z^* and ε_{∞} are, respectively, the Born effective charges and the macroscopic high-frequency static dielectric tensors (see above) which are also calculated self-consistently using DFPT.

For a *nonpolar* material, the dynamical matrix is analytic in reciprocal space and the real space IFCs are quite short ranged (i.e., negligible beyond a certain range R_{max}). In this case, the IFCs can be obtained by Fourier transformation of $\widetilde{K}_{\kappa\alpha,\kappa'\beta}(\boldsymbol{q})$ computed on a regular discrete mesh in $\boldsymbol{q}$ space of spacing $\Delta q \leq 2\pi / R_{max}$. The so obtained IFCs can be used to compute the dynamical matrices at any arbitrary $\boldsymbol{q}$ point (i.e., a point not contained in the original grid). In case of a polar material, the dynamical matrix displays a nonanalytic behavior in the $\boldsymbol{q}\rightarrow 0$ limit, see above. Therefore, the nonanalytic contribution [Eq. (46)] is subtracted from the $\tilde{K}_{\kappa\alpha,\kappa'\beta}(\boldsymbol{q})$ at each $\boldsymbol{q}$ point in the grid. Fourier transforming these modified $\widetilde{K}_{\kappa\alpha,\kappa'\beta}(\boldsymbol{q})$ gives the short-ranged IFCs.

We have used DFPT to investigate the phonon spectra of several semiconductors [39-41] under zero and high pressures. As an example, we will focus here on those of ZnSe (a wide band gap semiconductor) [40]. Fig. 7 depicts the phonon spectra of ZnSe at zero and 9 GPa pressures. The most important feature to note here is the excellent agreement with experiment. The pressure variation of phonon spectra of ZnSe depicted by the mode Grüneisen parameter of ZnSe, defined as $\gamma_{j,q} = -(d \ln \omega_{j,q}(V)/d \ln V)$, is shown in Fig. 8. This figure shows that the optical and longitudinal acoustical (LA) branches are shifted up in frequency while the transverse acoustical (TA) branches experience a downward shift. We will show below that such a behavior has a direct impact on the thermal properties of ZnSe, especially in the case of thermal expansion.

Also shown in Fig. 7 are the results obtained with the semicore $3d$ electrons of Zn treated as part of the frozen core and including the non-linear exchange-correlation corrections (NLCC) [91]. The relaxation of the semicore d electrons is clearly required for highly accurate theoretical determination of the phonon spectra of IIB-VI compounds. However, their effects are rather small, and hence these electrons can be treated as part of the frozen core for computing the phonon spectra of big systems (large unit cells) involving group-II elements.
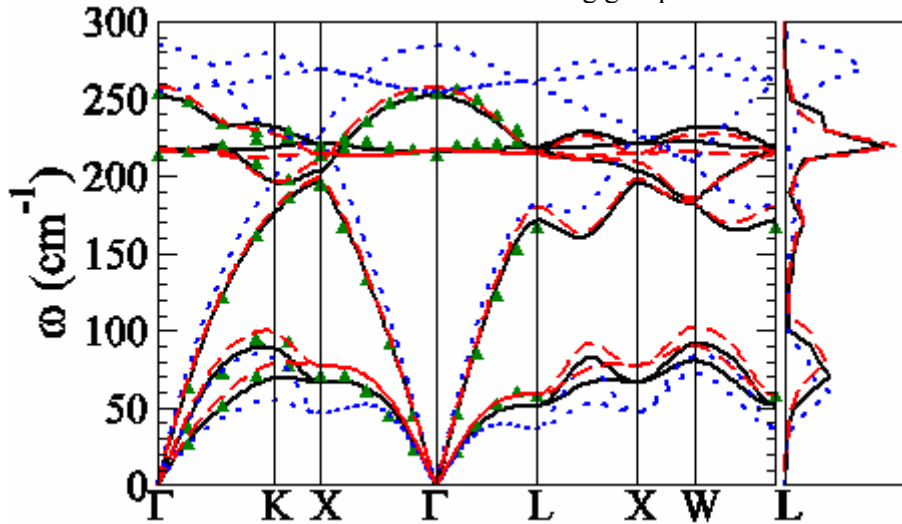

FIG. 7. Phonon spectra and density of states of ZnSe, at zero (solid lines) and 9 GPa (dotted lines) pressures. The calculated phonon spectra at zero pressure are in excellent agreement with the experimental data (triangles), obtained using inelastic neutron scattering [90]. NLCC calculations (see text) at zero pressure are shown with dashed lines. (Taken from Ref. 40).
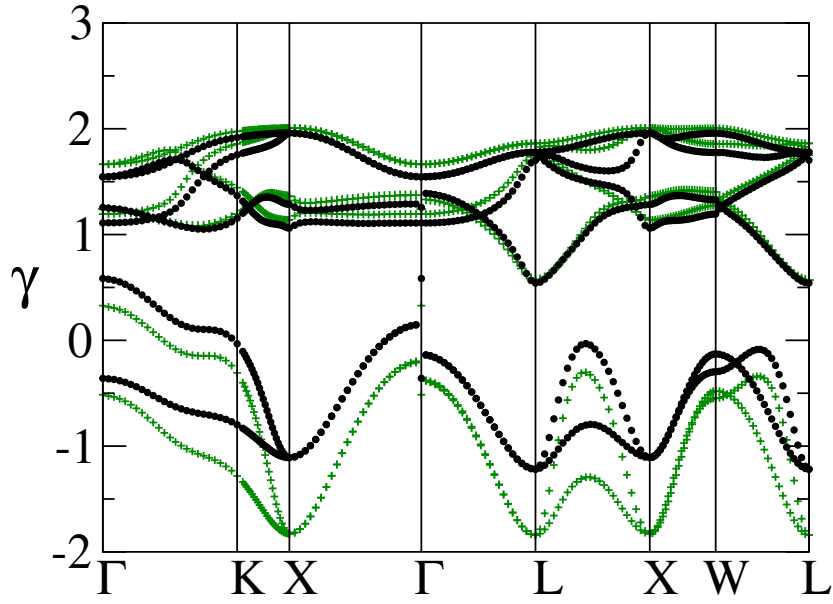
FIG. 8. Mode Grüneisen parameter of ZnSe, along several high symmetry directions of the fcc lattice, with (crosses) and without (circles) including the semicore $3d$ electrons of Zn as valence electrons. (Taken from Ref. 40).

For such a cubic material, the Born transverse effective charge tensor Z^* is isotropic. Because of the charge neutrality, the effective charge $Z^* = \mathrm{Tr}\, Z^*/3$ of the anions is minus that of the cations. The zero pressure value of Z^* of the cations of ZnSe is 2.026 (2.00) for $3d$ (NLCC) calculation, which is in excellent agreement with the experimental value of 2.03. On the other hand, the calculated zero pressure value of $\varepsilon_\infty = \mathrm{Tr}\, \varepsilon_\infty / 3$ of ZnSe is 7.53, which is considerably higher than the experimental value of 6.3. However, our NLCC value of 6.59 is in good agreement with the experiment and other similar theoretical results.

V.D. Equation of State, Thermal Expansion and Heat Capacity in the Quasiharmonic Approximation

The knowledge of the entire phonon spectrum of a given system enables the calculation of its thermodynamic properties and the relative stability of its different phases as functions of T. The thermodynamic properties are usually determined by the appropriate thermodynamic potential relevant to the given ensemble. In the ensemble where the sample volume (V) and T are independent variables, the relevant potential is the Helmholtz free energy (F). In the adiabatic or Born-Oppenheimer approximation, F of a semiconductor can be written as

$$F = E_{tot} + F_{vib} = E_{tot} + E_{vib} - TS_{vib}, \qquad (47)$$

where E_{vib} and S_{vib} is the contribution of the lattice vibration to the internal energy and entropy (S), respectively. The electronic entropy contribution to S, vanishes identically for insulators, and thus, it is not included in Eq. (47). Even for metals, this contribution is usually neglected, although it is easy to calculate. Thus, the key quantity to calculate in order to have access to the thermal properties and to phase stability is F_{vib}.

F_{vib} is usually calculated within the quasiharmonic approximation (QHA). This means calculating F_{vib} in the harmonic approximation, retaining only the implicit V dependence through the phonon frequencies, and it is given as

$$F_{vib}(T,V) = k_B T \sum_{j,q} \ln(2\sinh(\hbar\omega_{j,q}(V)/2k_B T)$$

$$(48)$$

The QHA accounts only partially for the effects of anharmonicity. However, QHA is found to be a very good approximation at temperatures not too close to the melting point.
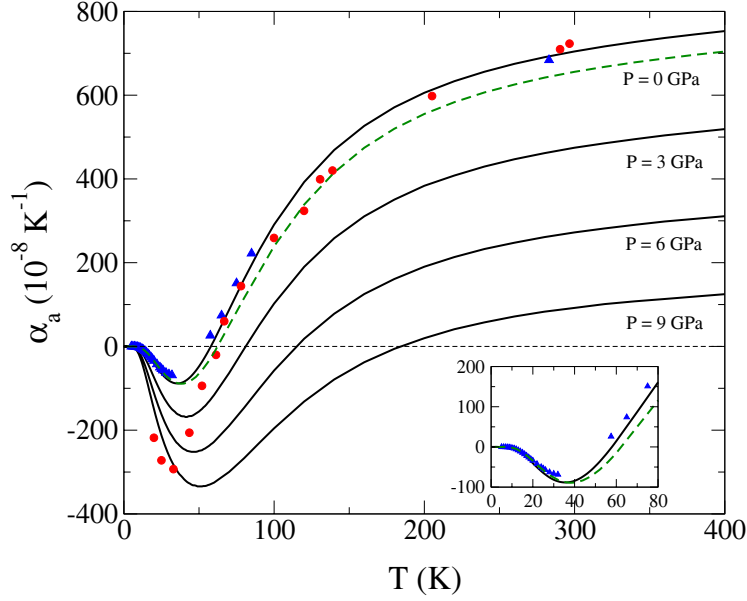
146

FIG. 9. Linear thermal expansion coefficient of ZnSe as a function of temperature, at different pressures. Solid lines: semicore 3d electrons treated as valence. Dashed line: NLCC calculations. At zero pressure, our results are in excellent agreement with the recent experimental results (Triangles: Ref. 94), which differ from previous experimental data (Circles: Ref. 95) at low temperatures. Inset: data in the temperature range of 0–80 K, at zero P. (Taken from Ref. 40).

For given T and V, the equilibrium state of a crystal is determined by minimizing F with respect to all possible degrees of freedom. The equation of state (P versus V) of the system is obtained by equating P to minus the derivative of F with respect to V at constant T, or

$$P = -(\partial F / \partial V)_T . \qquad (49)$$

The thermal expansion can be directly obtained from the equation of state, and the volume thermal expansion coefficient is defined as

$$\alpha_V = \frac{1}{V}\left(\frac{\partial V}{\partial T}\right)_P . \qquad (50)$$

The linear thermal expansion coefficient for cubic crystals is given as

$$\alpha_a = \frac{1}{3}\alpha_V . \qquad (51)$$

Due to anharmonicity effects, the heat capacity at constant P (C_P) is different from that at constant volume (C_V). The former, which is what experiments directly determine, is proportional to T at high T, while the latter goes to a constant which is given by the classical equipartition law: $C_V =$ $3Nk_B$, where N is the number of atoms in the system. The relation between C_P and C_V is [92]

$$C_P - C_V = \alpha_V^2(T)B_0VT, \qquad (52)$$

where B_0 is the bulk modulus. Within QHA, C_V is given as [88]

$$C_V(T) = \sum_{q,j} c_{q,j}^V(T) = $$
$$k_B \sum_{q,j}\left(\frac{\hbar\omega_{q,j}(V)}{2k_BT}\right)^2 \frac{1}{\sinh^2[\hbar\omega_{q,j}(V)/2k_BT]}, \qquad (53)$$

where $c_{q,j}^V(T)$ is the contribution to C_V of the j,$\mathbf{q}$ phonon mode at a certain T. The linear thermal expansion can be expressed in terms of $c_{q,j}^V(T)$ and $\gamma_{q,j}$ as [93]

$$\alpha_a(T) = \frac{1}{3B_0V}\sum_{q,j}\gamma_{q,j}c_{q,j}^V(T). \qquad (54)$$

We have calculated the thermal properties of some semiconductors [40, 41], under zero and high pressures, at the level of LDA. As an example, we show in Figs. 9 and 10 the thermal expansion and heat capacity of ZnSe [40], respectively. The success of LDA in

describing such properties is clearly evident. The most interesting feature to note here is the dramatic increase in the temperature range of negative thermal expansion of ZnSe under hydrostatic compression. The negative thermal expansion can be understood as follows. At low T, the excited phonon modes are predominantly of TA type with negative $\gamma_{j,q}$ [see Eq. (54) and Fig. 8], giving negative values of α_a. Moreover, as shown above, the hydrostatic pressure leads to a decrease in the

frequency of the TA phonon modes and to an increase in that of the other modes. Thus, at high P and low T, the predominance of the TA phonon modes becomes increasingly more pronounced, leading to an increase in the range of T where α_a is negative and to a reduction in its calculated values. The calculated $C_V(T)$ of ZnSe is also in excellent agreement with experiment, and it is much less sensitive to pressure than α_a.
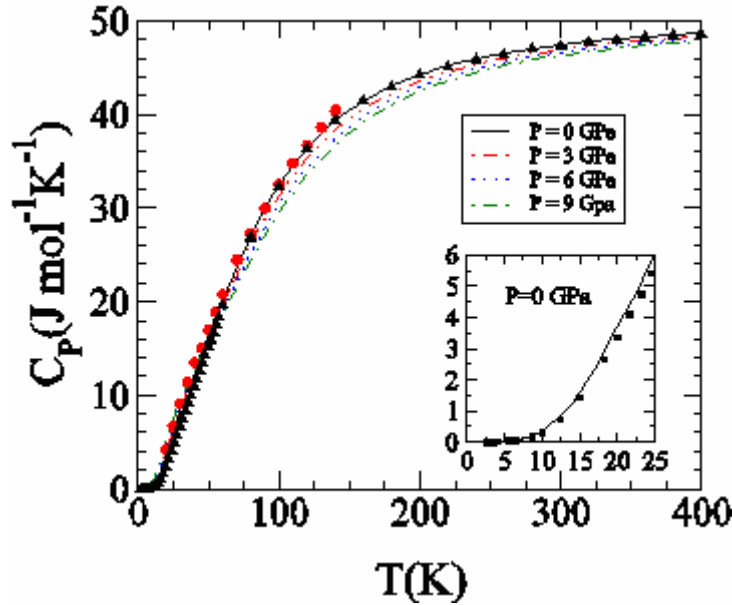

FIG. 10. As in Fig. 9, but for heat capacity at constant pressure. Triangles: NLCC calculations. Circles: experimental data of Ref. 96. Squares: experimental data of Ref. 97. Inset: data in the temperature range of 0–25 K, at zero P. (Taken from Ref. 40).

The presented phonon spectra and thermal properties of ZnSe can be considered as examples on the accuracy of the LDA calculations, described in Sec. III, for many physical and chemical properties of a wide range of systems.

VI. Wannier Functions: Recent Developments and Applications

As noted in Sec. I, the non-uniqueness property of the localized Wannier functions (WFs) has dramatically limited their applications. Thus, the most important development in this field is the introduction of unique maximally localized WFs (MLWFs), by Marzari and Vanderbilt [53]. The MLWFs have already found interesting applications [54-67]. In this section, we provide a brief description of MLWFs, and

focus on the novel bond ionicity scale based on the center of the MLWFs [67].

VI.A. Maximally localized Wannier functions

The electronic states in periodic systems are usually described in terms of extended Bloch orbitals

$$\varphi_{nk}(\boldsymbol{r}) = u_{nk}(\boldsymbol{r})e^{ik.r}, \qquad (55)$$

where $u_{n,k}(\mathbf{r})$ are periodic functions with the periodicity of the crystal. The Bloch orbitals are characterized by two quantum numbers: the wave vector inside the first Brillouin zone (BZ), $\boldsymbol{k}$, and the band index n. An alternative representation is in terms of localized real-space orbitals or Wannier functions (WFs), $|\mathbf{R}n>$, which are characterized by real-space translation vectors $\mathbf{R}$ and n. The WFs can be

constructed from the extended Bloch orbitals according to

$$| \boldsymbol{R}n > = \frac{V_{cell}}{(2\pi)^3} \int_{BZ} | \varphi_{n,\boldsymbol{k}} > e^{i\zeta_n(\boldsymbol{k}) - i\boldsymbol{k}.\boldsymbol{r}} d\boldsymbol{k}, \quad (56)$$

where $\zeta_n(\boldsymbol{k})$ is an arbitrary periodic phase factor in the reciprocal lattice. Such phase factors, which do not affect the physical properties extracted from Bloch's orbitals, lead to the non-uniqueness of the WFs.

Marzari and Vanderbilt [53] have exploited the above non-uniqueness property to construct MLWFs. This has been done by writing

$$| \boldsymbol{R}n > = \frac{V_{cell}}{(2\pi)^3} \int_{BZ} \sum_{m=1}^{N} U_{mn}^{(\boldsymbol{k})} | \varphi_{n,\boldsymbol{k}} > e^{-i\boldsymbol{k}.\boldsymbol{R}} d\boldsymbol{k}, (57)$$

where $U_{mn}^{(\boldsymbol{k})}$ are unitary matrices of dimension N (number of occupied states). Then, the optimal set of $U_{mn}^{(\boldsymbol{k})}$ is obtained by minimizing a spread function given as

$$\Omega = \sum_{n} < 0n | r^2 | 0n > - < 0n | \boldsymbol{r} | 0n >^2 . \quad (58)$$

The expectation value $\boldsymbol{r}_n = < 0n | \boldsymbol{r} | 0n >$ defines the centers of the MLWFs. An elegant iterative scheme for minimizing Ω has been introduced by Marzari and Vanderbilt [53].

In our work [67], we followed the procedure of Ref. 53 to construct the MLWFs of 32 $A^N B^{8-N}$ compounds, with $N = 1, 2, 3$ and 4, in their ground-state structures [diamond, zincblende (ZB), or rocksalt (RS)]. The considered systems consist of 3 of group-IV elemental solids in the diamond structure, the cubic phase of SiC, 15 III–V compounds in the ZB structure, 4 IIB–VI compounds in the ZB structure, 4 IIA–VI compounds in the RS structure and 4 I–VII compounds in the RS structure.

Let us first start with the elemental group-IV solids (Si, Ge and α-Sn) in the diamond structure. For such systems, there are four bonding MLWFs per primitive unit cell since there are eight valence electrons filling completely four valence bands. This means that there is a symmetric MLWF associated with each bond, as shown in Fig. 11, in the case of Si. The center of the MLWF coincides with that of the corresponding bond. The

relative position of the center of the MLWF is defined as $\beta = r_n / d$, where r_n is the distance between $\boldsymbol{r}_n$ and the position of the cation of the associated bond and d is the bond length. Thus, for elemental group-IV solids, $\beta = 0.5$.

For the $A^N B^{8-N}$ compounds crystallizing in the ZB structure, the mean features of the MLWFs are quite similar to those of the elemental group-IV solids. However, in the ZB form, the two atoms at the ends of each bond have different electronegativities, which leads to a partial charge transfer from the cation to the anion regions. This, in turn, shifts the center of the MLWFs away from the center of the bond toward the anion, as illustrated in Fig. 12, in the case of GaN. Therefore, the values of β of these systems are larger than 0.5. We have demonstrated (see next subsection) that there is a strong correlation between $(\beta - 0.5)$ and the bond ionicity [67], as expected. Based on this fact, an ionicity scale will be introduced in the next subsection.

For the more ionic I–VII and IIA–VI compounds crystallizing in the sixfold coordinate RS phase, the situation is quite different; the one-to-one correspondence between the bonding MLWFs and bonds breaks down. In the RS structure, the four bonding MLWFs, per primitive unit cell, correspond to six bonds. Because of the large bond ionicity of these compounds, one expects the MLWFs to be centered near the anions. Our calculations have shown that the centers of the MLWFs lie along four of the eight [111] directions of the cubic crystals, very close to the anions, as shown in Fig. 13, in the case of NaCl. It is interesting to note that, with respect to the anions, the MLWFs in the RS phase have the same orientation as those in the ZB phase (along the bonds of the latter structure). Moreover, it is meaningful to consider that each MLWF is a superposition of three somehow "optimized" σ-bond orbitals of the three neighboring bonds (see Fig. 13). Thus, each bond yields two thirds of an MLWF, which is the same ratio between the number of MLWFs and the bonds in the RS structure. To find the value of β of the relevant compounds, we consider one of the above "optimized" σ-bond orbitals and take its center to be the component of the center of any of the two associated MLWFs along the corresponding bond.
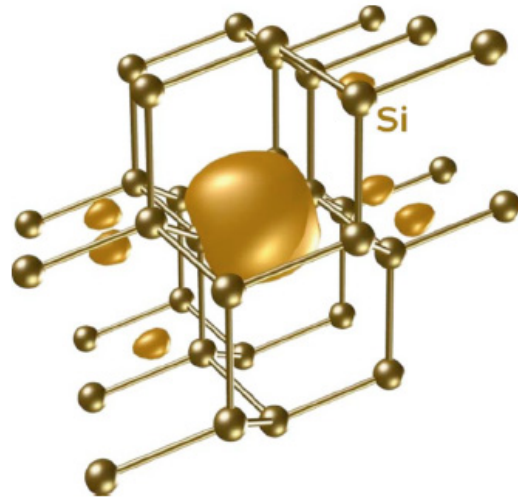
FIG. 11. An isosurface of a maximally localized Wannier function of Si in the diamond. (Taken from Ref. 67).
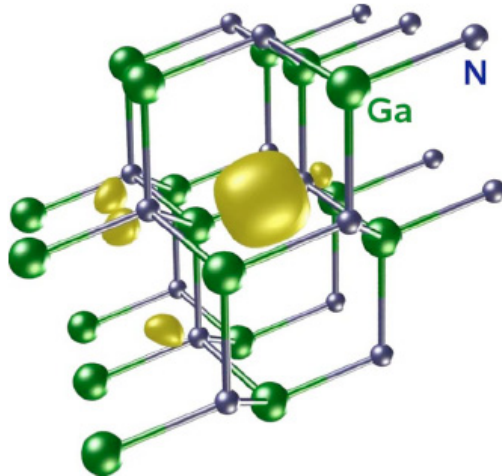

FIG. 12. An isosurface of a maximally localized Wannier function of GaN in the zinc-blende structure. (Taken from Ref. 67).
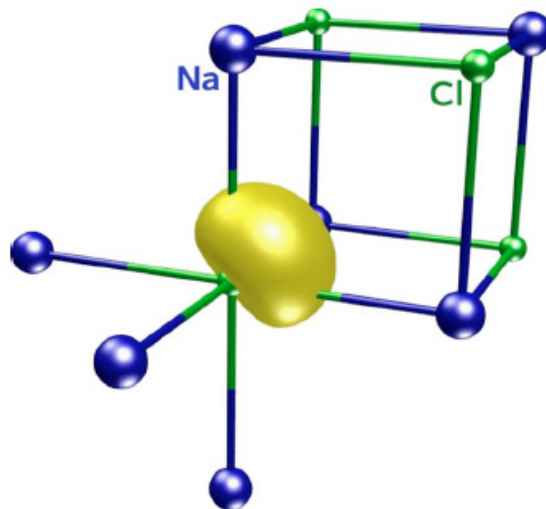

FIG. 13. An isosurface of a maximally localized Wannier function of NaCl in the rocksalt structure. (Taken from Ref. 67).

VI.B. A Novel Bond Ionicity Scale Based on the Centers of Mlwfs

As noted in the previous subsection, there is a strong correlation between the deviation of $\mathbf{r}_n$ from the bond center [expressed by (β − 0.5)] and the bond ionicity (see Fig. 14). This, in turn, shows that (β − 0.5) can be used as a measure for the bond ionicity. To devise a bond ionicity scale based on (β − 0.5), it is important to realize that we are dealing with a bond property in the solid phase of the material. Therefore, the concept of resonant bonds of Pauling [98] also applies to the present case. This implies that such an ionicity scale should also depend on the valency N and coordination number M. After several attempts, we found that the best ionicity scale takes the form

$$w_i = (2\beta - 1)^{(N/M)} . \qquad (59)$$

A remarkable feature of this ionicity scale is that it involves only physical constants.

The previous *ab initio* ionicity scales are extracted from either the charge density (Ref. 99), g, or band structure parameters (Ref. 100), f_i^*. It is worth noting that these are properties of the solid as a whole. The same can be said about the most famous empirical ionicity scale of Phillips [101], f_i, which is based on the dielectric theory of Phillips and Van Vechten. Thus, a major advantage of our ionicity scale is that it is directly derived from a bond related, see above.

A comparison between the present ionicity scale and previous empirical [101] and *ab initio* ones [99,100] is shown in Fig. 15. The important features to note from this figure are: (i) The quite large scattering of the previous values of bond ionicity. (ii) The w_i provides almost a best fit to the previously available values. This reflects the accuracy and reliability of the w_i bond ionicity scale. Moreover, we have shown [67] that the critical value of the bond ionicity that separates the fourfold (ZB or wurtzite) and sixfold (RS) coordinate structures is found to be of about 0.7.
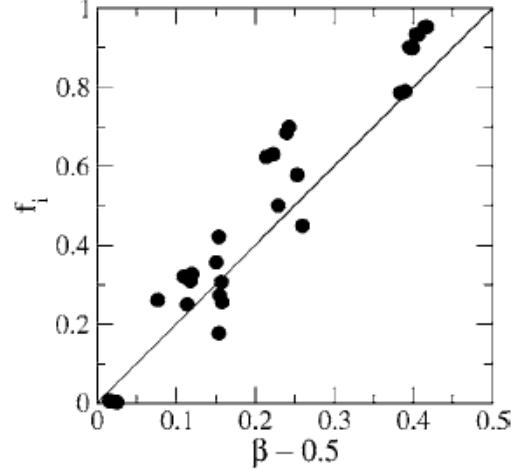

FIG. 14. The Phillips bond ionicity (f_i) vs (β−0.5) for the considered $A^N B^{8-N}$ compounds. Those of the elemental group-IV solids are not shown. (Taken from Ref. 67).
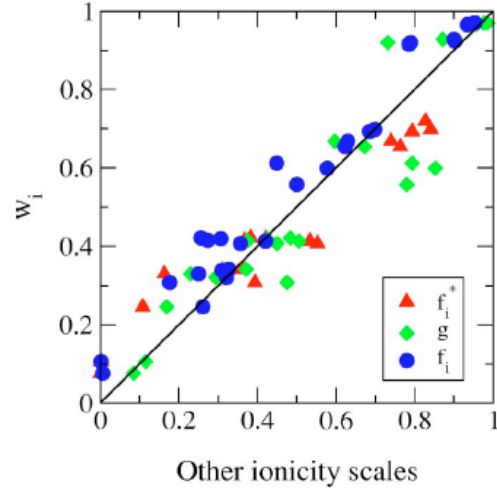
Fig. 15. The present bond ionicity w_i vs those of Phillips (Ref. 101), f_i, Garcia and Cohen (Ref. 99), g, and Christensen *et al.* (Ref. 100), f_i^*. (Taken from Ref. 67).

VII. Summary

Advances in modern computational electronic structure techniques, mainly based on Kohn-Sham density functional theory (KS-DFT), have made them the most attractive and widely used theoretical methods for investigating many properties of a wide range of systems. They are currently being used to tackle fundamental problems in physics, chemistry, geology, material science and biology. The great success of these theoretical approaches can be attributed to four main reasons.

(i) Their accuracy and high predictive power. This is demonstrated in this review article by presenting results in excellent agreement with experiment for the electronic structure, phonon spectra, dielectric and thermal properties of semiconductors. Moreover, these parameter free approaches enable us to get a deeper understanding and faithful explanation of the experimental results and allow us to study the properties of systems which are either unstable or not yet experimentally realized. This is particularly important when searching for new materials with specific properties and for investigating the behavior of the materials under extreme conditions which can't be obtained in the laboratory, such as the high temperature and pressure in the Earth's core.

(ii) The continuous progress in both basic theory and algorithms which increases the accuracy and efficiency of these methods and open the door for new applications.

(iii) The availability of a large variety of codes, which are rather easy to use and have many interesting and useful features.

(iv) The huge progress in the computer performance.

Providing a comprehensive account of these approaches and their developments and applications is far beyond the scope of any review article. Instead, this subject is introduced through a set of examples taken from my recent research work, which touch upon some important recent developments in this field, namely the exact-exchange formalism within KS-DFT, exact-exchange based quasi-particle GW calculations and maximally localized Wannier functions. This is in addition to the density functional perturbation theory. The basic theory behind these approaches is briefly described and some results are provided to demonstrate the accuracy and capabilities of these approaches. It should be noted that the presented results are obtained using programs to which we have added the new used features, namely the exact-exchange and maximally localized Wannier functions to the SPHINX code [102].

Acknowledgements

References

[1] Kohn, W. and Sham, L.J., Phys. Rev. A, 140 (1965) 1133.

[2] Hohenberg, P. and Kohn, W., Phys. Rev. B, 136 (1964) 864.

[3] Martin, R.M., Electronic Structure: Basic Theory and Practical Methods (Cambridge University Press, Cambridge, 2004).

[4] Perdew, J.P. and Zunger, A., Phys. Rev. B, 23 (1981) 5048.

[5] Godby, R.W., Schlüter, M. and Sham, L.J., Phys. Rev. B, 37 (1988) 10159.

[6] Kotliar, G. et al., Rev. Mod. Phys., 78 (2006) 865.

[7] Vogel, D., Krüger, P. and Pollmann, J., Phys. Rev. B, 54 (1996) 5495.

[8] Qteish, A., J. Phys.: Condens. Matter, 12 (2000) 5639.

[9] Langreth, D.C. and Mehl, M.J., Phys. Rev. B, 28 (1983) 1809.

[10] Städele, M., Majewski, J.A., Vogl, P. and Görling, A., Phys. Rev. Lett., 79 (1997) 2089.

[11]Städele, M., Moukara, M., Majewski, J.A., Vogl, P. and Görling, A., Phys. Rev. B, 59 (1999) 10031.

[12]Sahni, V., Gruenebaum, J. and Perdew, J.P., Phys. Rev. B, 26 (1982) 4371.

[13]Sharp, R.T. and Horton, G.K., Phys. Rev., 90 (1953) 317.

[14]Talman, J.D. and Shadwick, W.F., Phys. Rev. A, 14 (1976) 36.

[15]Qteish, A., Al-Sharif, A.I., Boeck, S., Neugebauer, J., Fuchs, M. and Scheffler, M., Phys. Rev. B, 72 (2005) 155317.

[16]Aulbur, W.G., Jönsson, L. and Wilkins, J.W., Solid State Phys., 54 (1999) 1.

[17]Rinke, P., Qteish, A., Nuegebauer, J., Froysoldt, C. and Scheffler, M., New Journal of Physics, 7 (2005) 126.

[18]Hedin, L., Phys. Rev., 139 (1965) A796.

[19]Hybertsen, M.S. and Louie, S.G., Phys. Rev. Lett., 55 (1985) 1418.

[20]Godby, R.W., Schlüter, M. and Sham, L.J., Phys. Rev. Lett., 56 (1986) 2415.

[21]Kotani, T. and van Schilfgaarde, M., Solid State Commun., 121 (2002) 476.

[22]Usuda, M., Hamada, N., Shiraishi, K. and Oshiyama, A., Jpn. J. Appl. Phys., 43 (2004) L407.

[23]Rohlfing, M., Krüger, P. and Pollmann, J., Phys. Rev. Lett., 75 (1995) 3489.

[24]Rohlfing, M., Krüger, P. and Pollmann, J., Phys. Rev. B, 57 (1998) 6485.

[25]Luo, W., Ismail-Beigi, S., Cohen, M.L. and Louie, S.G., Phys. Rev. B, 66 (2002) 195215.

[26]Qteish, A., Al-Sharif, A.I., Boeck, S., Neugebauer, J., Fuchs, M. and Scheffler, M., Computer Physics Comm., 169 (2005) 28.

[27]Rinke, P., Scheffler, M., Qteish, A., Winkelnkemper, M., Bimberg, D. and Nuegebauer, J., Appl. Phys. Lett., 89 (2006) 176919.

[28]Rinke, P., Winkelnkemper, M., Qteish, A., Bimberg, D., Nuegebauer, J., Scheffler, M., Phys. Rev. B, 77 (2008) 075202.

[29]Rinke, P., Qteish, A., Neugebauer, J., Freysoldt, C. and Scheffler, M., Phys. Stat. Sol. (b), 245 (2008) 929.

[30]Qteish, A., Rinke, P., Neugebauer, J. and Scheffler, M., Phys. Rev. B, 74 (2006) 245208.

[31]Qteish, A., Rinke, P., Neugebauer, J. and Scheffler, M., unpublished.

[32]Baroni, S., Giannozzi, P. and Testa, A., Phys. Rev. Lett., 59 (1987) 2662.

[33]Gonze, X., Allan, D.C. and Teter, M.P., Phys. Rev. Lett., 68 (1992) 3603.

[34]Gonze, X., Phys. Rev. B, 55 (1997) 10337.

[35]Gonze, X. and Lee, C., Phys. Rev. B, 55 (1997) 10355.

[36]Baroni, S., de Gironcoli, S., Dal Corso, A. and Giannozi, P., Rev. Mod. Phys., 73 (2001) 515.

[37]Hamann, D.R., Wu, X., Rabe, K.M. and Vanderbilt, D., Phys. Rev. B, 71 (2005) 035117.

[38]Wu, X., Vanderbilt, D., Hamann, D.R., Phys. Rev. B, 72 (2005) 035105.

[39]Aouissi, M., Hamdi, I., Meskini, N. and Qteish, A., Phys. Rev. B, 74 (2006) 054302.

[40]Hamdi, I., Aouissi, M., Qteish, A. and Meskini, N., Phys. Rev. B, 73 (2006) 174114.

[41]Tahri, S., Qteish, A., Al-Qasir, I. and Meskini, N., unpublished.

[42]Born, M. and Huang, K., Dynamical Theory of Crystal Lattices (Oxford University Press, New York, 1954).

[43]Carrier, P., Wentzcovitch, R. and Tsuchiya, J., Phys. Rev. B, 76 (2007) 064116.

[44]Wu, Z. and Wentzcovitch, R., Phys. Rev. B, 79 (2009) 104304.

[45]Grabowski, B., Ismer, L., Hickel, T. and Neugebauer, J., Phys. Rev. B, 79 (2009) 134106.

[46]Kunc, K. and Martin, R.M., in "*Ab initio* Calculations of Phonon Spectra", edited by J. T. Devreese, V. E. Van Doren and P. E. Van Camp (Plenum, New York, 1985), P. 65.

[47] Srivastava, G.P., Physics of Phonons (Taylor and Francis Group, New York, 1990).

[48] Fasolino, A., Molinari, E. and Kunc, K., Phys. Rev. B, 41 (1990) 8302.

[49] Qteish, A. and Molinari, E., Phys. Rev. B, 42 (1990) 7090.

[50] Ben Amar, A., Qteish, A. and Meskini, N., Phys. Rev. B, 53 (1996) 5372.

[51] Ben Amar, A., Qteish, A. and Meskini, N., Phys. Rev. B, 60 (1999) 6452.

[52] Wei, S. and Chou, M.Y., Phys. Rev. Lett., 69 (1992) 2799.

[53] Marzari, N. and Vanderbilt, D., Phys. Rev. B, 56 (1997) 12847.

[54] King-Smith, R.D. and Vanderbilt, D., Phys. Rev. B, 47 (1993) 1651.

[55] Vanderbilt, D. and King-Smith, R.D., Phys. Rev. B, 48 (1993) 4442.

[56] Resta, R., Rev. Mod. Phys., 66 (1994) 899.

[57] Williamson, A.J., Hood, R.Q. and Grossman, J.C., Phys. Rev. Lett., 87 (2001) 246406.

[58] Wu, X., Selloni, A. and Car, R., Phys. Rev. B, 79 (2009) 085102.

[59] Calzolari, A., Marzari, N., Souza, I. and Nardelli, M.B., Phys. Rev. B, 69 (2004) 035108.

[60] Usui, H., Arita, R. and Kurok, K., J. Phys.: Condens. Matter, 21 (2009) 064223.

[61] Ku, W., Rosner, H., Pickett, W.E. and Scalettar, R.T., Phys. Rev. Lett., 89 (2002) 167204.

[62] Schnell, I. and Kotliar, G., Phys. Rev. B, 65 (2002) 075103.

[63] Paul, I. and Kotliar, G., Phys. Rev. B, 67 (2003) 115131.

[64] Whittaker, D.M. and Croucher, M.P., Phys. Rev. B, 67 (2003) 085204.

[65] Silvestrelli, P.L., Phys. Rev. Lett., 180 (2008) 053002.

[66] Wahn, M. and Neugebauer, J., Phys. Stat. Sol. (b), 243 (2006) 1583.

[67] Abu-Farsakh, H. and Qteish, A., Phys. Rev. B, 75 (2007) 085201.

[68] Payne, M.C., Teter, M.P., Allan, D.C., Arias, T.A. and Joannopoulos, J.D., Rev. Mod. Phys., 64 (1992) 1045.

[69] Fock, V., Z. Phys., 63 (1930) 855.

[70] Jones, R.O. and Gunnarsson, O., Rev. Mod. Phys., 76 (1989) 681.

[71] Staroverov, V.N., Scuseria, G.E., Tao, J. and Perdew, J.P., Phys. Rev. B, 69 (2004) 075102.

[72] Däne, M. et al., J. Phys.: Condens. Matter, 21 (2009) 045604, and references therein.

[73] Filippetti, A. and Spaldin, N.A., Phys. Rev. B, 67 (2003) 125109.

[74] Droghetti, A., Pemmaraju, C.D. and Sanvito, S., Phys. Rev. B, 78 (2008) 140404(R).

[75] Anisimov, V.I., Aryasetiawan, F. and Lichtenstein, A.I., J. Phys.: Condens. Matter, 9 (1997) 767.

[76] Becke, A.D., J. Chem. Phys., 98 (1993) 1372.

[77] Casida, M.E., Phys. Rev. A, 51 (1995) 2005.

[78] Kümmel, S. and Perdew, J.P., Phys. Rev. B, 68 (2003) 035103.

[79] Gross, E., Runge, E. and Heinonen, O., Many-Particle Theory (Hilger, Bristol, 1991).

[80] Landau, L.D., Sov. Phys.—JETP, 3 (1957) 920; Sov. Phys.—JETP, 5 (1957) 101; Sov. Phys.— JETP, 35 (1959) 70.

[81] Magyar, R.J., Fleszar, A. and Gross, E.K.U., Phys. Rev. B, 69 (2004) 045111.

[82] Wu, J. et al., Appl. Phys. Lett., 80 (2002) 3967.

[83] Davydov, V.Y. et al., Phys. Status Solidi B, 229 (2002) R1.

[84] Nanishi, Y., Saito, Y. and Yamaguchi, T., Jpn. J. Appl. Phys., 42 (2003) 2549.

[85] Wu, J. et al., Phys. Rev. B, 66 (2002) 201403.

[86] Walukiewicz, W. et al., J. Cryst. Growth, 269 (2004) 119.

[87]The ABINIT code is a common project of the Université Catholique de Louvin, Corning Incorporated, and other contributors, URL http://www.abinit.org.

[88]The knowledge of $\{\varphi^{(n)}\}$ allows the calculation of the total energy derivatives up to the $(2n+1)$ order.

[89]Sternheimer, R.M., Phys. Rev., 96 (1954) 951.

[90]Hennion, H., Moussa, F., Pepy, G. and Kunc, K., Phys. Lett. A, 35 (1971) 376.

[91]Louie, S.G., Froyen, S. and Cohen, M.L., Phys. Rev. B, 26 (1982) 1738.

[92]Callen, H.B., Thermodynamics and an Introduction to Thermostatistics (Wiley, New York, 1985).

[93]Karch, K., Pavone, P., Windl, W., Schütt, O. and Strauch, D., Phys. Rev. B, 50 (1994) 17054.

[94]Smith, T.F. and White, G.K., J. Phys. C, 8 (1975) 2031.

[95]Novikova, S.I., Fiz. Tverd. Tela (Leningrad) 2 (1960) 2341. [Sov. Phys. Solid State, 2 (1976) 2087]; 3 (1976) 178 [3 (1976) 129]; 5 (1963) 2138 [5 (1964) 1558]; 1 (1959) 1841 [1 (1960) 1687].

[96]Irwin, J.C. and LaCombe, J., J. Appl. Phys., 45 (1974) 567.

[97]Birch, J.A., J. Phys. C, 8 (1975) 2043.

[98]Phillips, J.C., Bonds and Bands in Semiconductors (Academic Press, New York, 1973).

[99]Garcia, A. and Cohen, M.L., Phys. Rev. B, 47 (1993) 4215.

[100]Christensen, N.E., Satpathy, S. and Pawlowska, Z., Phys. Rev. B, 36 (1987) 1032.

[101]Phillips, J.C., Rev. Mod. Phys., 42 (1970) 317.

[102]www.sphinxlib.de.

Jordan Journal of Physics

ARTICLE

Design Principles for Quarter-Wave Retarders that Employ Total Internal Reflection and Light Interference in a Single-Layer Coating

R. M. A. Azzam and **H. K. Khanfar**

Department of Electrical Engineering, University of New Orleans, New Orleans, Louisiana 70148, USA.

Abstract: Explicit equations are derived for the design of quarter-wave retarders (QWR) that exploit total internal reflection (TIR) and interference of light in a transparent thin-film coating at the base of a prism. The optimal refractive index and normalized thickness of QWR coatings on glass and ZnS prisms are determined as functions of the internal angle of incidence from 45° to 75°. An achromatic retarder that uses TIR by a Si_3N_4-coated N-BK10-Schott glass prism is also presented that achieves exact QWR at two wavelengths (409 and 500 nm) and exhibits a retardation error of $< 1.5^o$ for wavelengths $375 \leq \lambda \leq 550$ nm in the near-UV and the violet-blue-green part of the visible spectrum.

Keywords: Polarization; Interference; Total internal reflection; Thin films; Wave retarders; Physical optics.

Introduction

Quarter-wave retarders (QWR) are versatile optical elements that are widely used for polarization-state generation and detection [1, 2]. The 90° differential phase shift (or an odd multiple thereof) between the two orthogonal linear eigenpolarizations of a QWR is often obtained in transmission through a linearly birefringent crystalline plate or by employing total internal reflection (TIR) in a prism. QWR prisms of different designs that employ one or multiple TIR have been described [3 - 9].

To obtain QWR on single TIR at a dielectric-dielectric interface requires a refractive index ratio of $\geq \sqrt{2}+1 = 2.414$ [10]. For example, Ref. [11] describes a non-interference-type, broadband (1.2 – 4 μm), IR QWR that uses one TIR at a buried Si-SiO_2 interface. However, the presence of an optical interference coating (at the prism-air interface) significantly alters the phase shifts that accompany TIR, hence introduces flexibility that can be exploited in the design

of QWR [12, 13]. The primary aim of this work is to present a new analytical approach for the design of such single-layer-coated TIR QWR and to provide several examples on its applications.

Analysis and Design Procedure

Fig. 1 shows TIR of a monochromatic light beam of wavelength λ at an angle of incidence ϕ at the base of a prism of refractive index n_0 which is coated with a transparent thin film of refractive index n_1 and thickness d. (Notice that the thickness d is greatly exaggerated on the scale of Fig. 1, and that the overlapping partial beams that are reflected from the front and back sides of the optically thin film are not shown.) The surrounding ambient medium is assumed to be air or an inert gas of refractive index $n_2 = 1$ and the entrance and exit faces of the prism are antireflection coated (ARC). The complex-amplitude reflection coefficients of

Corresponding Author: R. M. A. Azzam. **Email**: razzam@uno.edu

the coated surface for the incident linear polarizations parallel p and perpendicular s to the plane of incidence, that account for light interference in the thin film, are given by the Airy-Drude formula [2]:

$$R_\nu = \frac{r_{01\nu} + r_{12\nu}X}{1 + r_{01\nu}r_{12\nu}X}, \nu = p, s. \qquad (1)$$

In Eq. (1) $r_{01\nu}, r_{12\nu}$ are the Fresnel reflection coefficients at the prism-film (01) and film-ambient (12) interfaces for the ν polarization, respectively, and

$$\left.\begin{array}{l} X = \exp(-i\,2\pi\varsigma), \\ \varsigma = d/D_\phi, \\ D_\phi = (\lambda/2)(n_1^2 - n_0^2 \sin^2\phi)^{-1/2}. \end{array}\right\} \qquad (2)$$

TIR at the base of the prism requires that $\phi > \phi_{c02} = \arcsin(1/n_0); \phi_{c02}$ is the critical angle of the film-free prism-air (02) interface. To ensure partial reflection at the prism-film (01) interface, hence allow for light interference in the coating, we choose $n_1 > n_0$. Under these conditions, the overall reflection coefficients R_ν [Eq. (1)] are periodic functions of film thickness d with period D_ϕ given by Eq. (2).

The Fresnel interface reflection coefficients $r_{01\nu}, r_{12\nu}$ for the ν polarization can be conveniently expressed in terms of two angles α_ν, δ_ν,

$$\left.\begin{array}{l} r_{01\nu} = \tan\alpha_\nu, \\ r_{12\nu} = \exp(i\,\delta_\nu), \\ \nu = p, s. \end{array}\right\} \qquad (3)$$

In the Nebraska-Muller conventions [2, 14] α_ν, δ_ν are restricted to the following ranges,

$$\left.\begin{array}{l} -45^\circ \le \alpha_p \le 45^\circ, -45^\circ \le \alpha_s \le 0, \\ 0 \le \delta_{p,s} \le \pi. \end{array}\right\} \qquad (4)$$

By substitution of Eqs. (2) and (3) in Eq. (1), we obtain

$$\left.\begin{array}{l} R_\nu = \frac{\tan\alpha_\nu + \exp(-i\,\gamma_\nu)}{1 + \tan\alpha_\nu \exp(-i\,\gamma_\nu)}, \\ \gamma_\nu = 2\pi\varsigma - \delta_\nu, \\ \nu = p, s. \end{array}\right\} \qquad (5)$$
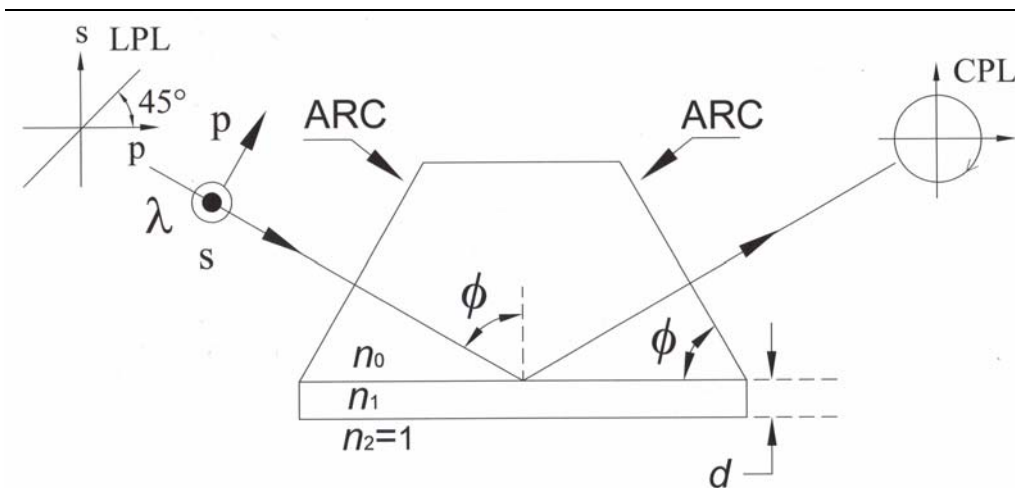

FIG. 1. TIR of a monochromatic light beam of wavelength λ at an angle of incidence ϕ at the base of a prism of refractive index n_0 which is coated with a transparent thin film of refractive index n_1 and thickness d. The entrance and exit faces of the prism are antireflection coated (ARC). p and s represent the orthogonal linear polarizations parallel and perpendicular to the plane of incidence, respectively. When QWR is achieved, incident linearly polarized light (LPL) at 45° azimuth from the plane of incidence is reflected as circularly polarized light (CPL).

From Eq. (5), it can be readily verified that $R_\nu R_\nu^* = 1$, which confirms that TIR takes place at the coated base of the prism. Consequently, R_ν is expressed as a pure phase factor

$$R_\nu = \exp(i\Delta_\nu), \nu = p, s, \qquad (6)$$

where Δ_ν is the overall TIR phase shift for the ν polarization. From Eqs. (5) and (6), the following important result is obtained:

$$\tan\Delta_\nu = \frac{-\cos(2\alpha_\nu)\sin\gamma_\nu}{\sin(2\alpha_\nu)+\cos\gamma_\nu}, \nu = p, s. \qquad (7)$$

The differential retardation on TIR is specified by the difference

$$\Delta = \Delta_p - \Delta_s. \qquad (8)$$

Taking the tangent of both sides of Eq. (8) gives

$$\tan\Delta = \frac{\tan\Delta_p - \tan\Delta_s}{1 + \tan\Delta_p \tan\Delta_s}. \qquad (9)$$

To achieve QWR on TIR at the coated base of the prism, $\Delta = \pm\pi/2$, the denominator of the right-hand side of Eq. (9) must be zero, or

$$\tan\Delta_p \tan\Delta_s = -1. \qquad (10)$$

Substitution of Eq. (7) in Eq. (10) gives

$$\left.\begin{array}{l} \cos\gamma_p \cos\gamma_s + \sin(2\alpha_p)\cos\gamma_s + \\ \sin(2\alpha_s)\cos\gamma_p + \\ \cos(2\alpha_p)\cos(2\alpha_s)\sin\gamma_p \sin\gamma_s \\ + \sin(2\alpha_p)\sin(2\alpha_s) = 0. \end{array}\right\} \qquad (11)$$

Equation (11) is the essential design condition for achieving QWR using TIR by a single-layer-coated prism (Fig. 1). The angles $\alpha_p, \alpha_s, \gamma_p, \gamma_s$ that appear in Eq. (11) are expressed as explicit functions of the prism and film refractive indices n_0, n_1, angle of incidence ϕ and normalized film thickness ς by

$$\left.\begin{array}{l} \alpha_p = (\pi/4) - \\ \quad \arctan[n_0(n_1^2 - n_0^2 \sin^2\phi)^{1/2} / \\ \quad\quad (n_1^2 \cos\phi)], \\ \alpha_s = (\pi/4) - \\ \quad \arctan[(n_1^2 - n_0^2 \sin^2\phi)^{1/2} / \\ \quad\quad (n_0 \cos\phi)]; \end{array}\right\} \qquad (12)$$

$$\left.\begin{array}{l} \gamma_p = 2\pi\varsigma - \\ \quad 2\arctan[n_1^2(n_0^2 \sin^2\phi - 1)^{1/2} / \\ \quad\quad (n_1^2 - n_0^2 \sin^2\phi)^{1/2}], \\ \gamma_s = 2\pi\varsigma - \\ \quad 2\arctan[(n_0^2 \sin^2\phi - 1)^{1/2} / \\ \quad\quad (n_1^2 - n_0^2 \sin^2\phi)^{1/2}]. \end{array}\right\} \qquad (13)$$

For a given prism with refractive index n_0 and angle of incidence ϕ, Eq. (11) can be cast in the simple functional form

$$f(n_1, \varsigma) = 0. \qquad (14)$$

Eq. (14) represents the constraint on the refractive index n_1 and normalized thickness ς of the interference coating such that QWR is realized in TIR. As will be seen in the next section, Eq. (14) has infinitely many solutions, but only one is optimal in that QWR is achieved with minimum sensitivity to small changes of film thickness or wavelength.

Total Internal Reflection QWR Using Coated Glass Prism

Consider a prism of refractive index $n_0 = 1.5$ (e.g. glass) and an angle of incidence $\phi = 60°$. Fig. 2 shows a plot of the function $f(n_1, \varsigma)$ versus ς, $0 \le \varsigma \le 1$, for constant values of film refractive index n_1 from 1.9 to 6.1 in equal steps of 0.2 that represent numerous transparent optical coating materials in the visible and IR light. For each n_1 in this range, Eq. (14) has two solutions for ς (represented by points A and B for the case of $n_1 = 1.9$). The minimum value of n_1 for which the two solutions of Eq.

159

(14) coincide is $n_{1\min} = 1.7924$, and no solutions exist if $n_1 < n_{1\min}$. This corresponds to the point of tangency C ($\varsigma_C = 0.355$) of the topmost curve in Fig. 2 and the dashed line $f = 0$. Point C represents the optimal choice of film refractive index and thickness as it indicates insensitivity to small changes of ς, hence tolerance to small film-thickness errors or wavelength shifts. Suitable optical coating materials whose refractive index can be tuned to the optimal value $n_{1\min} = 1.7924$

(e.g. by appropriate control of stoichiometry and deposition conditions) include SiON [15] and Y_2O_3 [16].

Fig. 3 represents the locus of all possible solutions of Eq. (14) for coatings on a prism with refractive index $n_0 = 1.5$ that achieve QWR on TIR at an internal angle of incidence $\phi = 60°$. Again, the optimal coating refractive index and thickness correspond to point C at the bottom of the curve.
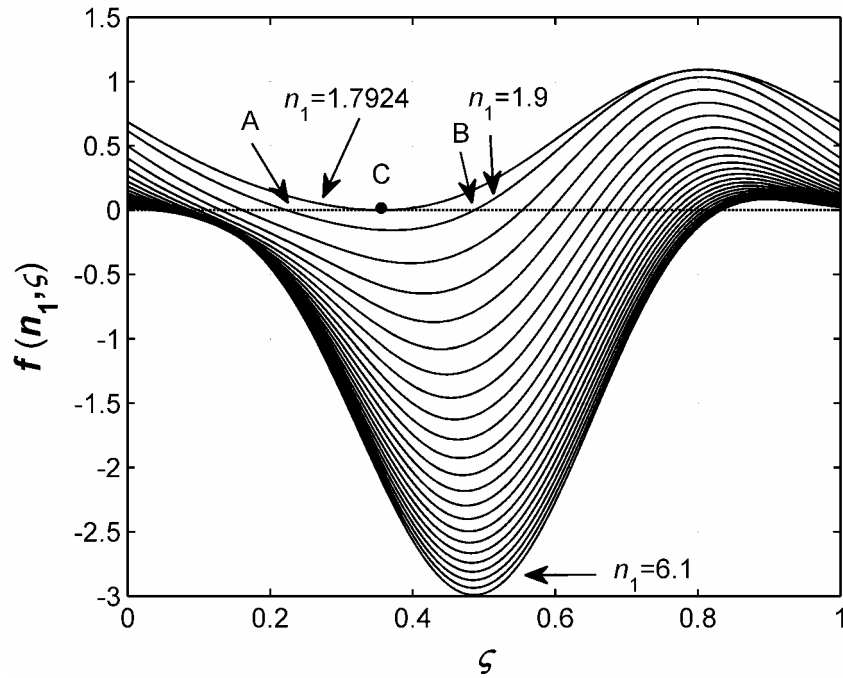

FIG. 2. Plot of the function $f(n_1, \varsigma)$ versus ς for constant values of n_1 from 1.9 to 6.1 in uniform steps of 0.2 for $n_0 = 1.5$ and $\phi = 60°$. For each n_1 in this range, Eq. (14) has two solutions for ς (represented by points A and B on the curve for $n_1 = 1.9$). The minimum value of n_1 for which the two solutions of Eq. (14) coincide is $n_{1\min} = 1.7924$ and corresponds to the point of tangency C of the topmost curve with the $f = 0$ line.

Fig. 4 shows the optimal refractive index $n_{1\min}$ and associated normalized thickness ς of thin-film coatings on a prism with $n_0 = 1.5$ that achieve QWR on TIR at different angles of incidence in the range $45° \leq \phi \leq 75°$.

Figure 5 shows the corresponding results for optimal QWR coatings on Cleartran ZnS [17] prism with refractive index $n_0 = 2.35$ for red light ($\lambda \approx 633$ nm).
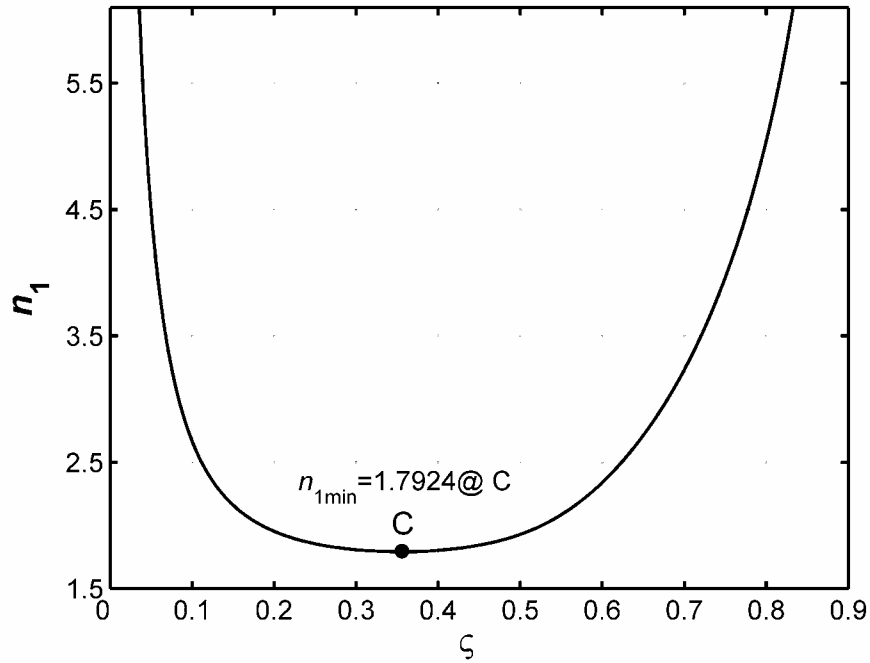
FIG. 3. Locus of all possible solutions of Eq. (14) is shown for coatings on prism of refractive index $n_0 = 1.5$ (e.g. glass) that achieve QWR on TIR at an angle of incidence $\phi = 60^\circ$. The optimal coating is represented by point C.
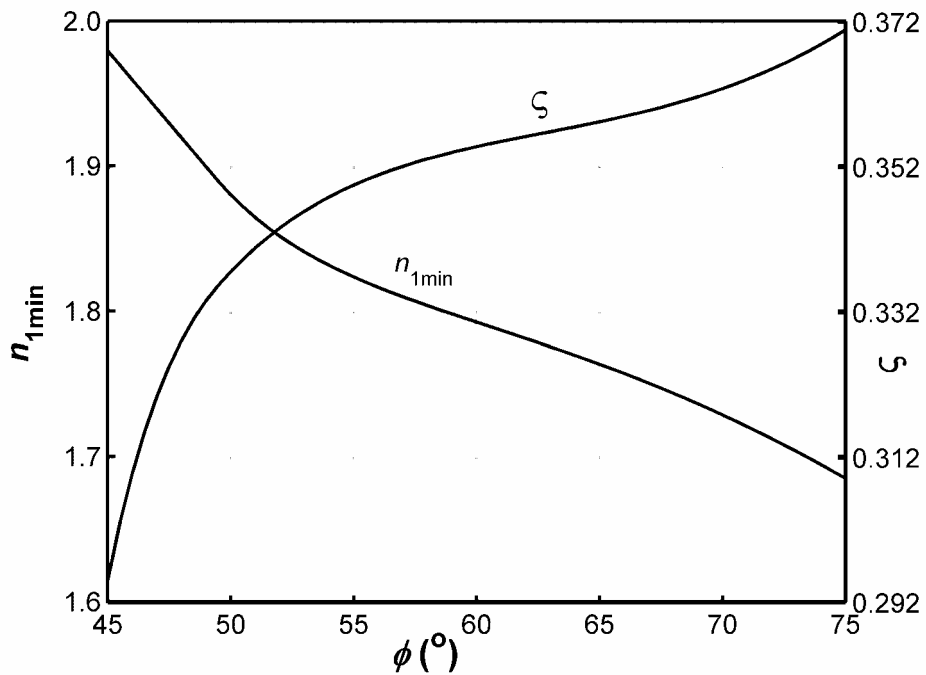

FIG. 4. Optimal (minimum) refractive index $n_{1\min}$ and associated normalized thickness ς of thin-film coatings on a prism of refractive index $n_0 = 1.5$ that achieve QWR on TIR at angles of incidence ϕ that vary from 45° to 75°.
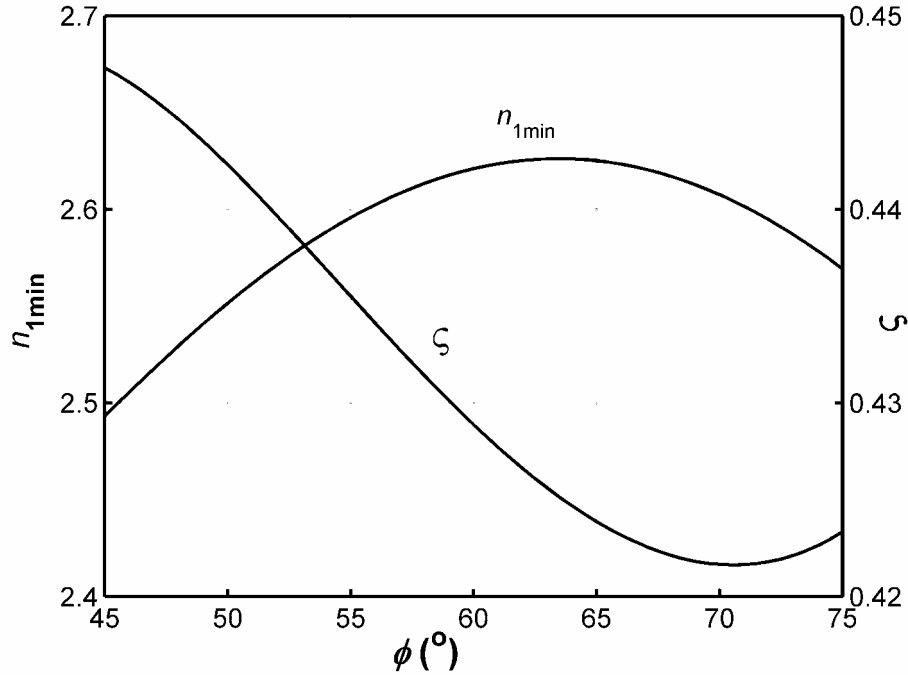
FIG. 5. Optimal (minimum) refractive index $n_{1\min}$ and associated normalized thickness ς of thin-film coatings on ZnS prism ($n_0 = 2.35$) that achieve QWR on TIR at angles of incidence ϕ that vary from $45°$ to $75°$.

Spectral Response of TIR QWR that Uses Right-Angle Prism of N-BK10 Glass Coated with Si_3N_4 Film

We now consider a specific TIR QWR made of a right-angle prism ($\phi = 45°$) of N-BK10 Schott glass with $n_0 = 1.5021$ [18] at the preselected design wavelength $\lambda = 500$ nm. The calculated optimal coating refractive index $n_{1\min} = 2.0607$ matches that of silicon nitride [15] at $\lambda = 500$ nm, and the associated optimum film thickness is $d = 43.66$ nm.

Figure 6 shows the retardation Δ *versus* λ of this QWR for $375 \leq \lambda \leq 550$ nm, which includes near-UV and the violet-blue-green part of the visible spectrum. In these calculations, the dispersion of the coating and prism materials is accounted for [15, 18]. Notice that exact QWR ($\Delta = 90°$) is achieved at the design wavelength $\lambda = 500$ nm (point P), as expected, and also at the shorter wavelength $\lambda = 409$ nm (point Q). The deviation of Δ from $90°$ is $< 1.5°$ over the $375 \leq \lambda \leq 550$ nm spectral range and is

$< 0.55°$ over the 400-500 nm band. This retardation error is less than that of commercial achromatic crystal wave plates over comparable bandwidths [19].

Conclusions

We provided detailed explicit analysis of the conditions that are required to achieve QWR ($90°$ differential phase shift between the *p* and *s* linear polarizations) on total internal reflection (TIR) at the base of a prism which is coated with a single-layer optical interference film. For given prism refractive index and angle of incidence, optimal values of the refractive index and thickness of the thin-film coating for QWR are obtained. Specific results are shown over a range of incidence angles for TIR QWR using transparent coatings on glass and ZnS substrates. A TIR retarder that employs Si_3N_4-coated N-BK10-Schott glass prism is also presented that exhibits exact QWR at two wavelengths (409 and 500 nm) and has a retardation error of $< 1.5°$ over the 375 - 550 nm spectral range.
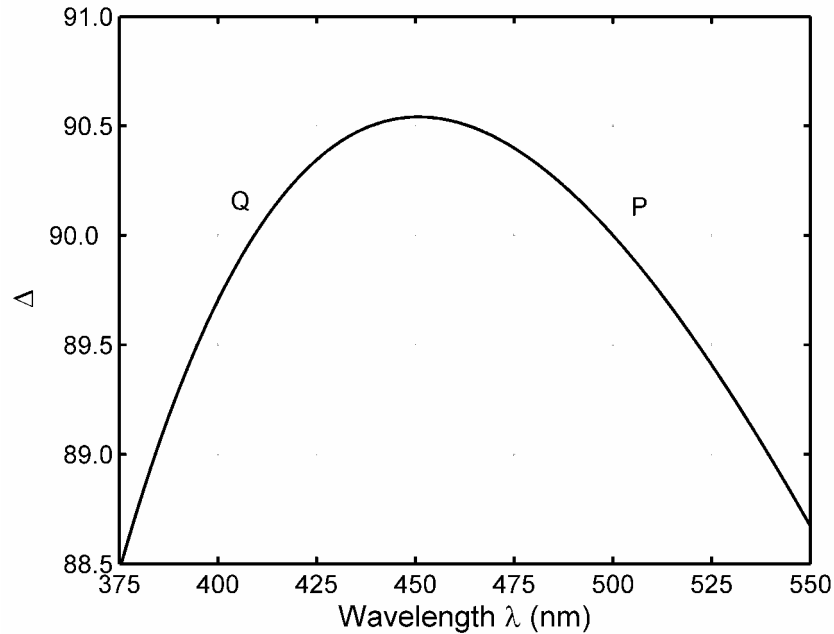
FIG. 6. Spectral response (Δ versus λ) of TIR QWR made of right-angle prism ($\phi = 45^\circ$) of N-BK10 Schott glass with refractive index $n_0 = 1.5021$ at $\lambda = 500$ nm whose base is coated with a silicon-nitride layer of refractive index $n_1 = 2.0607$ ($\lambda = 500$ nm) and thickness $d = 43.66$ nm. QWR is exactly achieved at two wavelengths $\lambda = 500$ and 409 nm at points P and Q, respectively.

References

[1]Bennett, J.M., "Polarization", in: M. Bass (ed.), Handbook of Optics, Vol. I (McGraw-Hill, New York, 1995), Chap. 5.

[2]Azzam, R.M.A. and Bashara, N.M., "Ellipsometry and Polarized Light" (North-Holland, Amsterdam, 1987).

[3]King, R.J., J. Sci. Instrum., 43 (1966) 617.

[4]Bennett, J.M., Appl. Opt., 9 (1970) 2123.

[5]Filinski, I. and Skettrup, T., Appl. Opt., 23 (1984) 2747.

[6]Kan'an, A. M. and Azzam, R. M. A., Opt. Eng., 33 (1994) 2029.

[7]Azzam, R.M.A. and Howlader, M.M.K., J. Lightwave Technol., 14 (1996) 873.

[8]Azzam, R.M.A. and Khanfar, H.K., Appl. Opt., 47 (2008) 359.

[9]Azzam, R.M.A. and Khanfar, H.K., Appl. Opt., 47 (2008) 4878.

[10]Azzam, R.M.A., J. Opt. Soc. Am., A, 21 (2004) 1559.

[11]Azzam, R.M.A. and Spinu, C.L., J. Opt. Soc. Am., A, 21 (2004) 2019.

[12]Spiller, E., Appl. Opt., 23 (1984) 3544.

[13]Cojocaru, E., Appl. Opt., 28 (1989) 211.

[14]Muller, R.H., Surf. Sci., 16 (1969) 14.

[15]Bååk, T., Appl. Opt., 21 (1982) 1069.

[16]www.cerac.com/pubs/proddata/y2o3.htm.

[17]Debenham, M., Appl. Opt., 23 (1984) 2238.

[18]www.us.schott.com/optics_devices/english/ products/flash/abbediagramm_flash.html.

[19]www.edmundoptics.com.

Jordan Journal of Physics

ARTICLE

Effect of Sintering and Annealing Temperatures on the Critical Temperature and Electrical Resistivity of $Bi_2Ba_2Ca_2Cu_3O_{10+\delta}$

Y. A. Hamam[a], **A. El Ali (Al-Dairy)**[a], **K. D. Alazawi**[b] and **S. M. Mamand**[c]

[a] *Department of Physics, Yarmouk University, Irbid, Jordan.*

[b] *Department of Physics, University of Mousl, Mousl, Iraq.*

[c] *College of Teachers, Sulaimania University, Iraq.*

Abstract: Samples of the high temperature superconducting system, $Bi_2Ba_2Ca_2Cu_3O_{10+\delta}$, were prepared by using the solid state reaction method with different sintering temperatures of 810, 830, 850, 870 and 890 $^{\circ}$C. The electrical resistivity measurements exhibited that the sintering and annealing conditions have major effects on the critical temperature of the superconducting compound. The sample prepared at 850 $^{\circ}$C has a critical temperature $T_c \approx$ 110 K, meanwhile the sample prepared at 870 $^{\circ}$C has a critical temperature $\approx$ 80 K. However, the sample which was prepared at 890 $^{\circ}$C showed semiconducting behavior with an activation energy of 6.40 meV. The effect of annealing on the critical temperature has been investigated using the sample prepared at 850 $^{\circ}$C. The value of T_c at the annealing temperature of 400 $^{\circ}$C rises from 110 K to 138 K with increasing the annealing time from 24 hrs to 72 hrs. This increase might be due to the increase of oxygen content or to the intergrowth of a large number of Cu-O layers in the cell.

Keywords: High temperature superconductors; Semiconductors; Sintering; Annealing; Electrical resistivity.

Introduction

The discovery of superconductivity between 7 K and 22 K in the Bi-Sr-Cu-O compound has been reported by Michel *et al.* in 1987 [1]. Meada *et al.* [2] and Chu *et al.* [3] reported that adding Ca to the Bi-Sr-Cu-O system produced a material that was superconducting above liquid nitrogen temperature 77 K.

Great attention has been focused on the series compound Bi-Sr-Cu-O which shows superconductivity around 105 K [4]. The properties of these systems show that the superconductors with structure formulae $Bi_2Sr_2CuO_6$, $Bi_2Sr_2CaCu_2O_8$ and $Bi_2Sr_2Ca_2Cu_3O_{10}$ have T_c values of 10, 85 and 110 K, respectively [5].

The partial substitution effects on the structure and electrical properties of the high temperature superconducting compounds $Bi_{2-x}Tl_xBa_{2-y}Sr_yCa_2Cu_3O_{10+\delta}$ have been investigated [6]. Makarenko *et al.* studied the annealing effect on critical temperature and resistivity of $(Bi,Pb)_2Sr_2Ca_2Cu_3O_y$ after being irradiated by Co-60 gamma-rays. They found that annealing at 150-200 $^{\circ}$C resulted in an increase of resistivity and a drop of critical temperature up to doses of 2×10^9 R [7]. The effect of post-annealing on critical current density of (Bi,Pb)-2223/Ag tapes has been reported by Li *et al.* Their results showed that post-annealing at low temperature in reduced oxygen partial pressure can improve the critical current density. They claimed that the effect of post-annealing could be related to the increase of (Bi,Pb)-2223 phase and the formation of $Pb_3Sr_{2.5}Bi_{0.5}Ca_2CuO_y$ (3321 phase) as well as the improvement of grain connectivity [8]. Khalil and Sedky studied the

---

Corresponding Author: Y. A. Hamam. **Email**: yaqobhamam@yahoo.com

effect of annealing temperature (750-850 °C), when annealing in air for 50 hrs, on the structural, mechanical and superconducting properties of $Bi_2Sr_2CaCu_2O_{8+\delta}$ system [9]. They found that the critical temperature T_c increased from 78 up to 100 K with annealing temperature in addition to more sharpening of the transition. This behavior was explained by the improvement of coupling between superconducting grains and by elimination, by annealing, of oxygen disorder and microcracks. Florence *et al.* investigated the effects of rapid thermal annealing on the material and electrical properties of sputter deposited $YBa_2Cu_3O_{7-x}$ superconducting films [10]. They found that the critical temperature decreased for all annealing times and temperatures above the growth temperature and suggested that this was due to oxygen effusion from thin films.

The aim of this paper is to investigate mainly the electrical properties of the superconductor compound Bi-Ba-Ca-Cu-O using different sintering and annealing temperatures as well as different annealing times.

Experimental Procedure

High temperature $Bi_2Ba_2Ca_2Cu_3O_{10+\delta}$ superconductor samples were prepared using the solid state reaction method using appropriate quantities of highly pure Bi_2O_3, $CaCO_3$, $BaCO_3$ and CuO. The mixture was ground with isopropanol by using a gate mortar. The well mixed powder of these oxides was calcimined at 800 °C.

The mixture was pressed into approximately 1 gm pellets, 1.1 cm in diameter and 0.17 cm in thickness. The pressed pellets were initially heated in air from room temperature to different sintering temperatures of 810, 830, 850, 870 and 890 °C for 24 hrs and then slowly cooled to room temperature at a rate of 30 °C/hr. Finally, the sample pellets were annealed at different temperatures of 200, 400, 500, 600 and 700 °C for different annealing times of 24, 48, 72 and 96 hrs.

The X-ray diffraction patterns at room temperature were obtained using Phillips X-ray diffractometer with CuK_α radiation ($\lambda = 1.5418$ Å).

The electrical resistivity was measured using the standard four-probe method and the electrical contacts to the samples were made using fine copper wires with conductive silver paste. The electrical resistivity measurements have been conducted to determine the critical temperature. The oxygen content in the sample was measured by using the iodemetric method [11].

Results and Discussion

X-ray diffraction measurements on $Bi_2Ba_2Ca_2Cu_3O_{10+\delta}$ superconductor sintered at 850 °C were reported in a previous article [6]. The structure was found to be single tetragonal phase with lattice parameters $a = b = 5.43$ Å and $c = 34.13$ Å. The electrical resistivity at various sintering temperatures was obtained and the results are shown in Fig. 1. The critical temperatures and oxygen contents at various sintering temperatures are summarized in Table 1.

As shown in Table 1, the increase of sintering temperature from 810 °C to 870 °C leads to an increase in oxygen content. The critical temperature T_c has an optimum value with increasing sintering temperature (T_c has a maximum value when samples are sintered at 850 °C). The superconducting critical transition temperature, T_c in this work, is defined as the temperature at which the sample resistance drops to zero.

TABLE 1. Critical temperatures for $Bi_2Ba_2Ca_2Cu_3O_{10+\delta}$ samples with different sintering temperatures.

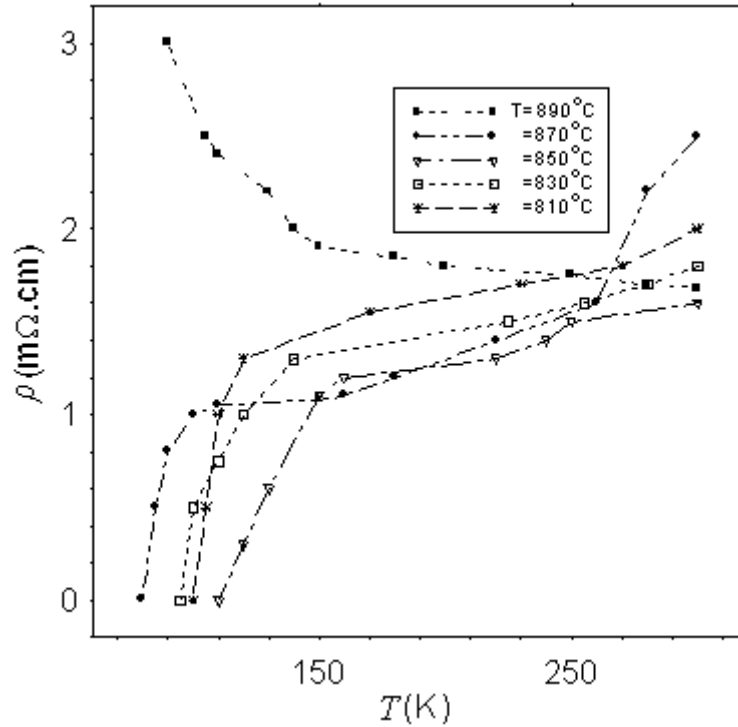| T (°C)	T_c (K)	$10+\delta$
810	99	10.12
830	95	10.17
850	110	10.22
870	80	10.71
890	Semiconductor: $E_{act} = 6.35$ meV	10.27

FIG. 1. The resistivity versus temperature for Bi$_2$Ba$_2$Ca$_2$Cu$_3$O$_{10+\delta}$ samples prepared at different sintering temperatures.

However, the additional increase in sintering temperature up to 890 °C leads to a drop in the oxygen content and might lead to a structural phase change. Optimal oxygen content is very necessary for the presence of high temperature superconductivity with tetragonal phase, and a shift from this optimal value would result in the formation of a non superconducting phase. The sample sintered at 890 °C showed semiconductor behavior. It is seen from Fig. 1 that the resistivity $\rho(T)$ of that sample rises exponentially with decreasing temperature. Therefore, the conductivity $\sigma(T) = 1/\rho(T)$ of the sample, at this sintering temperature, falls exponentially with increasing temperature. In Fig. 2, $\ln\sigma$ is plotted *versus* $1/T$ and the

conductivity is fitted to the expression (Arrhenius Equation):

$$\sigma(T) = \sigma_o \exp(-E_{act}/kT),$$

where $\sigma(T)$ is the conductivity at temperature T in Kelvin, $\sigma_o = \sigma(1/T = 0)$, E_{act} is the activation energy and k is the Boltzmann constant. This fit gave an activation energy of ≈ 6.35 meV and $\sigma_o = 0.764\,(m\Omega.cm)^{-1}$.

The conduction is due to hopping between conduction and valence bands; however electrons in this case are hopping between localized states. The change in the superconducting behavior at different sintering temperatures is probably due to the change in grain connectivity or coupling between the superconducting grains. These results are in good agreement with the results reported in other works [9, 10].
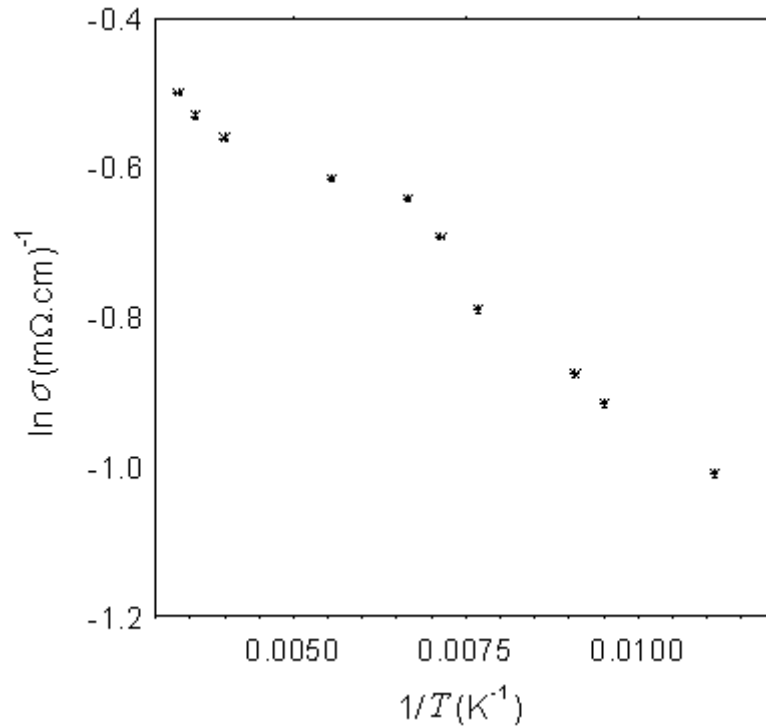
FIG. 2. The natural logarithm of the conductivity, ln σ, versus temperature for the $Bi_2Ba_2Ca_2Cu_3O_{10+\delta}$ sample sintered at 890 °C.

The maximum value of T_c is 110 K for samples prepared at a sintering temperature of 850 °C. These samples, sintered at 850 °C, were then annealed at different annealing temperatures and times. The best value of T_c was obtained for an annealing temperature of 400 °C. As shown in Fig. 3, it increased from 110 K to 130 K and then decreased with increasing annealing temperature. The behaviors of the critical temperature, T_c, and oxygen content with annealing temperature are summarized in Table 2. It is clear from that table that the increase in oxygen content plays a very important role in increasing or decreasing T_c. This could be caused by decreasing the structure defects and also due to the intergrowth of a large number of Cu-O layers in the unit cell.
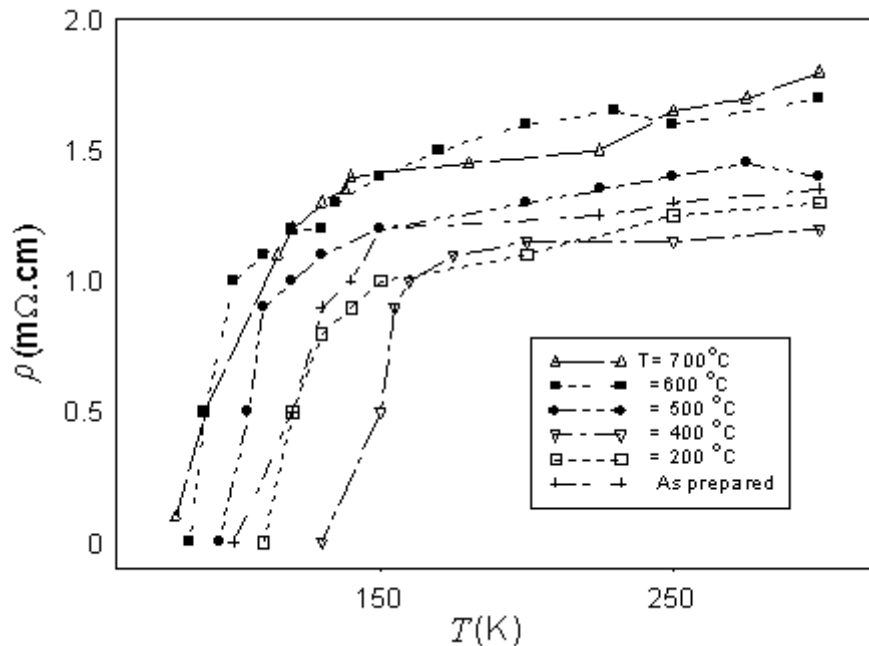

FIG. 3. The resistivity versus temperature for the prepared $Bi_2Ba_2Ca_2Cu_3O_{10+\delta}$ with different annealing temperatures.

168

TABLE 2. Critical temperatures for $Bi_2Ba_2Ca_2Cu_3O_{10+\delta}$ samples sintered at 850 °C with different annealing temperatures.

Annealing Temperature T (°C)	Critical Temperature T_c (K)	$10+\delta$
200	110	10.29
400	130	10.38
500	95	9.97
600	86	9.93
700	80	9.90

The behavior of resistivity *versus* temperature for an optimum annealing temperature of 400 °C with time is shown in Fig. 4. It is clear from this figure that increasing the time of annealing results in an increase in the value of T_c which saturates at the annealing time of 72 hours with a value of $T_c \approx 138$ K.

TABLE 3. Critical temperatures for annealed $Bi_2Ba_2Ca_2Cu_3O_{10+\delta}$ superconductors at 850 °C and different annealing times for the annealing temperature of (400 °C).

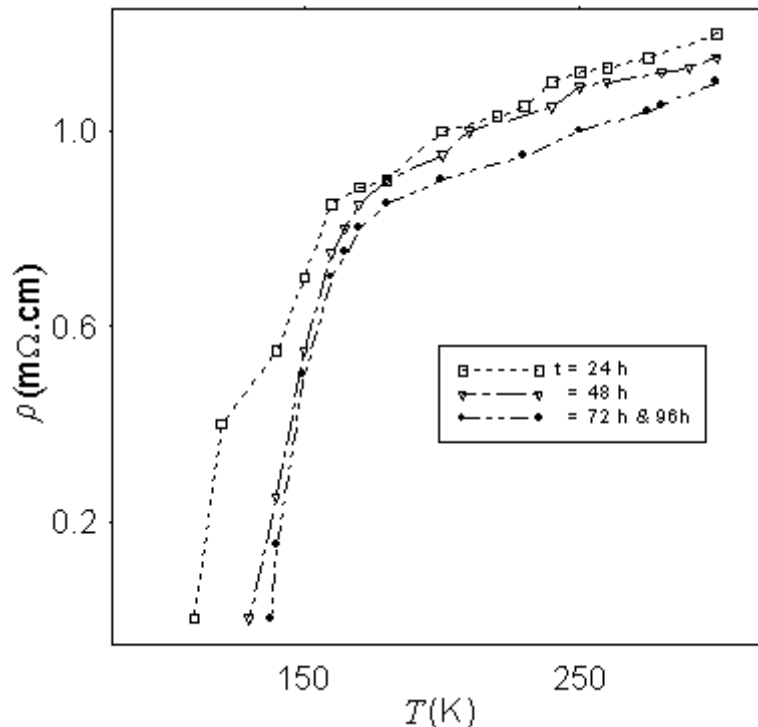| T_c (K)	Annealing time (hr)	$10+\delta$
110	24	10.38
130	48	10.40
138	72	10.42
138	96	10.42

FIG. 4. The resistivity versus temperature for $Bi_2Ba_2Ca_2Cu_3O_{10+\delta}$ samples annealed at 400 °C for different annealing times.

As shown in Table 3, and from Fig. 4, the increase in T_c value with increasing of annealing temperature leads to the increase in oxygen content. This might increase the charge carriers, the number of the Cooper pairs, due to more electron-phonon coupling conditions [5].

Conclusion

Superconductivity is possible in the tetragonal structure and orthorhombic structure, according to sintering temperature.

The optimum value of sintering temperature is ≈ 850 °C which gives the optimum structure and electrical properties. The change in structure and electrical properties might occur at sintering temperatures higher than 850 °C as observed in the samples sintered at 890 °C. This could be due to the creation of oxygen deficiency or change of phase. Annealing temperature and annealing time are very critical to both oxygen content and critical temperature. The highest value of T_c was obtained at an annealing temperature of 400 °C, and T_c increased with annealing

time and then saturated beyond the annealing time of 72 hrs. The increase in T_c by annealing can be caused by more optimum oxygen content, intergrowth of a large number of Cu-O layers in the cell and a decrease of structural defects.

References

[1]Michel, C., Hervieu, M., Borel, M.M., Grandin, A., Deslandes, F., Provost, J. and Raveau, B., Z. Phys. B, 68 (1987) 421.

[2]Maeda, H., Teanaka, Y., Fukutomi, M. and Asano, T., Jpn. J. Appl. Phys., 27 (1988) L209.

[3]Chu, C.W., Bechtold, J., Gao, L., Hor, P.H., Huang, Z.J., Meng, R.L., Sun, Y.Y., Wang, Y.Q. and Xue, Y.Y., Phys. Rev. Lett., 60 (1988) 941.

[4]Hazen, R.M., Prewitt, C.T., Angel, R.J., Ross, N.L., Finger, L.W., Hadidiacos, C.G., Veblen, D.R., Heaney, P.J., Hor, P.H., Meng, R.L., Sun, Y.Y., Wang, Y.Q., Xue, Y.Y., Huang, Z.J., Gao, L., Bechtold, J. and Chu, C.W., Phys. Rev. Lett., 60 (1988) 1174.

[5]Rao, C., "Chemistry of oxide superconductors", (Sci. Publi., Oxford, 1988).

[6]El Ali (Al-Dairy), A., Alazawi, A.D., Hamam, Y.A. and Khasawinah, K., Jordan Journal of Physics, 1(1) (2008) 43.

[7]Makarenko, L.F., Gurinovich, V.A. and Kononyuk, I.F., Solid State Communications, 84(10) (1992) 971.

[8]Li, M.Y., Chen, X.P., Qu, T.M., Yi, H.P., Han, Z. and Liu, Q., Physica C: Superconductivity, 412-414(2) (2004) 1091.

[9]Khalil, S.M. and Sedky, A., Physica B, 357(3-4) (2005) 299.

[10]Florence, R.G., Ang, S.S. and Brown, W.D., Supercond. Sci. Technol., 7 (1994) 741.

[11]Subramanina, M. and Morrissey, K., Mod. Phys. Lett., 95 (1990) B4.

Jordan Journal of Physics

ARTICLE

Structural and Magnetic Properties of $BaFe_{12-x}Al_xO_{19}$ Prepared by Milling and Calcination

I. Bsoul[a]   and   **S. H. Mahmood**[b]

[a] *Department of Physics, Al al-Bayt University, Al-Mafraq, Jordan.*
[b] *Department of Physics, Yarmouk University, Irbid, Jordan.*

Abstract: Al substituted barium ferrite particles $BaFe_{12-x}Al_xO_{19}$ with $0 \leq x \leq 0.8$ have been prepared by ball milling method. X-ray diffraction (XRD) has shown that the average crystallite size for all samples under investigation is in the range $66 - 76$ nm. Scanning electron microscopy (SEM) imaging indicates that the particle size is in the range $0.2 - 1.0$ μm, which demonstrates that the particles are polycrystalline. It was found that Al substitution does not significantly change the particle size of $BaFe_{12-x}Al_xO_{19}$. The magnetic properties have been investigated using a vibrating sample magnetometer, and the anisotropy field is estimated. It was found that the coercivity of the samples increases from 4.2 kOe to 6.0 kOe with increasing Al concentration from $x = 0.0$ to 0.8 due to the increase in the anisotropy field. Interparticle interactions determined from the remnant magnetization data are found to be consistent with a reversal mechanism (demagnetizing like effect) for all samples examined.

Keywords: Ball milling; Barium ferrite; Coercive field; Magnetization.

Introduction

Barium hexaferrites, briefly (BaM), have attracted considerable interest due to their potential for different applications such as in permanent magnets, microwave devices and magnetic recording devices. The magnetic properties of hexaferrites such as saturation magnetization, coercivity and anisotropy field are strongly dependent on M-type phase [1]. Hexaferrites are well-known ferrimagnetic materials with strong uniaxial anisotropy. Anisotropy field can be controlled by the substitution of Fe^{3+} ions by paramagnetic and diamagnetic cations of $BaFe_{12-x}Al_xO_{19}$, or cations combination such as Mn-Ti [2], Co-Sn [3, 4], Zn-Ti [5], Co-Ti [6], ... etc. These substitutions aim at developing materials with improved characteristics, which make hexaferrites suitable for technological applications. Also, the synthesis of nanocrystalline hexaferrites with particle size less than 0.1μm and narrow particle size distribution leads to the production of single domain particles relevant to new applications.

Several methods have been developed to prepare barium ferrite particles including sol-gel method [7, 8], glass-ceramic method [9], glass crystallization method [10], liquid mix method [11], mechanical alloying [12], ceramic method [13], aerosol rute [14] and hydrothermal technique [15, 16].

Little had been reported on the Al-substituted barium ferrites (Al-BaM). The structural and magnetic properties of these materials seem to vary with the preparation method and the Al concentration [8, 12, 16]. Moreover, the microwave absorption properties have been reported to be affected by Al- substitution [17].

In this paper, the effect of Al ions on the magnetic properties of barium hexaferrite synthesized by milling and calcination is

---

Corresponding Author: I. Bsoul. **Email**: Ibrahimbsoul@yahoo.com

reported. Milling and calcination method is a technique that has been recently adopted for the preparation of barium ferrite powders, due to its simplicity of operation and handy experimental apparatus [12]. Also, this method is useful for the production of powders composed of fine particles smaller than the single domain size. The magnetic properties, X-ray diffraction (XRD) patterns and scanning electron microscopy (SEM) images have been investigated and analyzed in an attempt to explore the effect of Al substitution for Fe in BaM and to explain the magnetic behavior of $BaFe_{12-x}Al_xO_{19}$.

Experimental Procedure

$BaFe_{12-x}Al_xO_{19}$ powders with $x = 0$, 0.1, 0.2, 0.3, 0.4, 0.5, 0.6, 0.7 and 0.8 were prepared by using the milling and calcination method. Metallic oxides (Fe_2O_3 and Al_2O_3) and barium carbonate ($BaCO_3$) were used as starting materials. Mechanical alloying was performed in a planetary ball-mill (Fritsch Pulverisette 7) using a ball to powder ratio of 8:1. Milling was carried out for 16 h with an angular frequency of 250 rpm. After mechanical milling, the mixture was pressed at 5 tons/sq inch into disks, 1cm in diameter. These disks were calcined in air atmosphere at 1100°C for 10 h. The selection of this calcination temperature was based on the analysis of XRD patterns for more than 5 samples subject to different calcination temperatures from 800°C to 1200°C, which revealed that the optimum calcination temperature for obtaining a hexagonal $BaFe_{12-x}Al_xO_{19}$ phase was 1100°C. Each disk was subsequently cut into three pieces, one was finely ground for the powder X-ray diffraction study, the second was used for the grain morphology study and the last one was used for magnetic measurements.

XRD analysis was carried out in Philips X'Pert PRO X-ray diffractometer (PW3040/60) with CuK_α radiation (45 kV, 40 mA). The grain structure of the prepared samples was investigated using scanning electron microscope (SEM FEI Quanta 600) equipped with EDX facility for elemental analysis. The magnetic measurements were carried out using vibrating sample magnetometer (VSM MicroMag 3900, Princeton Measurements Corporation), with a maximum applied field of 10 kOe at room temperature. The isothermal remnant magnetization (IRM) curve was obtained by the following procedure: the sample was initially demagnetized. A small positive field was applied then removed, and the remnant magnetization was recorded. The procedure was repeated with increasing the positive field to reach positive saturation remanence. Magnetic anisotropy field was estimated by differentiating the reduced IRM curve. The DC demagnetization remanence (DCD) curve was obtained by initially saturating the sample with a positive field of 10 kOe. A small negative field was applied to the sample. Remanence magnetization was recorded after removing the negative field and at last this procedure was repeated with increasing the negative field until negative saturation remanence was reached.

Results and Discussion

XRD patterns of some samples of $BaFe_{12-x}Al_xO_{19}$ along with the standard pattern for hexagonal barium ferrite ($BaFe_{12}O_{19}$) with space group $P6_3/mmc$ are shown in Fig. 1. It can be seen from the Figure that the XRD patterns for all samples match the standard pattern 043-0002 for hexagonal barium ferrite ($BaFe_{12}O_{19}$) [18]. Two peaks of $\alpha\text{-}Fe_2O_3$ are present in all samples examined; one peak at 33.14° and the other at 35.6°, which interferes with the peak of $BaFe_{12}O_{19}$ at the same diffraction angle. Thus, the most intense peaks between 35° and 36° (200 and 108) have reversed intensities for all samples examined. The lattice parameters a and c were calculated using the formula [19]:

$$\frac{1}{d_{hkl}^2} = \frac{4}{3}\left(\frac{h^2 + hk + k^2}{a^2}\right) + \frac{l^2}{c^2} \qquad (1)$$

where d is the interplanar distance and h, k and l are Miller indices. The lattice parameters for this phase are shown in Table 1. These values of lattice parameters agree well with those published for the hexagonal barium ferrite [12, 20]. It should be noted that the preparation method and the Al^{3+} substitution for Fe^{3+} in the concentration range reported in this work do not affect the hexagonal structure of $BaFe_{12}O_{19}$. A general trend of reduction in lattice parameters, as a

result of Al substitution, can be observed from Table 1. The maximum reduction in lattice parameters is about 0.2%. In comparison, a reduction in lattice parameters of about 0.7% was reported for Al-BaM sample prepared with $x = 2$ using the same technique and conditions used in this work [12].
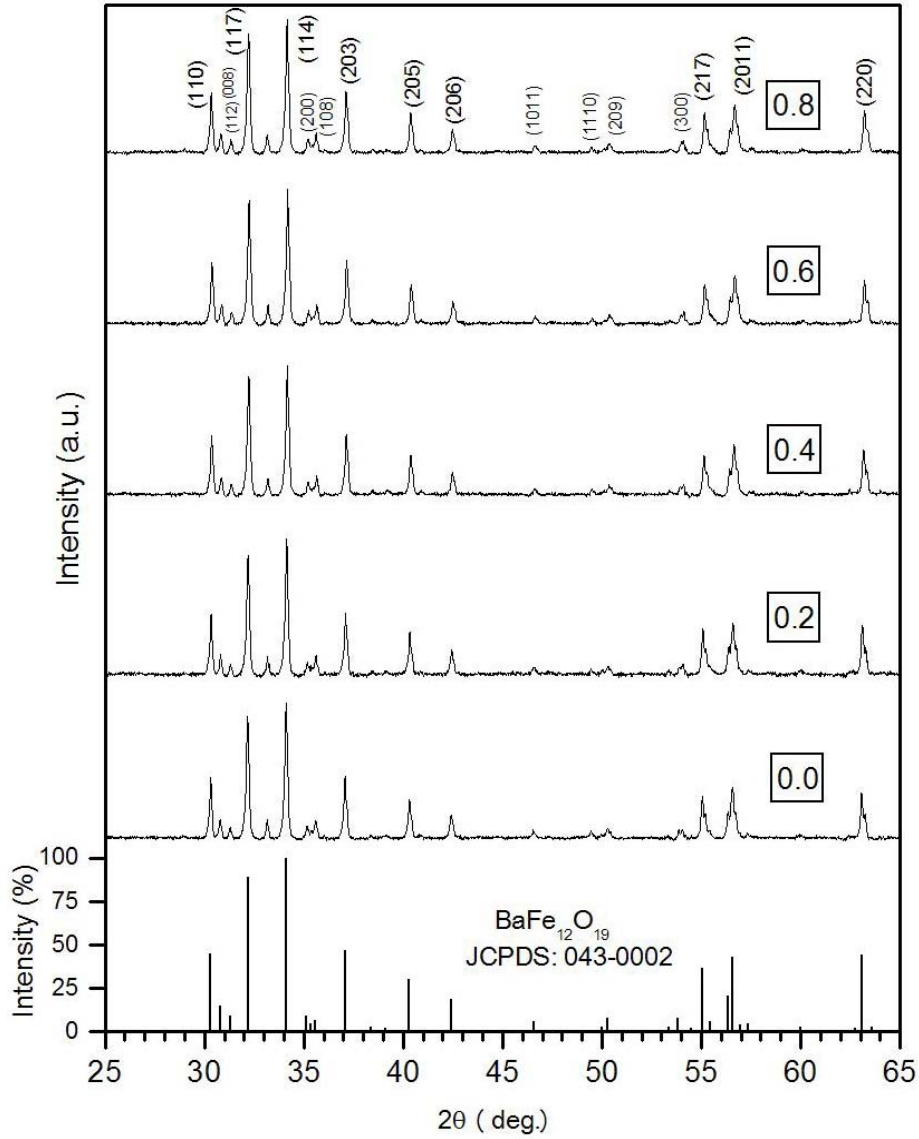

FIG. 1. XRD patterns of BaFe$_{12-x}$Al$_x$O$_{19}$ with different doping concentrations along with the standard pattern for hexagonal barium ferrite.

TABLE 1. Lattice parameters and average crystallite size of BaFe$_{12-x}$Al$_x$O$_{19}$.

x	$a = b$ (Å) $\pm$ 0.002	c (Å) $\pm$ 0.007	Average crystallite size (D) nm
0.0	5.889	23.194	76
0.1	5.889	23.194	76
0.2	5.887	23.192	71
0.3	5.885	23.173	74
0.4	5.882	23.164	70
0.5	5.880	23.142	70
0.6	5.879	23.153	69
0.7	5.885	23.172	66
0.8	5. 885	23.171	72

The average Al^{3+} wt % in the particles is measured using the EDX facility in the SEM and is plotted against x in Fig. 2. The Al content in $BaFe_{12-x}Al_xO_{19}$ is close to that of the initial mixtures and indicates that about 90% or more of the aluminum ions enter into the lattice of barium ferrite.
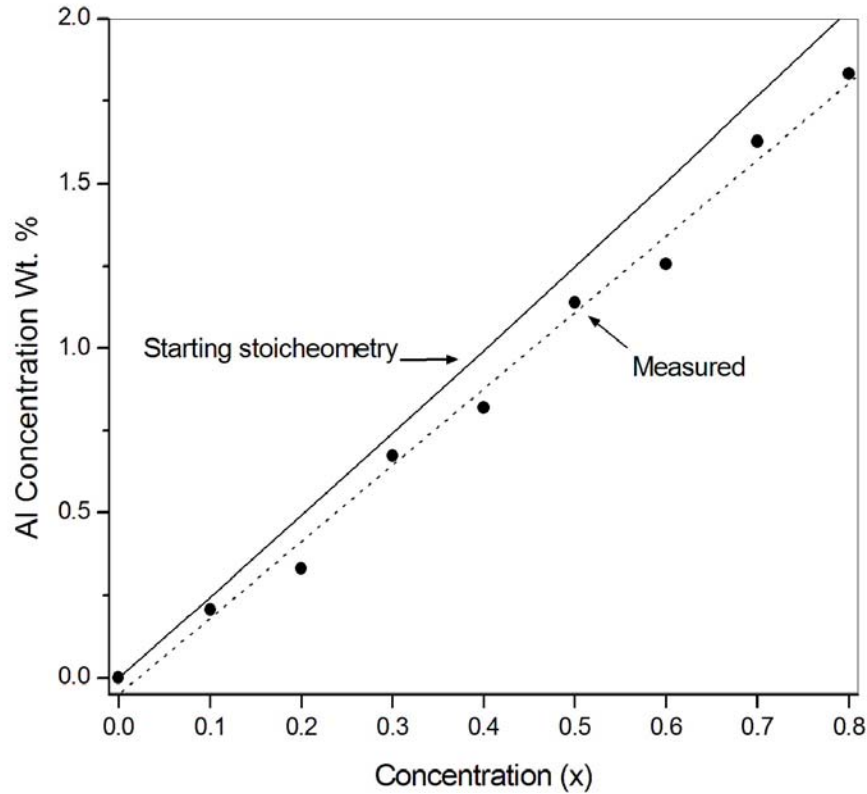

FIG. 2. Aluminum content in $BaFe_{12-x}Al_xO_{19}$ from initial doping and measured by EDX.

The average crystallite size is determined from the positions of Bragg reflections (217) (220) using the well-known Scherrer formula [19]:

$$D = \frac{K\lambda}{\beta \cos\theta} \qquad (2)$$

where D is the crystallite size, K the Scherrer constant, λ the wavelength of radiation (1.54056 Å), β the width at half peak maximum measured in radians and θ is the peak position. The above mentioned reflections are selected for the analysis since they are strong enough and are resolved into the $K_{\alpha1}$ and $K_{\alpha2}$ components for more accuracy. The strongest reflections are not resolved into the two components, providing a wider peak and, consequently, a non-accurate smaller particle size. The results of the analysis (Table 1) indicate that the average crystallite size of all samples is in the range 66 – 76 nm and that Al^{3+} substitution for Fe^{3+} does not substantially affect the crystallinity of $BaFe_{12-x}Al_xO_{19}$. On the other hand, the morphology of the grains for all samples is investigated by the direct observation via scanning electron microscopy. Fig. 3 shows a SEM photograph of $BaFe_{12-x}Al_xO_{19}$ samples with doping concentrations of 0.0 and 0.8. As x increases, the grain size practically remains constant, which indicates that the Al substitution in the concentration range reported in this work does not significantly influence the particle size distribution. The particles in all samples under investigation are close to spherical in shape with diameters extending from 200 nm to about 1 μm. Comparing the results of the XRD analysis and SEM imaging leads to the conclusion that most of the particles in the samples are not single crystals. Also, since the critical diameter of spherical barium ferrite with single magnetic domain is reported to be 460 nm [21], we conclude that probably more than 50% of the grains in the prepared samples are single-domain ones.
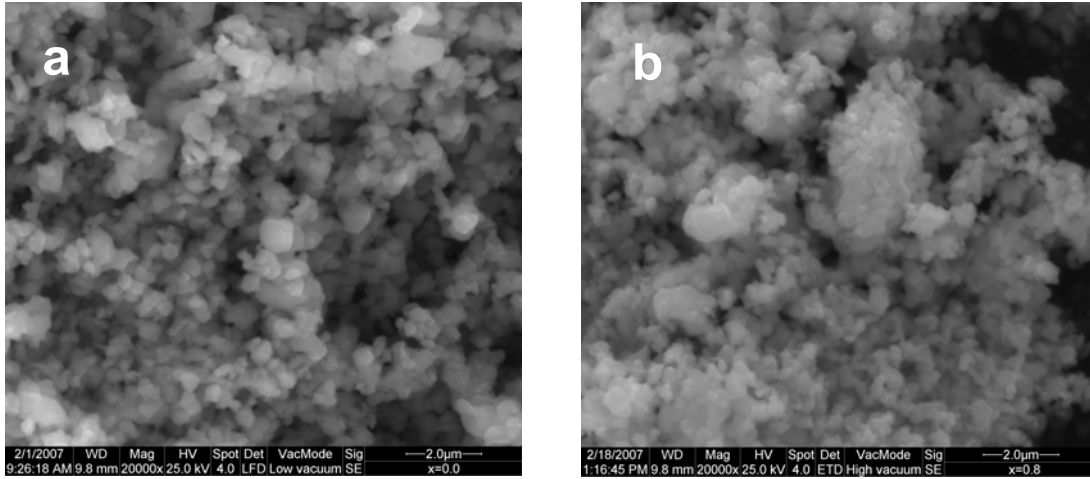
FIG. 3. SEM photograph of $BaFe_{12-x}Al_xO_{19}$, a) $x = 0.0$, b) $x = 0.8$.

The measured hysteresis loops for some of the $BaFe_{12-x}Al_xO_{19}$ samples as a function of applied magnetic field are shown in Fig. 4. The magnetization curve for the non-substituted sample belongs to a hard magnetic material with high coercive field strength of about 4.2 kOe. This value of the coercivity is in good agreement with the reported results [22-24]. As one might observe, doping of barium ferrite with aluminum leads to the increase in coercive field and decrease in both remnant and saturation magnetization. The effects of Al concentration on the saturation magnetization and coercivity of $BaFe_{12-x}Al_xO_{19}$ for all samples examined are shown in

Fig. 5. The saturation magnetization decreases with increasing Al concentration, as expected, due to the weakening of the superexchange interaction of Fe^{3+}-O- Fe^{3+}. On the other hand, the coercivity increases linearly from about 4.2 kOe to 6.0 kOe as x increases from 0.0 to 0.8. This increase in coercivity can not be understood based on particle size effects, since all prepared samples have similar particle sizes. This increase in coercivity is thus attributed to the increase in anisotropy field H_a, since the coercivity is proportional to magnetic anisotropy field [25].
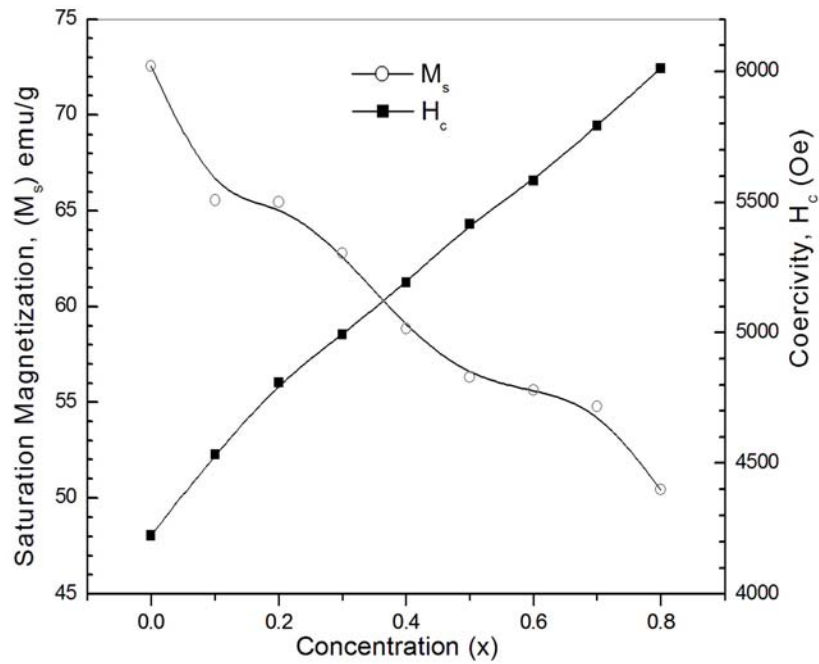

FIG. 4. Hysteresis loops for some of the $BaFe_{12-x}Al_xO_{19}$ samples as a function of applied magnetic field.

FIG. 5. Saturation magnetization and coercivity of $BaFe_{12-x}Al_xO_{19}$ as a function of Al concentration (x).

The switching field distribution can be obtained by differentiating the reduced IRM curve $m_r(H) = M_r(H) / M_r(\infty)$. Fig. 6 shows the reduced IRM curve and the corresponding switching field distribution for a representative sample with $x = 0.4$. The effective magnetic anisotropy field for each sample examined in this work is obtained

from the maximum of the switching field distribution [26]

$$f(H)]_{max} = \left[\frac{dm_r}{dH}\right]_{H = H_a/2} \qquad (3)$$

(i.e., $H_a = 2H_{max}$, where H_{max} is the value of the field at the maximum of the switching field distribution).
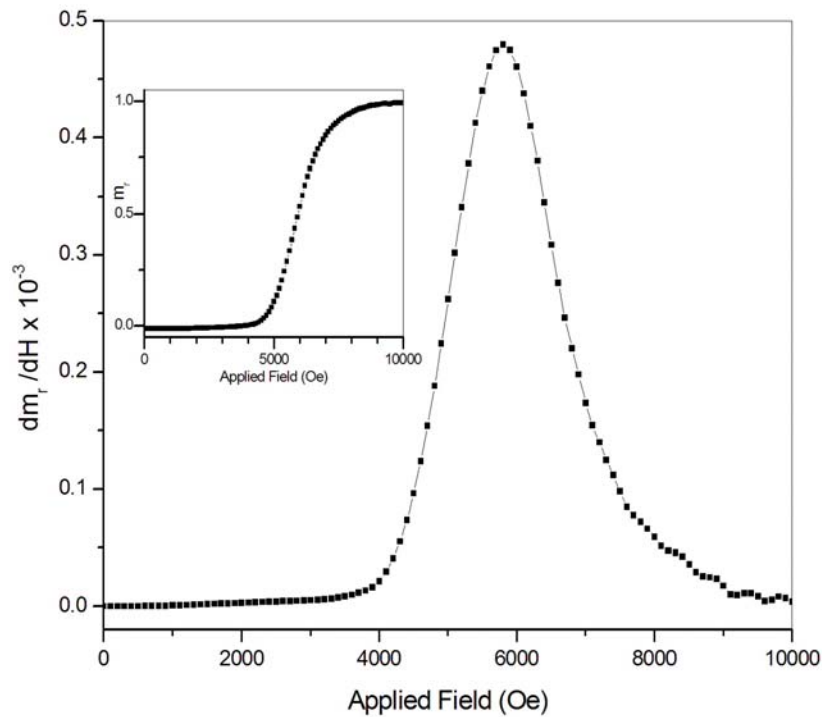

FIG. 6. Switching field distribution for a sample with $x = 0.4$. Inset: reduced IRM curve for a sample with $x = 0.4$.

Fig. 7 shows the variation of magnetic anisotropy field with Al concentration for all samples examined. It is clear that H_a increases with increasing Al concentration. The ratio H_c / H_a for all samples is about 0.44, which is close to Stoner-Wohlfarth [27] value of 0.48 for single-domain noninteracting randomly oriented particles. The ratio observed in our samples is higher than that observed by Görnert *et al.* [25] for samples with particle diameters of 110 nm and 420 nm. The deviation from the theoretical value could be due to interparticle interactions.
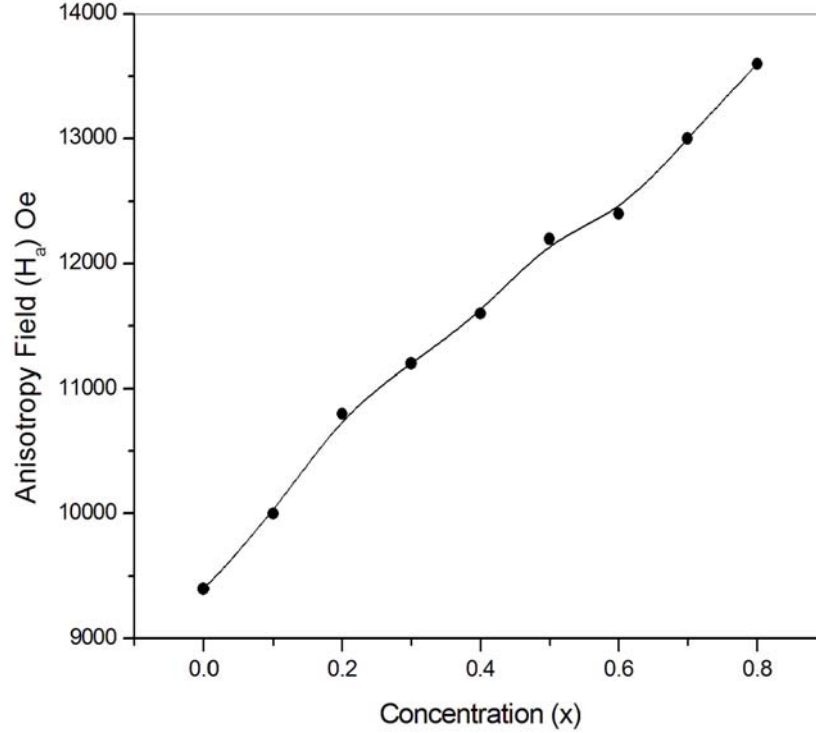

FIG. 7. Anisotropy field of $BaFe_{12-x}Al_xO_{19}$ as a function of Al concentration (x).

Next, we investigate the role of Al substitution on the interparticle magnetic interactions in BaFe$_{12-x}$Al$_x$O$_{19}$ using the difference δm defined by Kelly [28]:

$$\delta m(H) = m_d(H) - [1 - 2m_r(H)] \qquad (4)$$

where $m_r(H) = M_r(H) / M_r(\infty)$ is the reduced IRM and $m_d(H) = M_d(H) / M_r(\infty)$ is the reduced DCD. Usually, δm is used to clarify the sign and strength of the interaction between magnetic particles. Positive δm is attributed to magnetizing exchange interactions (magnetizing-like effect), whereas negative δm is associated with demagnetizing interactions (demagnetizing-like effect), i.e. negative δm indicates that the interparticle interactions assist magnetic reversal mechanisms. Fig. 8 shows the δm curves as a function of the applied field for samples of BaFe$_{12-x}$Al$_x$O$_{19}$ with different doping concentrations. The Figure illustrates that δm is negative for all samples at all applied fields, exhibiting a maximum negative value at a field that increases with increasing the Al concentration due to the consequent increase in magnetic anisotropy. The maximum of δm fluctuates around the value of 0.35 for all Al concentrations investigated, which indicates that doping barium ferrite with Al in the range investigated does not systematically and significantly affect the demagnetizing effect in BaFe$_{12-x}$Al$_x$O$_{19}$.

Conclusions

Nano-size particles of diameters smaller than 100 nm of BaFe$_{12-x}$Al$_x$O$_{19}$ have been prepared using a very simple method of milling and calcination. It was found that doping of barium ferrite with Al leads to a decrease in saturation magnetization and to a significant increase in the coercive field due

to the increase of magnetic anisotropy field. Interparticle interactions are found to assist the reversal mechanisms (demagnetizing-like effect), which is not significantly affected by Al concentration in the sample.
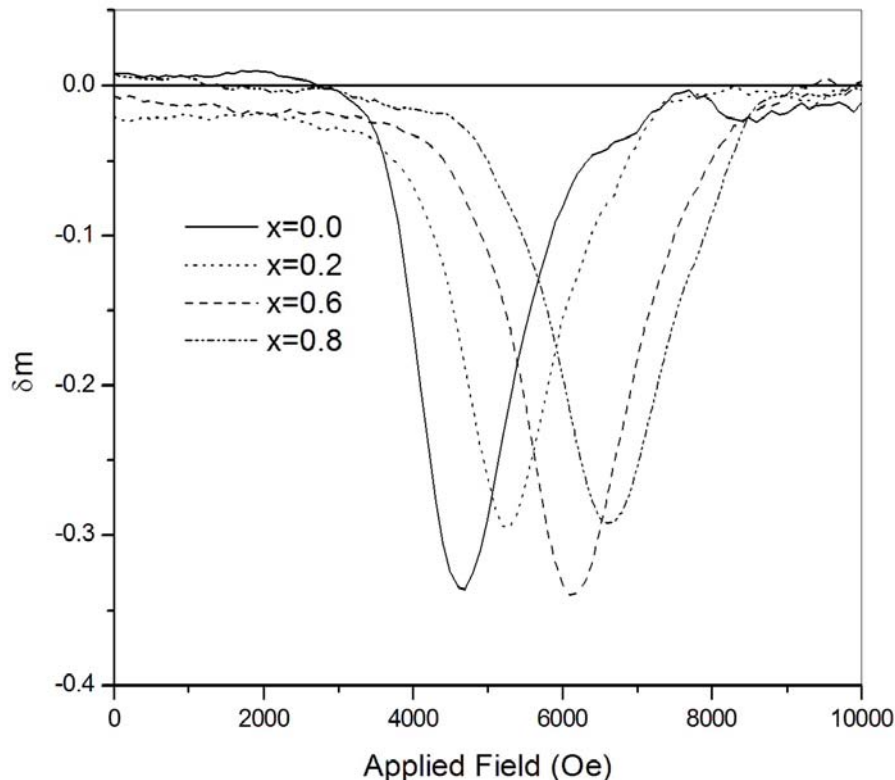

FIG. 8. δM curves of $BaFe_{12-x}Al_xO_{19}$ for some of the concentrations examined.

References

[1] Lechevallier, L., Le Breton, J.M., Wang, J.F. and Harris, I.R., J. Magn. Magn. Mater., 269 (2004) 192.

[2] Turilli, G., Licci, F., Rinaldi, S. and Deriu, A., J. Magn. Magn. Mater., 59(1-2) (1986) 127.

[3] Yang, Z., Zeng, H.X., Han, D., Liu, J.Z. and Geng, S.L., J. Magn. Magn. Mater., 115 (1992) 77.

[4] Han, D.H., Yang, Z., Zheng, H.X., Zhou, X.Z. and Morrish, A.H., J. Magn. Magn. Mater., 137 (1994) 191.

[5] Wartewig, P., Krause, M.K., Esquinazi, P., Rosler, S., Sonntag, R., J. Magn. Magn. Mater., 192 (1999) 83.

[6] Gruskova, A., Slama, J., Dosudil, R., Kevicka, D., Jancarik, V. and Toth, I., J. Magn. Magn. Mater., 242–245 (2002) 423.

[7] Zhong, W., Ding, W., Zhang, N., Hong, J., Yan, Q. and Du, Y., J. Magn. Magn. Mater., 168 (1997) 196.

[8] Yue, Z., Zhong, M., Ma, H. and Gue, G., J. Shanghai Univ., 12 (2008) 216.

[9] Shirk, B.T. and Buessem, W.R., J. Am. Ceram. Soc., 53 (1970) 192.

[10] El-Hilo, M., Pfeiffer, H., O'Grady, K., Schüppel, W., Sinn, E., Görnert, P., Rösler, M., Dickson, D.P.E. and Chantrell, R.W., J. Magn. Magn. Mater., 129 (1994) 339.

[11] Pernet, M., Obradors, X., Vallet, M., Hernandez, T. and Germi, P., IEEE Trans. Magn., MAG-24 (1988) 1898.

[12] Wang, S., Ding, J., Shi, Y. and Chen, Y.J., J. Magn. Magn. Mater., 219 (2000) 206.

[13] Albanese, G., J. Magn. Magn. Mater., 147 (1995) 421.

[14] Singhal, S., Garg, A.N. and Chandra, K., J. Magn. Magn. Mater., 285 (2005) 193.

[15] Liu, X., Wang, J., Gan, L.M. and Ng, S.C., J. Magn. Magn. Mater., 195 (1999) 452.

[16] Mishra, D., Anand, S., Panda, R.K. and Das, R.P., Mater. Lett., 58 (2004) 1147.

[17] Qui, J., Zhang, Q. and Gu, M., J. Appl. Phys., 98 (2005) 103905.

[18] International Centre for Diffraction Data (ICDD), JCPDS File 27-1029.

[19] Warren, B.E., X-Ray Diffraction, (Addison-Wesley, Reading, Massachusetts, 1969).

[20] Mallick, K.K., Shepherd, P. and Green, R.J., J. Magn. Magn. Mater., 312 (2007) 418.

[21] Rezlescu, L., Reslescu, E. and Popa, P.D., J. Magn. Magn. Mater., 193 (1999) 288.

[22] An, S.Y., Shim, I.B., Kim, C.S., J. Appl. Phys., 91(10) (2002) 8465.

[23] Sharma, P., Rocha, R.A., de Medeiros, S.N. and Paesano, A.Jr, J. Alloys and Compounds, 443(1-2) (2007) 42.

[24] Babu, V. and Padaikathan, P., J. Magn. Magn. Mater., 241 (2002) 85.

[25] Görnert, P., Schüppel, W., Sinn, E., Schumacher, F., Hempel, K.A., Turilli, G., Paoluzi, A. and Rösler, M., J. Magn. Magn. Mater., 114 (1992) 193.

[26] Pfeiffer, H. and Schüppel, W., Phys. Stat. Sol. (a), 119 (1990) 259.

[27] Stoner, E.C., Wohlfarth, E.P., Phil. Trans. Roy. Soc., 240A (1948) 599.

[28] Kelly, P.E., O'Grady, K., Mayo, P.I. and Chantrell, R.W., IEEE Transactions on Magnetics, 25(5) (1989) 3881.

Jordan Journal of Physics

ARTICLE

Preparation of Domestic Nuclear Detector Using Solutions of the Scintillation Materials (Acridine) and (Eosin)

R. M. Yousuf [a] and **L. A. Najam**[b]

[a]*Environmental Technology Department, College of Environmental Science and Technology, Mosul University, Mosul, Iraq.*
[b]*Department of Physics, College of Science, Mosul University, Mosul, Iraq.*

Abstract: In this work, three types of scintillation materials, Acridine orange, Eosin blue and Eosin yellow, were used to act as liquid scintillation detectors. They can be used to detect ionizing radiation, especially that of high Linear Energy Transfer (LET). This work determines the optimum concentration for each of the investigated materials to be 0.2 g/l dissolved in Methanol, added to a solution of Anthracene in Xylene of the concentration of 1.4 g/l and a solution of POPOP in Xylene of the concentration of 0.2 g/l. All samples were irradiated using radioactive sources ^{241}Am, ^{137}Cs and ^{60}Co.
Keywords: Liquid scintillation detectors; LET; Chemical quenching; Color quenching; Acridine; Eosin.

Introduction
Liquid Scintillation Solutions

A category of useful scintillators is produced by dissolving an organic scintillator into an appropriate solvent. Liquid scintillators can consist simply of these two components, or a third constituent could be added as wavelength shifter in order to tailor the emission spectrum for better matching with the spectral response of common photomultiplier tubes.

Liquid scintillators are often commercially sold in sealed glass containers and are handled in the same manner as solid scintillators. In certain applications, large-volume detectors with dimensions of several meters may be required. In these cases, the liquid scintillators are often the only practical choice from a cost standpoint [1].

Liquid scintillators are also widely applied to count radiation from a radioactive material that can be dissolved in the scintillator solution. In this case, all radiations emitted by the source immediately react with some portion of the scintillator, and the counting efficiency can be almost 100%. This technique is widely used, especially for counting low level beta activity such as that emitted by ^{14}C or tritium. In addition, liquid scintillation detectors can be applied to avoid some of the difficulties that arise when measuring low-energy beta particles or alpha particles using conventional methods [2]. The approach, sometimes called internal source liquid scintillation counting, involves dissolving the sample to be counted directly into the liquid scintillator. Under these conditions, problems relating to sample, such as self-absorption, are completely avoided [3].

A scintillator is generally a binary or ternary system composed of a solvent (donor) and one or two solutes [4]. The simplest system is a binary liquid scintillator, which consists of an organic scintillator, known as the activator or the primary solute, dissolved in an organic solvent. Typically, concentrations are less than 10 g/l. Primary

---

Corresponding Author: L. A. Najam. **Email**: dr_laithahmed@yahoo.com

solutes include compounds known as PPO, PBD and TP (2,5-diphenloxazol $C_{15}H_{11}NO$, 2-pheny1-5-(4-biphenylyl)-1,3,4-oxadiazole $C_{20}H_{22}N_2O$ and p-terphenly) and popular solvents are Toluene, Xylene and 1,4-dioxin [5,6].

The main requirements of the solute are that it should be an efficient scintillator and soluble in the used solvent. The solvent should be transparent to the scintillation of the solute, and should be able to dissolve not only the solute but also a wide range of source compounds and other substances that may have to be incorporated in the scintillator [7, 8].

Procedure
Sample Preparation

In this work, many chemical materials of 99% purity were used in order to obtain the best results and the largest accuracy. In addition, the solid organic material Anthracene ($C_{14}H_{10}$) was used as primary solute, as well as Xylene ($C_6H_{14}(CH_3)$) as organic solvent, while the POPOP material *{P – bis [2 - (5 - phenyloxazolyl)] benzene}* $C_{24}H_{16}N_2O_2$ was used as secondary organic solute. The latter serves to shift the wavelength of the present scintillations toward the region of the visible light.

Some organic solute materials were tested as wavelength shifters, such as Acridine orange ($C_{17}H_{19}N_3$), Eosin blue ($C_{20}H_6O_9Na_2Br_2$) and Eosin yellow ($C_{20}H_6Na_2$). All these chemical materials are also used to shift the wavelength of the present scintillators toward the region of the visible light.

Preparation of Anthracene in Xylene

In order to prepare 1.4 g/l concentration of Anthracene in Xylene, a quantity of 7 mg of Anthracene was dissolved in 5 ml of Xylene.

Preparation of POPOP {P-bis[2-(5-phenyloxazolyl)]benzene} in Xylene

The compound POPOP is considered as one of the wavelength shifters that is usually used as secondary solute, added to the photo scintillator to make scintillation light photons more appropriate for the photocathode of the

photomultiplier. It was noticed that the concentration of the secondary organic solute was small compared to the concentration of the primary solute. Thus, to prepare the liquid scintillator that contains POPOP, an optimum concentration of 0.2 g/l of POPOP in Xylene was preferred, so a mass of 0.04 mg of POPOP was dissolved in 0.2 ml of Xylene, then the liquid was left for many hours after every dilution process in order to become homogenous.

The Preparation of Different Concentrations of Acridine Orange, Eosin Blue and Eosin Yellow in Methanol

In order to prepare different concentrations (0.05, 0.1, 0.15, 0.2, 0.25, 0.3, 0.4 and 0.5 g/l) of Acridine orange, Eosin blue or Eosin yellow in methanol, the relation $C_1V_1=C_2V_2$ (where C_1 is the original concentration, C_2 the final concentration, V_1 the original volume and V_2 the final volume) has been applied.

Experimental Measurements

The measurement process includes the determination of the count rate during a period of 20 seconds. The measurements were performed for three replications for each sample, then the average was calculated. The net area was found by subtracting the measured value of the background, for the same time interval, from the measured value of the sample area.

The experimental measurements for all samples, and for every concentration, were performed using the experimental setup shown in Fig.1 [9, 10].

The prepared samples were irradiated by three gamma radioactive sources, namely ^{241}Am, ^{137}Cs and ^{60}Co. These sources were chosen since they emit gamma photons with low energy (59.5 keV for ^{241}Am), intermediate energy (662 keV for ^{137}Cs) and high energy (1173 and 1332 keV for ^{60}Co). Table 1 shows the nuclear data for all radioactive sources used in this work (manufactured by Amersham).

TABLE 1. Nuclear data for the used radioactive sources.

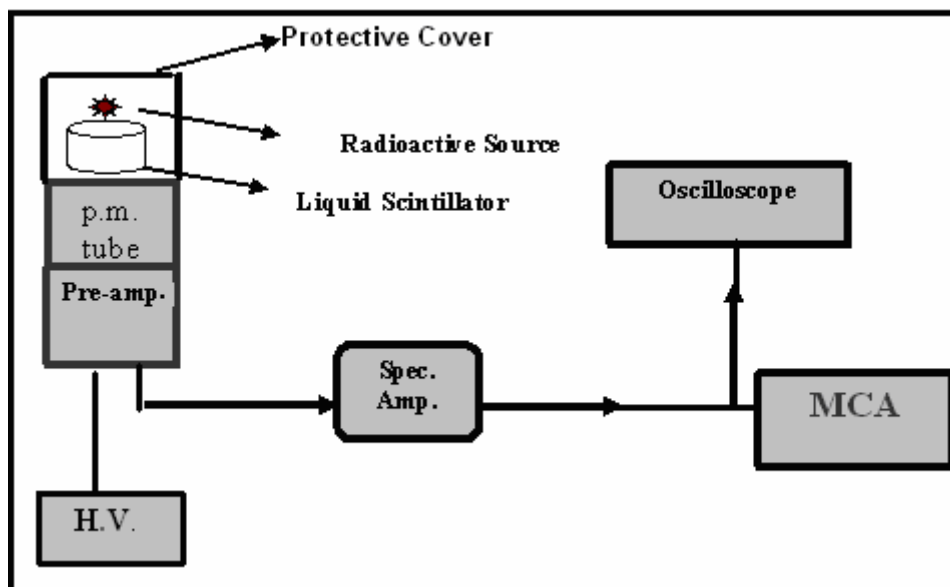| Isotope	$T_{1/2}$ (y)	$E\gamma$ (keV)	$I\gamma$ (%)	Activity at date of experiment (μCi)
^{241}Am	458	59.5	35.9	9.46
^{137}Cs	30	662	85.1	4.93
^{60}Co	5.2	1173	100	0.404
^{60}Co	5.2	1332	100	0.404

FIG. 1. Schematic diagram of the measurement system.

Results and Discussion

Tables 2, 3 and 4 list the net area under the curve of the spectrum for samples irradiated with ^{241}Am, ^{137}Cs and ^{60}Co, respectively. Note that the values within the tables represent ($N \pm \sqrt{N}$), where N = net area counts [11].

TABLE 2. Net area under the curve for samples irradiated for 20s with ^{241}Am.

Concentration (g/l)	Acridine Orange Counts	Eosin Blue Counts	Eosin Yellow Counts
0.5	240±15	552±23	275±17
0.4	295±17	615±25	390±20
0.3	380±19	750±27	470±22
0.25	550±23	875±30	610±25
0.2	690±26	1250±35	875±30
0.15	520±22	960±31	720±27
0.1	450±21	760±28	505±22
0.05	390±20	480±22	375±19

TABLE 3. Net area under the curve for samples irradiated for 20s with ^{137}Cs.

Concentration (g/l)	Acridine Orange Counts	Eosin Blue Counts	Eosin Yellow Counts
0.5	20700±144	24382±156	21500±147
0.4	22400±150	26435±163	23550±153
0.3	23700±154	28500±169	26560±163
0.25	26800±164	36600±191	29900±173
0.2	33500±183	39500±199	36200±190
0.15	26500±163	35300±188	28540±169
0.1	21250±146	32800±181	25500±160
0.05	19500±140	30900±176	22600±150

TABLE 4. Net area under the curve for samples irradiated for 20s with ^{60}Co.

Concentration (g/l)	Acridine Orange Counts	Eosin Blue Counts	Eosin Yellow Counts
0.5	5280±73	6840±83	6600±81
0.4	5500±74	7597±87	7170±85
0.3	5800±76	8104±90	7350±86
0.25	6100±78	10570±103	7900±89
0.2	7300±85	14200±119	8970±95
0.15	5730±76	11200±106	8100±90
0.1	5480±74	9520±98	7600±87
0.05	5040±71	7860±89	7200±85

The results in Tables 2, 3 and 4 are represented graphically in Figs. 2, 3 and 4, illustrating the variation of the count rate using each radioactive source with different concentrations of three different organic materials. Those figures show a gradual increase in the count rate (net area) at low concentrations of all chemical materials (Acridine orange, Eosin blue and Eosin yellow). The count rate then reaches its highest value and ultimately decreases at high concentrations.

This behavior can be explained as follows: First, the chemical quenching due to energy competition of the impurities within the sample, especially non fluorescent molecules, leads to the absorption of the transition energy originating between the solvent material and the primary solute, such that the decay from the excited state will happen without radiation. Second, the color quenching contributes to the competition process too, such that the color of the solute and the color due to the impurities will reduce the number of light photons within the sample. Third, the concentration quenching due to the increase in the molar concentration within the liquid scintillation sample will decrease the quantum efficiency of the fluorescence. The above three factors act together within the sample at the same time, such that at high concentration values, the total quenching effect reduces the fluorescence events, and the fluorescence intensity decreases.

We also notice that the optimum concentration for Acridine orange, Eosin blue and Eosin yellow that gives the maximum

count rate is (0.2 g/l). The maximum count rate occurs for Eosin blue in comparison with the other materials (Acridine orange and Eosin yellow), as shown in Figs. 2, 3 and 4.

However, there is no evident relation between the response of these materials at optimum concentration and the gamma energy.
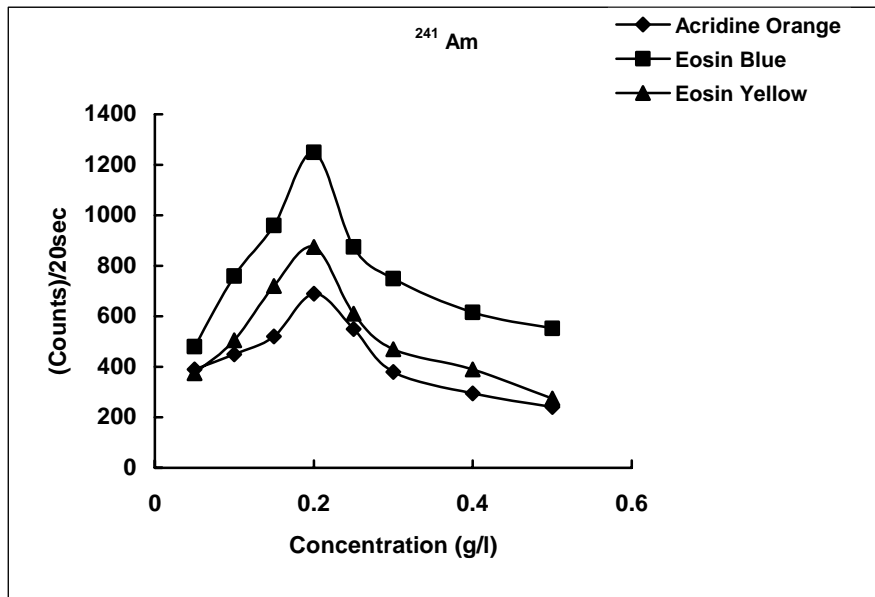

FIG. 2. The relation between the count rate, using ^{241}Am, and concentration for three different organic materials.
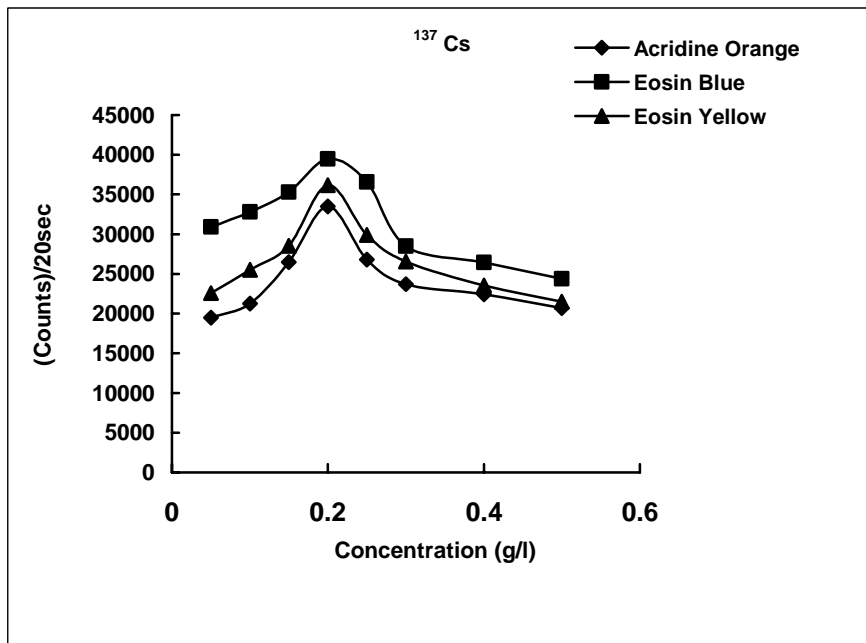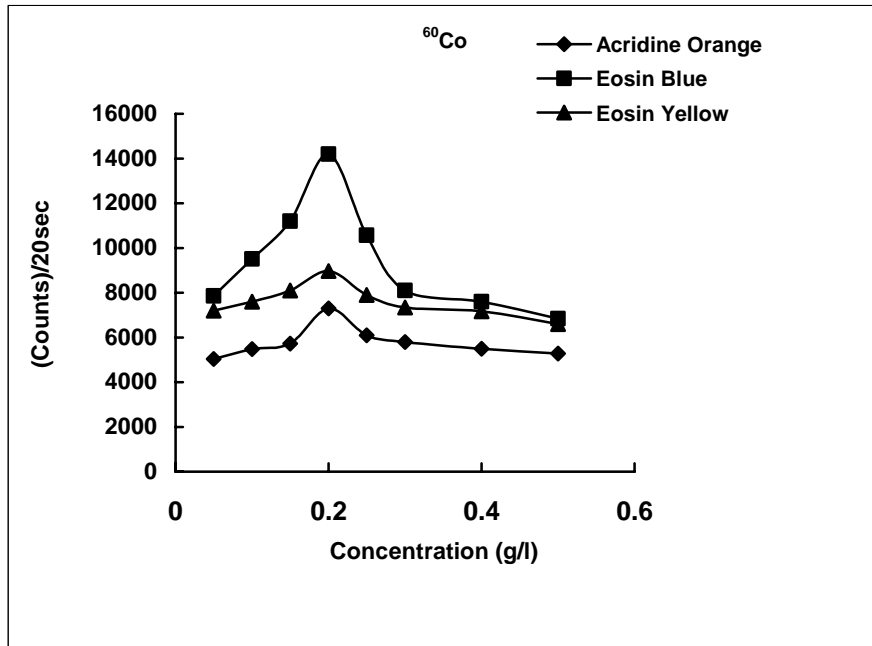

FIG. 3. The relation between the count rate, using ^{137}Cs, and concentration for three different organic materials.

185

FIG. 4. The relation between the count rate, using ^{60}Co, and concentration for three different organic materials.

Fig. 5 shows the background spectrum for Eosin blue at a concentration of 0.2 g/l. In addition, Figs. 6, 7 and 8 show the spectra of Eosin blue, at a concentration of 0.2 g/l, irradiated with the radioactive sources ^{241}Am, ^{137}Cs and ^{60}Co, respectively.
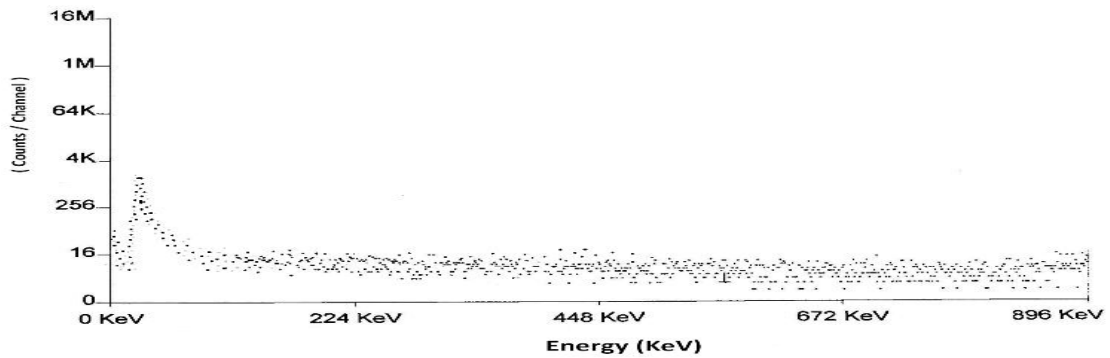
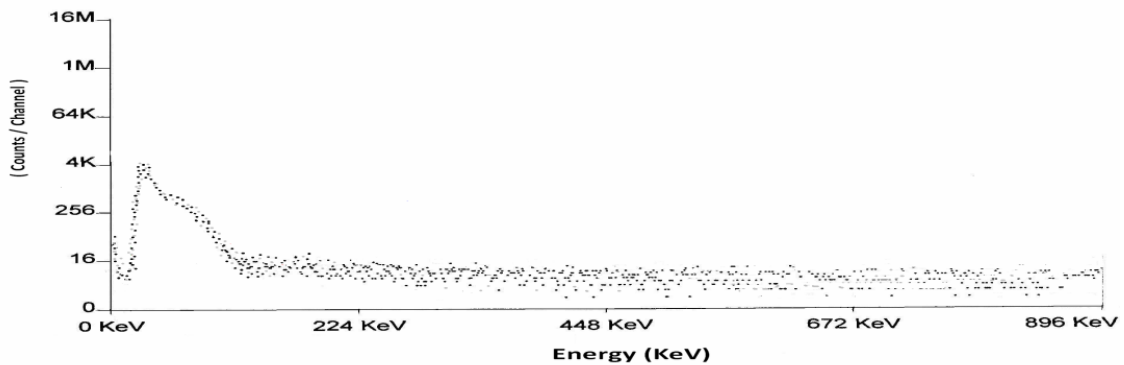FIG. 5. The background spectrum of the Eosin blue sample at a concentration of 0.2 g/l.

FIG. 6. The spectrum of Eosin blue sample at a concentration of 0.2 g/l irradiated with ^{241}Am.

186
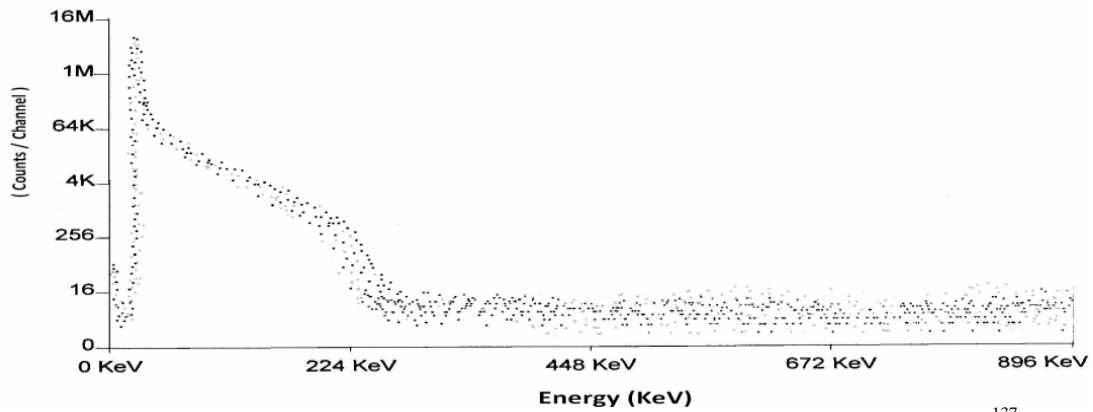
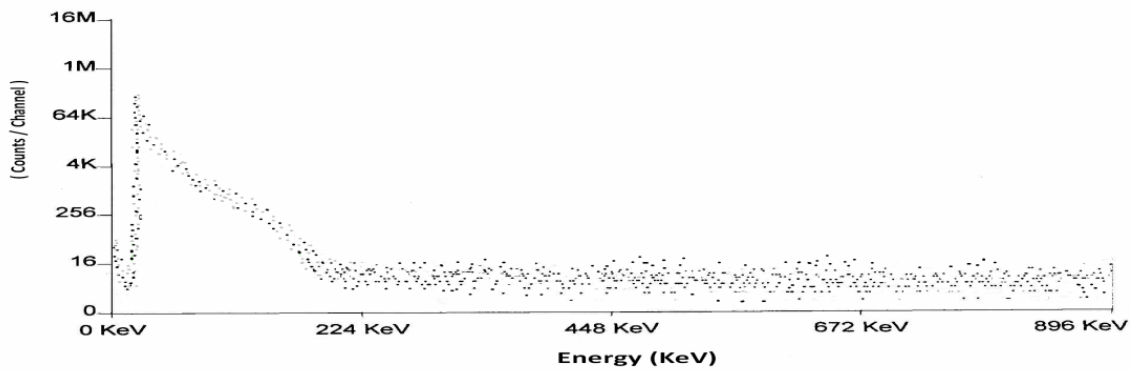FIG. 7. The spectrum of the Eosin blue sample at a concentration of 0.2 g/l irradiated with [137]Cs.

FIG. 8. The spectrum of the Eosin blue sample at a concentration of 0.2 g/l irradiated with [60]Co.

In order to investigate the properties of the used materials, IR analysis was performed. Fig. 9 shows the IR spectrum for the Eosin blue sample with the optimum concentration (0.2 g/l) before and after irradiation. Eosin blue was chosen due to its higher count rate as compared to the other two materials. It is clear that there is no significant difference in the spectrum before and after irradiation, implying that the irradiation time and the properties of the sources were not sufficient to produce any significant changes in the material.
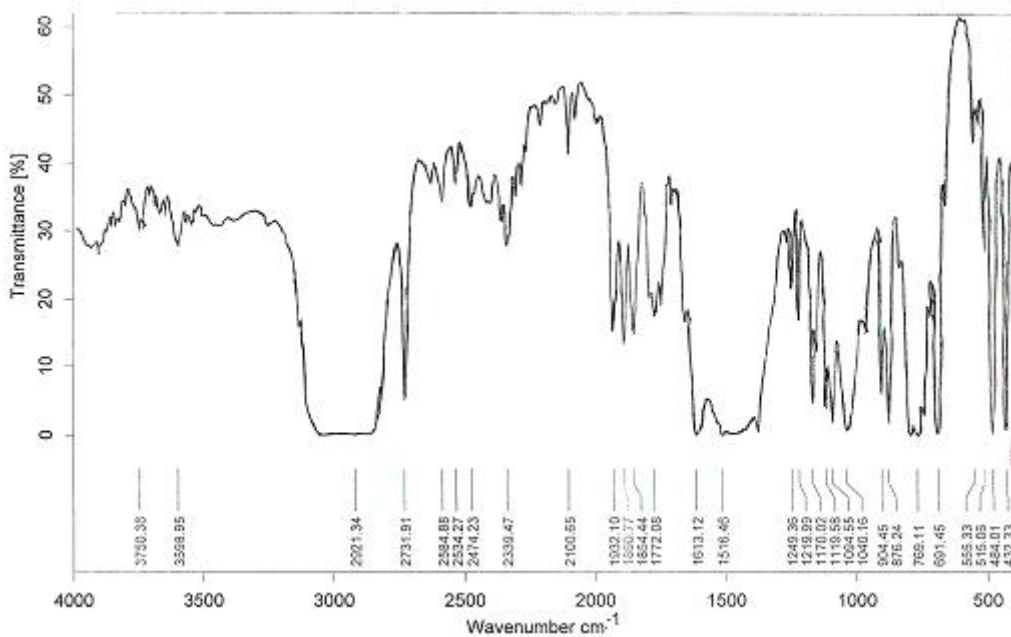

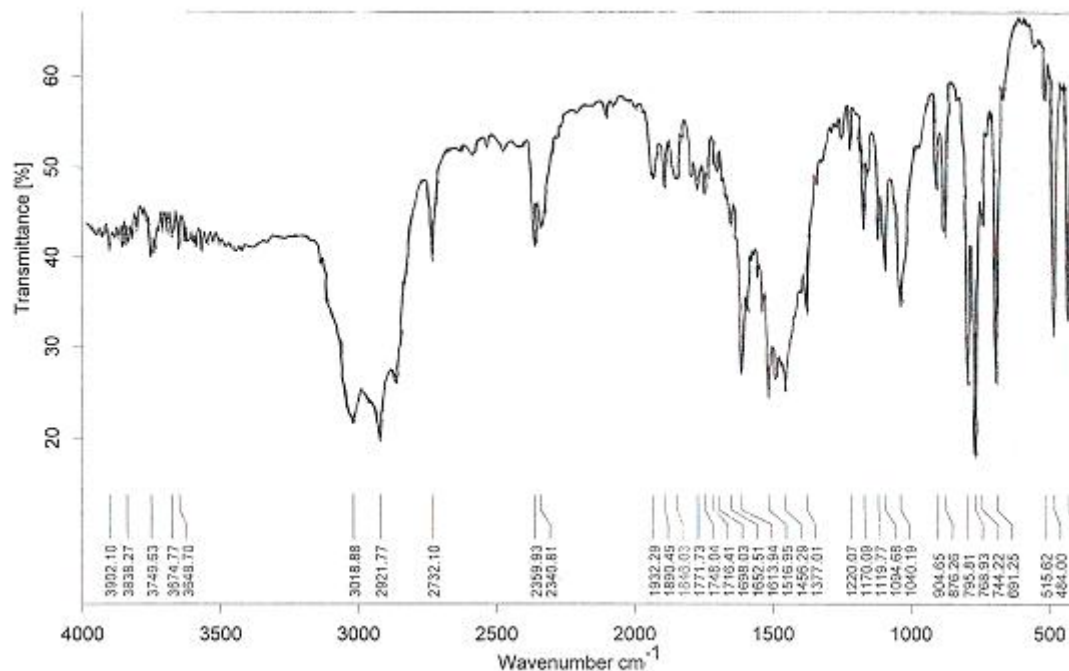FIG. 9A. The IR analysis of Eosin blue with the optimum concentration of 0.2 g/l before irradiation.

FIG. 9B. The IR analysis of Eosin blue with the optimum concentration of 0.2 g/l after irradiation.

References

[1]Knoll, G.F., "Radiation Detection and Measurement", John Wiley and Sons (2000).

[2]Kashirin, I.A., Ermakov, A.I., Malinovskiy, S.V., Belanov, S.V., Sapozhnikov, Yu.A., Efimov K.M., Tikomirov, V.A. and Sobolev, A.I., Applied Radiation and Isotopes, 53 (1-2) (2000) 303.

[3]Koike, Y. and Yamamoto, K., Nucl. Inst. and Meth., 84 (1970) 24.

[4]Berlman, I.B., "Handbook of the Fluorescence Spectra of Aromatic Molecules", (Academic Press, New York, 1971).

[5]Berlman, I.B. and Steringraber, O.J., Nucl. Inst. and Meth., 108(1973) 587.

[6]Langenscheidt, E., Nucl. Inst. and Meth., 91 (1971) 237.

[7]Tait, W. H., "Radiation Detection", (Butterworths and Co., Ltd., Britain, 1980).

[8]Doucet, M., Fabre, J.P., Gregoire, G., Panman, J. and Zuccheli, P., Nucl. Inst. and Meth., A459 (2001) 459.

[9]Younis, E.M, "Study of quenching in some liquid scintillation detectors", M.Sc. Thesis, (Univ. of Mosul, College of Science, Physics Dept., Iraq, 2006).

[10]Atalah, S.T., "The fabrication of solid scintillator detector and study of its properties", M.Sc. Thesis, (Univ. of Mosul, College of Science, Physics Dept., Iraq, 2007).

[11]Price, W.J., "Nuclear Radiation Detection", (New York, McGraw-Hill, 1958).

Jordan Journal of Physics

ARTICLE

Indoor Radon Concentrations and Effective Dose Estimation in Dwellings of As-Salt Region in Jordan

M. M. Ya'qoub[a], **I. F. Al-Hamarneh**[a] and **M. Al-Kofahi**[b]

[a] *Department of Applied Science, Prince Abdullah Bin Ghazi Faculty of Science and IT, Al-Balqa Applied University, Salt 19117, Jordan.*
[b] *Department of Physics, Baker University, Baldwin City, KS 66006, USA.*

Abstract: Radon concentrations were measured using passive dosimeters, SSNTD CR-39 in As-Salt city and its surrounding. 300 dosimeters were distributed over the study area dwellings according to the fraction of the population. The exposure time started from April 2004 and lasted for 100 days. Radon concentrations were found to vary from region to region, ranging from 31 to 501 Bq m^{-3} with a mean value of 111 ± 4 Bq m^{-3}. The concentration of radon short-lived daughters was estimated at 44 ± 2 Bq m^{-3} or around 0.012 Working Level (WL). The ground floors were found to have the highest radon concentrations with a mean value of 118 Bq m^{-3}, while the upper floors were found to have a mean value of 96 Bq m^{-3}. Based on the use of the room, bedrooms were found to have a higher mean radon concentration than living or setting rooms; these concentrations were 117 ± 16 and 105 ± 5 Bq m^{-3}, respectively. It was found that As-Salt dweller is exposed annually to 0.49 Working Level Month (WLM) from radon gas and its short-lived daughters. Hence, a person takes on the average an annual effective dose equivalent to 2.7 mSv according to UNSCEAR and 1.9 mSv according to ICRP. This implies an expected value for lung cancer probability of 0.004%.

Keywords: Indoor radon concentration; Passive dosimeter; CR-39; Effective dose; Jordan.

Introduction

Radium is a naturally occurring radioactive element available in trace amounts throughout the Earth crust. The decay of radium leads to a series of short-lived radioactive isotopes via gaseous radon to polonium, bismuth and lead. These decay products are attached, usually, to dust particles in air shortly after they are formed. After inhalation, these products are deposited in the lung, which receives a dose from alpha radiation, emitted during subsequent decay of these products. They also emit gamma rays that increase the external human exposure.

Over the past four decades, natural radiation exposure due to radon (^{222}Rn) and its progeny inside houses has been recognized as a worldwide problem and a cause of significant lung cancer risk to the population. It is also of great importance to assess the exposure to ^{222}Rn and its progeny in houses and areas of high ^{222}Rn levels for the purposes of quality control, radioactivity monitoring of building materials and for correction measures recommendations. Previous research papers [1-6] show that ^{222}Rn, on average, in many countries contributes 50% radiation dose to the general public, including other parts of Jordan, but there is considerable variation due to underlying geology. As-Salt city and its surrounding have more than 330,000 inhabitants, which constitute about 6.5% of the Jordan's total population. The main purpose of the present study was to measure the indoor radon concentration in dwellings

of As-Salt region, the middle part of Jordan, in order to assess whether the general public is at any risk from exposure to excessive levels of radon. Most of the dwellings in As-Salt city and its surrounding are without any compliance to regulatory standards and are typical for one family having two to three rooms. The dwellings surveyed were of different types, but were mainly made of stones with cement. The results of the present study shall help in establishing a baseline map of natural radiation background in this part of the world.

Region of the Study

As-Salt city lies to the northwest of Amman, capital of Jordan, at the latitude of 32° 00' and the longitude of 35° 30' (Fig. 1a). The structure and morphology of the study

area are controlled mainly by the Dead Sea, Jordan Transform Fault that roughly bisects the area into two geomorphological provinces; the Highlands and the Ghor areas. The former has a rough topography with elevations up to 1100 m above sea level (a.s.l.). The Ghor land is, more or less, a table land with elevations between 180 and 360 m a.s.l. The prevalent kinds of stone in the study area are limestone, argillaceous, dolomitic limestone, sandstone, dolomitic sandstone and marl [7]. There is a considerable climate seasonal variation with most of the precipitation occurring during winters (December-March) with a mean annual rainfall of 350 mm. Summers (June-September) are hot (average temperature range of 17-30 ^{o}C) and winters are cold (average temperature range of 3.5-14 ^{o}C).

FIG. 1a. Map of Jordan.

Measuring Procedures

Nuclear track detectors were used to measure the integrated concentrations of radon in As-Salt region. The technique used is based on a closed can containing the CR-39 SSNTD from Pershore Moulding Ltd., U.K. The schematic diagram of the chamber is shown elsewhere [3, 8-9]. To distribute the dosimeters fairly, As-Salt region was divided into 11 sub regions, adopting the formal division of the greater municipality of As-Salt (Fig. 1b), and they were weighted for the fraction of the number of their population to the total number of As-Salt population. In each region, the choice of the dwelling where the measurements were conducted was

random. The dosimeters were distributed in the specified locations starting from April 2004 and collected after the assigned period of 100 days. Every participating dwelling has got two dosimeters; one in the living room and the other in the bedroom, at a height of 1.5 m from the floor. 300 dosimeters were distributed in this study, 254 among them were collected at the end of the period and the remaining 46 were lost for different reasons. The retrieved dosimeters were chemically etched in 6.25 N NaOH, at a temperature of (80 $\pm$ 1) ^{o}C for 4 hours; these conditions give about 85% detection efficiency [10]. An optical microscope of 25× was used to count the number of tracks per cm^2 within the

exposed dosimeters. The tracks were counted randomly all over the detector surface for at least 20 fields of view to obtain an average and representative value of track density for each dosimeter. The measured track densities formed on the analyzed NTDs were converted into radon concentrations (Bq m^{-3}) using the calibration factor of (8.5 tracks cm^{-2} per kBq h m^{-3}) by adopting an exposure period of 100 days. Then the equilibrium equivalent concentration (EEC) was derived by multiplying the radon concentrations (Bq m^{-3}) by an equilibrium factor (F) of 0.4. The potential alpha energy concentration (PAEC),

which was used as a measure of decay product concentration, was obtained in the standard unit of working level (WL) by multiplying EEC by 5.57×10^{-9}. Finally, the PAEC to which the worker is exposed was multiplied by the time of exposure in working months of 170 hours, giving the potential alpha energy exposure (PAEE) in units of working level month (WLM). The lower limit of detection was empirically estimated as 3 times the standard deviation of the non-irradiated dosimeters. The equivalent value of this limit in terms of radon concentration was found to be 0.25 Bq m^{-3}.
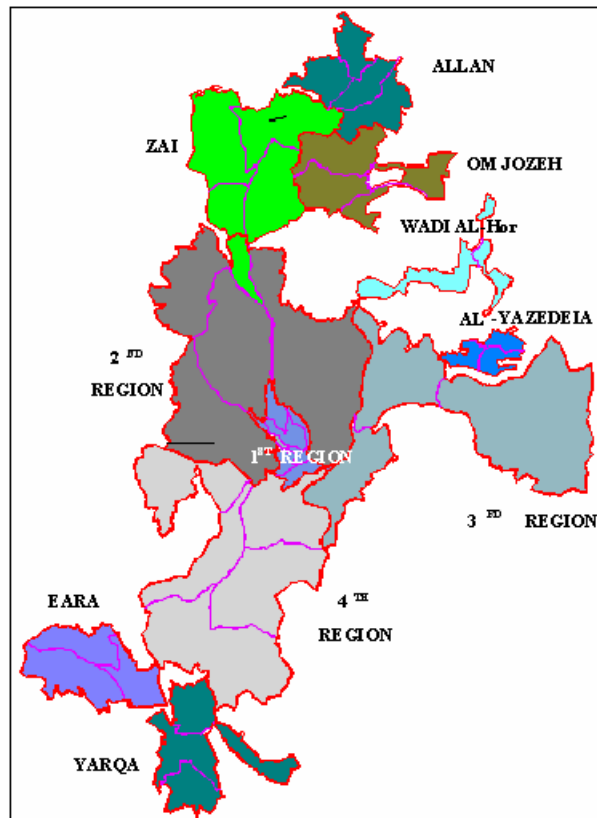

FIG. 1b. Map of the study area.

In order to derive the effective dose of exposure to radon and its progeny for a given time spent in a house if an equilibrium factor of 0.4 is assumed, 1 Bq h m^{-3} is equivalent to 3×10^{-6} mSv [11]. Moreover, the estimated exposure to airborne radon daughters has to be translated into an effective dose equivalent. Deposition and retention of radon daughters in lung are influenced mainly by the size distribution of the carrier aerosol, the fraction of unattached radioactivity, the breathing rate of the subject and biological and physiological factors. Following the suggestions made by UNSCEAR (1982) [12],

a breathing rate of 0.8 m^3 h^{-1} during indoor residence time will lead to a dose conversion factor of 0.061 mSv per Bq m^{-3}. On the other hand, according to ICRP 65 (1993) [11] dose conversion convention, the effective dose per unit of exposure at home is 4 mSv per working level month (WLM), which is based on a working month. It is defined as the amount of radioactive exposure an individual receives if he is exposed to 1 WL of radon for one working month (170 hours), considering the occupancy factor 0.8. Then, 1-year exposure introduces 41 WM [13].

191

Results and Discussion

The frequencies of radon concentration in the surveyed dwellings are plotted in Fig. (2a). From this figure, it can be seen that the frequency distribution looks lognormal-like, as is the case in most other national radon surveys [3, 8]. Moreover, Table 1 summarizes the results of radon levels in 127 houses in the investigated regions. The results indicate a random concentration arithmetic mean of 111 ± 4 Bq m^{-3} with the higher data frequency for values between 60-85 Bq m^{-3}. The measured concentrations were below the action level (< 200 Bq m^{-3}) as reported by ICRP (1993) [11]. Actually, about two thirds of the measured concentrations were lower than 110 Bq m^{-3}. The observed variations of radon concentrations among various regions can be attributed to many factors like the geological structure of the site, the various types of building materials used for the construction of the dwellings, the heating systems and ventilation rates, the aging effect on the building as well as the social habits of the dwellers. As an example, the third region has a feature that most of its dwellings are villas; their dwellers keep the windows closed to keep the elegant furniture away from dust and save energy in both cases of cooling or heating.
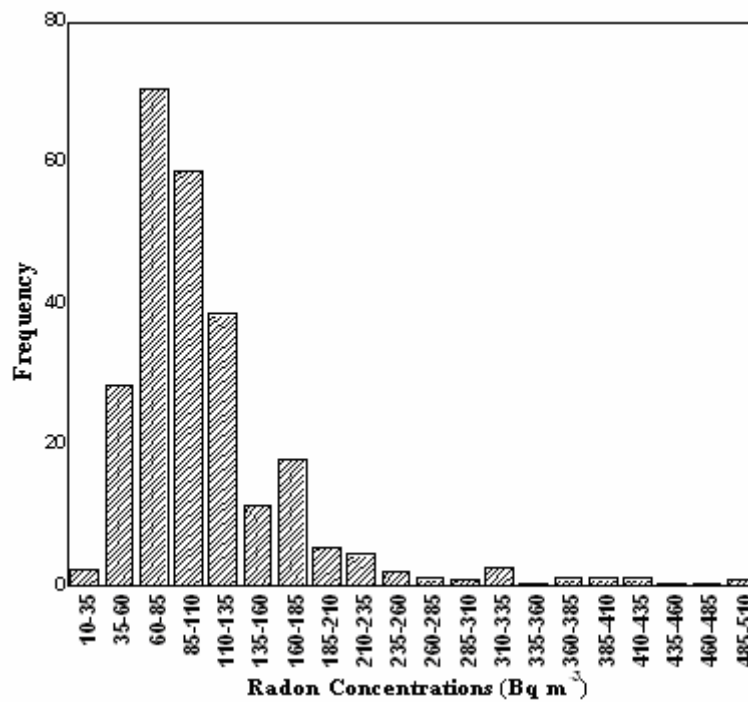

FIG. 2a. Frequency distribution of radon concentrations.

TABLE 1. Radon concentrations in As-Salt region.

Subregion	No. of Dosimeters	Minimum (Bq m^{-3})	Maximum (Bq m^{-3})	Mean $\pm$ σ (Bq m^{-3})
1st	50	34	431	116 ± 10
2nd	98	31	364	105 ± 5
3rd	22	39	392	136 ± 22
4th	20	39	187	101 ± 9
Zai	10	48	501	152 ± 47
Om Jozeh	8	52	168	101 ± 14
Wadi Al-Hor	4	84	129	103 ± 13
Al-Yazedeya	4	134	168	151 ± 17
Yarqa	14	43	213	117 ± 16
Eara	10	50	174	103 ± 12
Allan	14	48	154	86 ± 7
Total	254	39	331	111 ± 4

σ: Standard Error of the Mean.

Preliminary statistics of data for each subregion showed that it was reasonable to divide data into two groups depending on the floor level of the dwelling; ground floor and upper floors (first floor, second floor…etc.). The mean radon concentration for the ground floor was 119 ± 17 Bq m^{-3}, while it was 96 ± 9 Bq m^{-3} for the upper floors. The soil underneath the dwelling is the main radon source for the ground floor house, while the building materials are one of the main contributors at higher floors. In addition, the upper floors are usually more ventilated; their altitudes are higher than any borders or enclosures, which shut the airflow out. In some cases, the ground floors are more ancient than the upper floors. The exhalation of radon from walls, floors and ceilings in the older dwellings is higher than that in modern dwellings because of the cracks and defective joints in walls and floors, due to age and poor maintenance.

Depending on the use of the room, data for the floor itself can be divided into two groups; bedroom and living room. It is shown in Fig. (2b) that the mean radon concentration in bedrooms is higher than that in living rooms in most investigated regions. This may be attributed to the reduction in the ventilation rates in bedrooms. As it is noticeable in Fig. (2b), the radon concentration levels in some regions like the third region have higher values in living rooms than those in bedrooms at the opposite to the normal estimations. This is probably because these dwellings were built using the modern style; the bedrooms are upstairs with less radon concentrations.
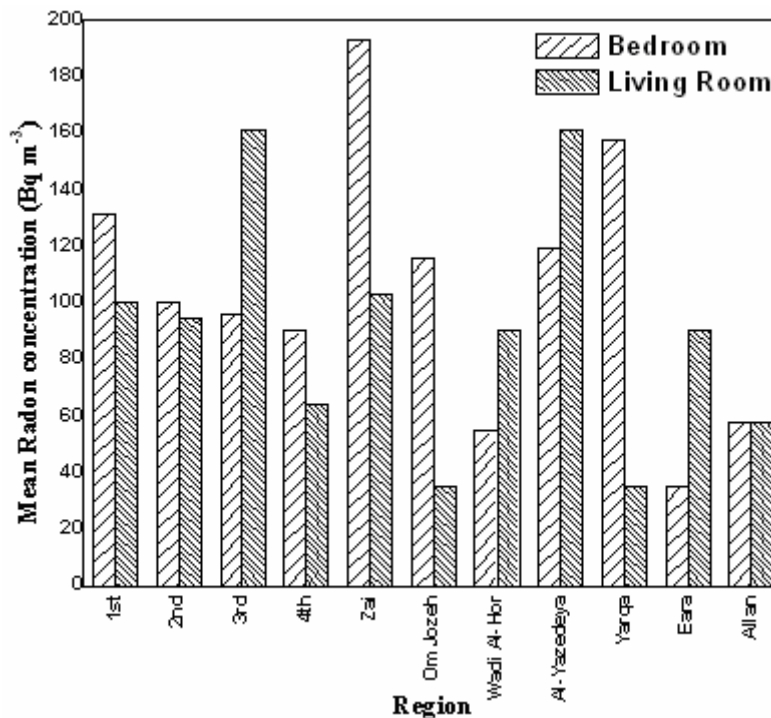

FIG. 2b. Comparison of radon mean concentrations in bedrooms and living rooms in the studied regions.

The radon concentration in As-Salt area is slightly higher in comparison to the major of other national and international areas as can be seen in Table 2. This may be due to the structure of the soil and rocks, which consist mainly of limestone. In addition, it may be due to the geological and topographical nature of As-Salt area, having many flexions and faults due to its mountainous nature [7], and the excavation activity of the earth crust because of building and road construction purposes. There is another intervening factor to influence the survey results and rise up the radon concentration. This factor is the fact that the majority of participants in the survey are employees; this implies that their dwellings are kept closed during the work time when they are outside the house. This may be an important factor in raising the radon concentration levels due to lack of ventilation.

TABLE 2. Radon concentration levels in local and non-local regions.

Country (Region)	Indoor Radon Concentration* (Bq m^{-3})	Reference No.
Jordan (As-Salt)	111 ± 4	Present Study
Jordan (Amman)	41	Khatibeh, A. et al., 1997
Jordan (Zarqa)	31	Khatibeh, A. et al., 1997
Jordan (Irbid)	44	Abumurad, K. and Al-Omari, R., 2008
Jordan (Soum)	144	Abumurad, K. and Al-Tamimi, M., 2005
Syria	44	Othman, I. et al., 1996
Saudi Arabia	16	Al-Jarallah et al., 2003
Egypt	9	Kenawy, M. and Morsy, A., 1991
Iran	82	Sohrabi, M. and Solaymanian, A., 1988
Brazil	82	Canoba, A. et al., 2002
Canada	34	Létourneau, E.G. et al., 1984
China	24	Zuoyuan, W., 1992
Denmark	53	Ulbak, K. et al., 1988
Finland	120	Castrén, O., 1994
France	62	Rannou, A. and Tymen, G., 1989
Mexico	38	Segovia, S. et al., 1993
Poland	41	Biernacka, M., 1992
Sweden	108	Swedjemark, G.A. et al., 1993
UK	20	Wrixon, A.D. et al., 1988
USA	46	Marcinowski, F., 1992
Population-weighted average	44	UNSCEAR, 2000

* Arithmetic mean values.

Based on these limited results obtained from a limited number of houses, as well as the measurements conducted only in one season, radiation doses received by the inhabitants could not be accurately determined. However, some crude estimates of the mean annual effective dose equivalent were determined as shown in Table 3. Table 3 shows the equilibrium equivalent concentration of radon (EEC) in units of Bq m^{-3}, which is the product of radon concentration C by the equilibrium factor F. It corresponds to a concentration of radon for which the radon daughters in equilibrium with radon have the same potential alpha energy as the actual daughter concentration of interest. The PAEC was also derived and shown in Table 3 (in mWL) along with the PAEE in units of WLM. Risk estimation, on the other hand, can be done by adopting a mean absolute risk factor of 0.9 × 10^{-4} per WLM [7]. As it can be seen from Table 3, the inhabitant of As-Salt area is exposed to an annual mean value of 0.49 WLM. This produces an annual effective dose equivalent to 2.71 and 1.95 mSv according to UNSCEAR (1982) [12] and ICRP 65 (1993) [11], respectively. These doses correspond to an average risk of 0.4 × 10^{-4}. This means that the dose due to radon may cause 4 lung cancer cases among each 100,000 inhabitants of As-Salt city per year.

Published data by the Ministry of Health in Jordan indicates that the number of lung cancer cases in As-Salt area was 15 per 100,000 inhabitants during the year 1998 [14]. Thus, one may deduce that lung cancer cases due to smoking and other factors are 11 per 100,000 inhabitants annually. It can be seen from Table 4 that As-Salt area has a high percentage of lung cancer from all types of cancer in comparison to other cities. This seems to agree with the high radon concentration levels in As-Salt area compared to other areas.

TABLE 3. Summarized data of EEC, PAEC, PAEE, annual effective dose and mean risk estimation for each region.

Region	EEC (Bq m^{-3})	PAEC (mWL)	PAEE (WLM)	Annual effective dose (mSv)		Mean estimated risk × 10^{-4}
				(a)	(b)	
1st	46 ± 4	12	0.5	2.0	2.8	0.4
2nd	42 ± 2	11	0.5	1.8	2.6	0.4
3rd	54 ± 9	14	0.6	2.4	3.3	0.5
4th	40 ± 3	11	0.4	1.8	2.5	0.4
Zai	61 ± 18	16	0.7	2.7	3.7	0.6
Om Jozeh	40 ± 5	11	0.4	1.8	2.4	0.4
Wadi Al-Hor	41± 5	11	0.4	1.8	2.5	0.4
Al-Yazedeya	60 ± 7	16	0.7	2.6	3.7	0.6
Yarqa	47 ± 6	12	0.5	2.0	2.8	0.5
Eara	41 ± 5	11	0.4	1.8	2.5	0.4
Allan	34 ± 3	92	0.4	1.5	2.1	0.3
Average	44 ± 2	12 ± 1	0.5	2.0	2.7	0.4

(a) According to ICRP 65 (1993), and (b) According to UNSCEAR (1982).

TABLE 4. Lung cancer percentage in males from all types of cancer (1998 statistics of the Ministry of Health, Jordan).

Governorate	Amman	Irbid	Zarqa	As-Salt	Al-Mafraq	Madaba	Ma'an	Aqaba
Lung Cancer in males %	9.1	12.2	12.4	17.6	9.7	9.5	6.6	7.1

Conclusions

Radon gas concentration levels inside houses of As-Salt area were found to have an average value of 111 ± 4 Bq m^{-3} during April to July of the year 2004. Concentration of radon short-lived daughters was estimated to be 44 ± 2 Bq m^{-3} or around 0.012 WL. It was found that the average exposure of dwellers in As-Salt area is annually 0.49 WLM due to radon gas and its short-lived daughters. This corresponds to an annual effective dose equivalent of 2.7 mSv according to UNSCEAR (1982) [12] and 1.9 mSv according to ICRP 65 (1993) [11]. This also implies an expected value for lung cancer probability of 0.004%, which means that 4 out of each 100,000 dwellers on the average become infected by lung cancer caused by radon inhalation. Even though this is not a high dose, but based on the ALARA principle, it is advisable to reduce the dose. An increase in ventilation rate would probably reduce the concentration level. For future work, it is recommended to extend the survey during other periods of the year in order to have a better representative value for the annual average. It is also recommended to study the radon concentration levels in soil and water in the same region of this study. Finally, the concentration levels as a function of the elevation of houses, due to the mountainous nature of As-Salt area, deserve to be studied.

Acknowledgements

References

[1] UNSCEAR, Ionizing Radiation: Sources and Effects on Ionizing Radiation. Report to the General Assembly, with Annexes. (United Nations, New York, 2000)

[2] Pvlenko, T.A. and Los, I.P., Radiat. Meas., 25(1-4) (1995) 595.

[3] Kullab, M.K., Al-Bataina, B.A., Ismail, A.M. and Abumurad, K.M., Radiat. Meas., 34 (2001) 361.

[4] Mamont-Cieśla, K., Nukleonika, 38(4) (1993) 71.

[5] Al-Saleh, F.S., Appl. Radiat. Isotop., 65 (2007) 843.

[6] Hadad, K., Doulatdar, R. and Mehdizadeh, S., J. Environ. Radioact., 95 (2007) 39.

[7] Basem, K. and Muneuzel, S., "The geology of Al Salt area map sheet no. 3154 III". H.K. J. Nat. Res. Auth. Bulletin, 41, (Amman, Jordan, 1998).

[8] Al-Kofahi, M., Khader, B., Lehlooh, A., Kullab, M., Abumurad, K. and Al-Bataina, B., Nucl. Tracks Radiat. Meas., 20 (1992) 377.

[9] Khatibeh, A., Ahmed, N., Matiullah, Kenawy, M., Abu-Murad, K., Kullab, M. and Al-Bataina, B., Radiat. Meas., 28 (1-6) (1997) 589.

[10] Bing, S., Nucl. Tracks Radiat. Meas., 22(1-4) (1993) 451.

[11] ICRP, "Protection against radon-222 at home and works", ICRP Publication 65, (Pergamon Press, Oxford, England, 1993).

[12] UNSCEAR, Report on Ionizing Radiation: Sources and Biological Effects, (United Nations, New York, 1982).

[13] WHO, Environmental Health Criteria 25, Selected Radionuclides, (Finland, 1983).

[14] Ministry of Health, the Hashemite Kingdom of Jordan. National Cancer Registry Report. Cancer Incidence in Jordan, (Amman, Jordan 1998).

[15] Khatibeh, A., Ahmad, N. and Matiullah, J. Environ. Radioact., 36(1) (1997) 85.

[16] Abumurad, K. and Al-Omari, R., Radiat. Meas., 43 (2008) S389.

[17] Abumurad, K. and Al-Tamimi, M., Radiat. Meas., 39 (2005) 77.

[18] Othman, I., Hushari, M., Raja, G. *et al.*, J. Radiol. Prot., 16(1) (1996) 45.

[19] Al-Jarallah, M., Fazal-ur, R., Abu-Jarad, F. and Al-Shukri, A., Radiat. Meas., 36(1-6) (2003) 445.

[20] Kenawy, M. and Morsy, A., Nucl. Tracks Radiat. Meas., 19 (1991) 343.

[21] Sohrabi, M. and Solaymanian, A., Radiation Protection Practice. Proceedings of the 7th International Congress of the International Radiation Protection Association (Volume 1), (Pergamon Press, Sydney, 1988), p.242.

[22] Canoba, A., Lopez, F., Arnaud, M. et al., Geofis. Int., 41(4) (2002) 453.

[23] Létourneau, E., McGregor, R. and Walker, W., Radiat. Prot. Dosim., 7 (1984) 303.

[24] Zuoyuan, W., "Natural radiation in China: Level and distribution", (Laboratory of Industrial Hygiene, Beijing, 1992).

[25] Ulbak, K., Stenum, B., Sørensen, A. et al., Radiat. Prot. Dosim., 24(1-4) (1988) 401.

[26] Castrén, O., Radiat. Prot. Dosim., 56 (1994) 375.

[27] Rannou, A. and Tymen, G., Exposition au Radon dans les Habitations – Aspects Techniques et Sanitaires. (SFRP, Paris, 1989), p.42.

[28] Segovia, S., Pena, P., Mirele, F. and Quirino, L., Nucl. Track Radiat. Meas., 22(1-4) (1993) 445.

[29] Biernacka, M., Henschke, J., Jagielak, J. *et al.*, Progress of Medical Physics, (1992).

[30] Swedjemark, G., Mellander, H. and Mjönes, L., Indoor Air'93. Proceedings of the 6th International Conference on Indoor Air Quality and Climate, (Helsinki, 1993).

[31] Wrixon, A., Green, B., Lomas, P. et al., Natural radiation exposure in UK dwellings, NRPB-R190, (1988).

[32] Marcinowski, F., Radiat. Prot. Dosim., 45(1-4) (1992) 419.

Authors Index

Subject Index

المناقشة: يجب أن تكون موجزة وتركز على تفسير النتائج.

الاستنتاج: يجب أن يكون وصفا موجزا لأهم ما توصلت إليه الدراسة ولا يزيد عن صفحة مطبوعة واحدة.

الشكر والعرفان: الشكر والإشارة إلى مصدر المنح والدعم المالي يكتبان في فقرة واحدة تسبق المراجع مباشرة.

المراجع: يجب طباعة المراجع بأسطر مزدوجة ومرقمة حسب تسلسلها في النص. وتكتب المراجع في النص بين قوسين مربعين. ويتم اعتماد اختصارات الدوريات حسب نظام Wordlist of Scientific Reviewers.

الجداول: تعطى الجداول أرقاما متسلسلة يشار إليها في النص. ويجب طباعة كل جدول على صفحة منفصلة مع عنوان فوق الجدول. أما الحواشي التفسيرية، التي يشار إليها بحرف فوقي، فتكتب أسفل الجدول.

الرسوم التوضيحية: يتم ترقيم الأشكال والرسومات والرسومات البيانية (المخططات) والصور، بصورة متسلسلة كما وردت في النص.

تقبل الرسوم التوضيحية المستخرجة من الحاسوب والصور الرقمية ذات النوعية الجيدة بالأبيض والأسود، على ان تكون أصيلة وليست نسخة عنها، وكل منها على ورقة منفصلة ومعرفة برقمها بالمقابل. ويجب تزويد المجلة بالرسومات بحجمها الأصلي بحيث لا تحتاج إلى معالجة لاحقة، وألا تقل الحروف عن الحجم 8 من نوع Times New Roman، وألا تقل سماكة الخطوط عن 0.5 وبكثافة متجانسة. ويجب إزالة جميع الألوان من الرسومات ما عدا تلك التي ستنشر ملونة. وفي حالة إرسال الرسومات بصورة رقمية، يجب أن تتوافق مع متطلبات الحد الأدنى من التمايز (1200 dpi Resolution) لرسومات الأبيض والأسود الخطية، و 600 dpi للرسومات باللون الرمادي، و 300 dpi للرسومات الملونة. ويجب تخزين جميع ملفات الرسومات على شكل (jpg)، وأن ترسل الرسوم التوضيحية بالحجم الفعلي الذي سيظهر في المجلة. وسواء أرسل المخطوط بالبريد أو عن طريق الشبكة (Online)، يجب أرسال نسخة ورقية أصلية ذات نوعية جيدة للرسومات التوضيحية.

مواد إضافية: تشجع المجلة الباحثين على إرفاق جميع المواد الإضافية التي يمكن أن تسهل عملية التحكيم. وتشمل المواد الإضافية أي اشتقاقات رياضية مفصلة لا تظهر في المخطوط.

المخطوط المنقح (المعدَّل) والأقراص المدمجة: بعد قبول البحث للنشر وإجراء جميع التعديلات المطلوبة، فعلى الباحثين تقديم نسخة أصلية ونسخة أخرى مطابقة للأصلية مطبوعة بأسطر مزدوجة، وكذلك تقديم نسخة إلكترونية تحتوي على المخطوط كاملا مكتوبا على Microsoft Word for Windows 2000 أو ما هو استجد منه. ويجب إرفاق الأشكال الأصلية مع المخطوط النهائي المعدل حتى لو تم تقديم الأشكال إلكترونيا. وتخزن جميع ملفات الرسومات على شكل (jpg)، وتقدم جميع الرسومات التوضيحية بالحجم الحقيقي الذي ستظهر به في المجلة. ويجب إرفاق قائمة ببرامج الحاسوب التي استعملت في كتابة النص، وأسماء الملفات على قرص مدمج، حيث يعلَم القرص بالاسم الأخير للباحث، وبالرقم المرجعي للمخطوط للمراسلة، وعنوان المقالة، والتاريخ. ويحفظ في مغلف واقٍ.

الفهرسة: تقوم المجلة الأردنية للفيزياء بالإجراءات اللازمة لفهرستها وتلخيصها في جميع الخدمات الدولية المعنية.

حقوق الطبع

إخلاء المسؤولية

تقديم مخطوط البحث

تُرسَل نسخة أصلية وثلاث نسخ من المخطوط، مُرْفَقَةً برسالة تغطية من جانب الباحث المسؤول عن المراسلات، إلى رئيس التحرير:

أ.د. ابراهيم أبو الجرايش،

رئيس التحرير، المجلة الأردنية للفيزياء،

عمادة البحث العلمي والدراسات العليا،

جامعة اليرموك، اربد، الأردن.

هاتف : 111 11 72 2 962 00 / فرعي: 3735

فاكس : 121 11 72 2 962 00

بريد إلكتروني : jjp@yu.edu.jo

تقديم المخطوطات إلكترونيًا: اتبع التعليمات في موقع المجلة على الشبكة العنكبوتية.

ويجري تحكيمُ البحوثِ الأصيلة والمراسـلات القصيرة والملاحظات الفنية من جانب مُحكِّمين اثنين في الأقل من ذوي الاختصاص والخبرة. وتُشجَّع المجلـة البـاحثين على اقتراح أسمـاء المحكمين. أمـا نشـر المقـالات الخاصّـة فـي المجـالات الفيزيائيـة النَشِطَـة، فيتم بـدعوة مـن هيئـة التحرير، ويُشـار إليها كذلك عند النشر. ويُطلَب من كاتب المقال الخاص تقديم تقرير واضح يتَسم بالدقة والإيجاز عـن مجال البحث تمهيداً للمقال. وتنشر المجلة أيضاً مقالات المراجعة في الحقول الفيزيائية النشطة سريعة التغيُّر، وتشَجَّع كاتبي مقالات المراجعة أو مُستَكتبيها على إرسال مقترح من صفحتين إلى رئيس التحرير. ويُرفَق مع البحث المكتوب باللغة العربية ملخص (Abstract) وكلمات دالة (Keywords) باللغة الإنجليزية.

ترتيب مخطوط البحث

يجب أن تتم طباعة مخطوط البحث ببنط 12 نوعه Times New Roman، وبسطر مزدوج، على وجه واحد من ورق A4 (21.6 × 27.9 سم) مع حواشي 3.71 سم ، باستخدام معالج كلمات ميكروسوفت وورد 2000 أو ما اسْتَجَد منه. ويجري تنظيم أجزاء المخطوط وفق الترتيب التالي: صفحة العنوان، الملخص، رموز التصنيف (PACS)، المقدّمة، طرق البحث، النتائج، المناقشة، الخلاصة، الشكر والعرفان، المراجع، الجداول، قائمة بدليل الأشكال والصور والإيضاحات، ثَمَّ الأشكال والصور والإيضاحات. وتُكتَب العناوين الرئيسـة بخطّ **غامق**، بينما تُكتَب العناوين الفرعية بخطّ *مائل.*

صفحة العنوان: وتشمل عنوان المقالة، أسماء الباحثين الكاملة وعناوين العمل كاملة. ويكتب الباحث المسـؤول عن المراسلات اسمه مشـارا إليه بنجمة، والبريد الإلكتروني الخاص به. ويجب أن يكون عنوان المقالة موجزا وواضحا ومعبرا عن فحوى (محتوى) المخطوط، وذلك لأهمية هذا العنوان لأغراض استرجاع المعلومات.

الملخص: المطلوب كتابة فقرة واحدة لا تزيد على مـائتي كلمـة، موضـحة هـدف البحـث، والمنهج المتبع فيه والنتائج وأهـم مـا توصل إليه الباحثون.

الكلمات الدالة: يجب أن يلي الملخص قائمة من 4-6 كلمات دالة تعبر عن المحتوى الدقيق للمخطوط لأغراض الفهرسة.

PACS: يجب إرفاق الرموز التصنيفية، وهي متوافرة في الموقع http://www.aip.org/pacs/pacs06/pacs06-toc.html.

المقدمة: يجب أن توضّح الهدف من الدراسة وعلاقتها بالأعمال السابقة في المجال، لا أن تكون مراجعة مكثفة لمـا نشر (لا تزيد المقدمـة عن صفحة ونصف الصفحة مطبوعة).

طرائق البحث (التجريبيـة / النظريـة): يجب أن تكون هـذه الطرائق موضحة بتفصيل كاف لإتاحة إعادة إجرائها بكفـاءة، ولكن باختصـار مناسب، حتى لا تكون تكرارا للطرائق المنشورة سابقا.

النتائج: يستحسن عرض النتائج على صورة جداول وأشكال حيثما أمكن، مع شرح قليل في النص ومن دون مناقشة تفصيلية.

Name: .... :الأسم

Specialty: .... :التخصص

Address:.. :العنوان

P.O. Box: .... :صندوق البريد

City & Postal Code:... :المدينة/الرمز البريدي

Country:... :القطر

Phone:.. :رقم الهاتف

Fax No:.. :رقم الفاكس

E-mail: .... :البريد الإلكتروني

No. of Subscription:... :عدد الإشتراكات

Method of Payment: .... :طريقة الدفع

Amount Enclosed: .... :المبلغ المرفق

Signature:... :التوقيع

Cheques should be paid to Deanship of Research and Graduate Studies - Yarmouk University.

I would like to subscribe to the Journal
For

- ❏ One Year
- ❏ Two Years
- ❏ Three Years

One Year Subscription Rates		
	Inside Jordan	Outside Jordan
Individuals	JD 8	€ 40
Students	JD 4	€ 20
Institutions	JD 12	€ 60

Correspondence

المجلة الأردنية

للفيزياء

مجلة بحوث علمية عالمية محكّمة

رئيس التحرير:

ابراهيم عثمان أبو الجرايش

قسم الفيزياء، جامعة اليرموك، إربد، الأردن.

ijaraysh@yu.edu.jo

هيئة التحرير:

ضياء الدين محمود عرفة

قسم الفيزياء، الجامعة الأردنية، عمان، الأردن.

darafah@ju.edu.jo

نبيل يوسف أيوب

الجامعة الألمانية الأردنية، عمان، الأردن.

nabil.ayoub@gju.edu.jo

هشام بشارة غصيب

رئيس جامعة الأميرة سمية للتكنولوجيا، عمان، الأردن.

ghassib@psut.edu.jo

جميل محمود خليفة

قسم الفيزياء، الجامعة الأردنية، عمان، الأردن.

jkalifa@ju.edu.jo

سامي حسين محمود

قسم الفيزياء، جامعة اليرموك، إربد، الأردن.

(قسم الفيزياء، جامعة آل البيت، المفرق، الأردن.)

mahmoods@yu.edu.jo

مروان سليمان الموسى

قسم الفيزياء، جامعة مؤتة، الكرك، الأردن.

mmousa@mutah.edu.jo

نهاد عبد الرؤوف يوسف

قسم الفيزياء، جامعة اليرموك، إربد، الأردن.

nihadyusuf@yu.edu.jo

سكرتير التحرير: مجدي الشناق